NTNU – Trondheim
Norwegian University of
Science and Technology

Sound Field Analysis of Rooms with Ceiling Absorbers

Hallvard Andreas Granseth

Master of Science in Physics and Mathematics	
Submission date:	June 2015
Supervisor:	Jon Andreas Støvneng, IFY
Co-supervisor:	Peter Svensson, IET Magne Skålevik, Brekke & Strand Akustikk AS

Norwegian University of Science and Technology
Department of Physics

Abstract

The theory on damped modes and absorption of modes with grazing incidence presented by Kinsler et al. has been applied to the shoebox-shaped room with five hard walls and one absorber wall, using measurements in a scale model box. Single mode reverberation time analysis, estimations of reverberation time based on grazing mode absorption via measurements of the specific acoustic impedance, and measurements of vertical components of the sound intensity has all been used in an attempt at identifying grazing modes and comparing the theoretical descriptions to the observed sound field.

The thesis found Kinsler et al.'s theory on damped modes and absorption of modes with grazing incidence to be poorly suited for the shoebox-shaped room with five hard walls and one absorber wall. Grazing modes and non-grazing modes were not separable, neither by reverberation time estimates nor by sound intensity measurements. The reverberation time estimates using the damped modes & grazing mode absorption theory were several orders of magnitude less than the observed reverberation time. The most likely weakness in the theory is thought to be the assumption on wall impedance, which does not fit with porous absorbers on rigid walls.

Sammendrag

Teori om dempede moder og absorpsjon av moder med streifende innfall presentert av Kinsler et al. har blitt anvendt på et skoeskeformet rom med fem harde vegger og en absorberende vegg, ved bruk av målinger i en skalamodell. Analyse av enkeltmoders etterklangstid, estimering av etterklangstid basert på absorpsjonsteorien for streifende moder via målinger av spesifikk akustisk impedans, og målinger av vertikalkomponenter av lydintensitet har blitt brukt i et forsøk på å identifisere streifende moder og sammenligne de teoretiske beskrivelsene med det observerte lydfeltet.

Denne masteroppgaven fant at Kinsler et al.'s teori om dempede moder og absorpsjon av moder med streifende innfall var dårlig tilpasset det skoeskeformede rommet med fem harde vegger og en absorberende vegg. Streifende moder og ikke-streifende moder var ikke separable, hverken ved estimering av etterklangstid eller ved lydintensitetsmålinger. Estimatene for etterklangstid ved bruk av teorien om dempede moder & absorpsjon av moder med streifende innfall var flere størrelsesordener mindre enn den observerte etterklangstiden. Den mest sannsynlige svakheten i teorien er tenkt å være antagelsen om veggimpedans, da denne ikke passer med porøse absorbenter på harde vegger.

Preface

This thesis is submitted in fulfillment with the requirements of the Master's Programme in Applied Physics and Mathematics with specialization in Applied Physics at The Norwegian University of Science and Technology (NTNU).

The work included in this thesis was done mainly from February to June 2015. The work relies to some extent on a project done in preparation for the master's thesis during the autumn of 2014 and winter of 2014-2015. Four figures in this thesis are either reprints from this project or include results obtained in this project. These figures are included for illustrative purposes when relevant and they do not feature in Chapter 4 **Measurement results**.

The thesis is a continuation of the work of co-supervisor Magne Skålevik on small room acoustics. He deserves acknowledgment for his guidance throughout the project. Co-supervisor Professor Peter Svensson from the Department of Electronics and Telecommunications deserves recognition for being the primary academic supervisor and following the work on a regular basis. Appreciations are given to supervisor Associate Professor Jon Andreas Støvneng from the Department of Physics for helpful advice when needed.

Thanks also to Reyn O'Born for assistance with the English language and to Lars Brodal for providing conversation, coffee and a laptop computer. Finally, I would like to thank my family for providing much appreciated support through all my years at NTNU.

Hallvard Granseth, Trondheim, June 2015

Table of Contents

List of Figures

Abbreviations

A selection of the most important abbreviations and denotations of physical concepts.

SNR = Signal-to-noise ratio
1,2,3D = 1,2,3 dimension(s)

B = Filter bandwidth
f = Frequency
f_s = Schröder frequency
H = Transfer function
I = Sound intensity
k = Wave number
p = Sound pressure
t = Time
T = Reverberation time
u = Particle velocity
V = Volume
z = Specific acoustic impedance

α = Sound absorption coefficient
$\alpha_{x,y,z}$ = Spacial absorption coefficient
β = Temporal absorption coefficient
θ = Angle of wave propagation
λ = Wave length
σ = Airflow resistivity
ω = Angular frequency

Relevant constants

c = Speed of sound in air
ρ_0 = Equilibrium density of air

Chapter 1

Introduction

1.1 Background

The Norwegian Standard NS8175 *Acoustic conditions in buildings, Sound classification of various types of buildings* serves as reference for the Norwegian Building Codes, and includes limiting values for room acoustical parameters. In general, these limiting values are given for reverberation time, T, and mean sound absorption coefficient $\bar{\alpha}$ for the surfaces in various rooms and building types [16, pp. 3,9,12]. With T being one of normally only two room acoustical parameters, the importance of being able to predict it is self-evident.

However, the shoebox-shaped, or *rectangular cuboid*, room with hard, flat walls and floors and a soft, absorbing ceiling makes T difficult to predict. This room has been dubbed THE HARD CASE [15]. Common HARD CASE rooms are offices, meeting rooms, classrooms, recording or rehearsal spaces for music, gymnastic halls and cafeterias.

1.2 Motivation

A previous project by the author [5] investigated the behaviour of sound absorbing surfaces in THE HARD CASE, using a scale model box. The focus of the investigation was a difference in absorbing ability between high and low frequencies that varied significantly from what was expected, as shown in Figure 1.1. Above some unknown cross-over frequency f_x, the sound wave will be affected by the absorber to a lesser degree. However below f_x, the sound wave will be affected by the absorber to quite a larger degree. The observed differences in absorption characteristics between low and high frequencies are not predicted by any existing theory, nor is the cross-over frequency region specified. Figure 1.1 shows how the low-frequency region features an unexpectedly high α compared to predictions of $\alpha_{diffuse}$ and $\alpha(\theta \rightarrow 90°)$ by the Delany-Bazley model, and assuming locally reacting material.

It should be noted that the absorption coefficient α obtained from the measurements of the scale model absorber has been derived using the Sabine expression for reverberation time (equation (2.48). This equation assumes diffuse field conditions, which are not met by THE HARD CASE – and particularly not below the Schröder frequency. Consequently, the blue 'Scale model measured α' line in Figure 1.1 should be viewed with some scepticism. Note also how the 'Scale model measured α' line might articulate two frequency dependences: One frequency dependence of α for the absorber sample, and another for the coupling between the absorber and the sound field.

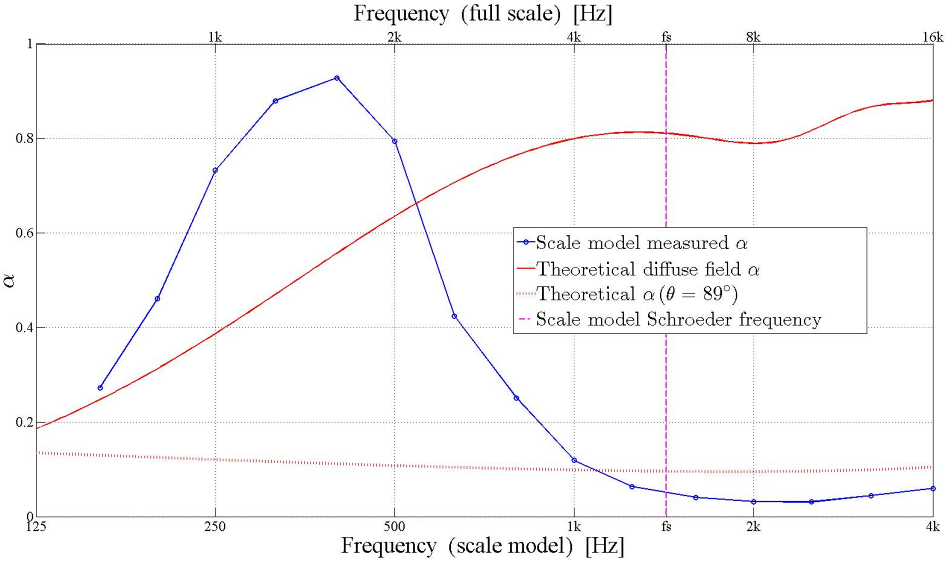

Figure 1.1: Theoretical diffuse field absorption, theoretical quasi-grazing absorption and measured scale model absorption for a porous absorber, with scale model Schröder frequency $f_s \approx 1.4$ kHz

Eliminating possible explanations having to do with the scale model and absorbers used, the following hypothesis was formulated to explain this behaviour: The sound field can be described as sound waves divided into two groups – the waves that are propagating parallel to the ceiling absorber and the waves that are not. The sound waves that are not propagating parallel to the ceiling can be said to have a vertical component.

> The vertical components of the sound field will be quickly damped and the horizontal components will die out more slowly. This remaining reverberant field will constitute a 2D sound field propagating parallel to the ceiling. The observed frequency dependent absorption might be explained by grazing incidence absorption (of the 2D field in the ceiling absorber) having different charactereistics than what is predicted by standard theory.

Examining existing theory on grazing incidence absorption, the frequency dependence observed is not described, and the difference in absorption between modes with grazing incidence (or *grazing modes*) and modes with non-grazing incidence (or *non-grazing modes*) is not big enough to account for the observed absorption differences. The experimental results indicates the theoretical relationship between grazing modes and non-grazing modes may be incorrect, and a look at grazing incidence absorption is warranted.

1.3 Problem description

> In rooms where the absorption is dominated by ceiling absorbers, long reverberation time can be observed at middle and high frequencies, i.e. that absorbers have low efficiency. This is explained by the sound field being dominated by horizontally propagating sound waves that are slightly damped. The ceiling absorber can still function efficiently at low frequencies, although standard theory predicts the opposite to be true. In this master thesis the functioning of the ceiling absorber will be explored using scale model measurements and theoretical calculations.

To elaborate, theory by Kinsler et al. [8, p. 350] on damped modes' grazing incidence absorption states that grazing modes will be absorbed by a factor 1/2 the absorption of non-grazing modes, and consequently that grazing modes will have twice the reverberation time of non-grazing modes. The expressions are not linked to frequency dependence in a way that sufficiently explains the observed absorption. If the theoretical expression for grazing modes can be challenged, grazing modes might have a frequency dependent absorption more in line with the observed absorption and the hypothesis explaining the reverberant behaviour of THE HARD CASE might be valid.

By measuring T for single modes and comparing T for grazing modes with T for non-grazing modes, it might be possible to dispute the validity of Kinsler et al.'s expressions. Additionally, T may be determined from the expressions for grazing incidence absorption based on measurements of the specific acoustic impedance, and thereby also indicate the validity (or lack thereof) of Kinsler et al.'s expressions. Finally, measurements of the vertical sound intensity component might serve to identify any grazing modes and maybe offer some illumination into how the absorber interacts with the sound field.

1.4 Structure

Chapter 2 will contain the relevant theoretical background in room acoustics. Chapter 3 will present the scale model box and sound absorber, the measurement method and equipment used. The measurement results are presented in Chapter 4, including modal estimations of T, calculations of T based on the theoretical expressions for grazing incidence and some examinations of the sound intensity as a function of distance to the absorber ceiling. The results will be discussed and compared in Chapter 5. This chapter will also contain comments on sources of error and some suggestions for further work. Lastly, Chapter 6 presents the conclusions.

Chapter 2

Theory

This chapter presents some important concepts in room acoustics - namely the wave equation & modes, intensity & impedance, reflection & absorption, and reverberation time. Different approaches to grazing incidence absorption are briefly elaborated. In addition, some notes on the Fourier transform, the scale model and the sound absorber are also included.

Notation

- **Bold** characters denote complex quantities.
- $\boldsymbol{X}^*$ denotes the complex conjugate of $\boldsymbol{X}$.
- j denotes the complex number $\sqrt{-1}$.

2.1 Wave theoretical room acoustics

The concepts elaborated in Section 2.1 will be presented in depth. This is because they are particularly important for understanding the implications of the results presented in Chapter 4.

2.1.1 The wave equation

The partial differential equation called *The Wave Equation* can be used with knowledge of the room's dimensions and boundary conditions to derive the exact sound pressure anywhere within the room [21, p. 497] [8, p. 349]. Including a sound source term, the inhomogeneous wave equation can be expressed as

$$\nabla^2 p(x,y,z,t) - \frac{1}{c^2}\frac{\partial^2 p(x,y,z,t)}{\partial t^2} = q(x',y',z',t') \tag{2.1}$$

where $p(x,y,z,t)$ is the sound pressure at coordinates (x,y,z) and time t and $q(x',y',z',t')$ is the source signal at coordinates (x',y',z') and time t'. Removing the source term from the equation (replacing the right-hand side with zero) gives the homogeneous version of the wave equation, which can be used to derive an expression for $p(x,y,z,t)$:

In a closed rectangular cuboid cavity with rigid boundaries (where the sound energy cannot escape) and assuming the time dependency of $\boldsymbol{p}$ can be expressed as $e^{j\omega t}$, we can assume a solution to the wave equation for p [8, p. 247]

$$\boldsymbol{p}(x,y,z,t) = \boldsymbol{X}(x)\boldsymbol{Y}(y)\boldsymbol{Z}(z)e^{j\omega t} \tag{2.2}$$

where the separation of variables leads to the following set of equations:

$$\begin{aligned}\left(\frac{d^2}{dx^2} + k_x\right)\boldsymbol{X} &= 0\\ \left(\frac{d^2}{dy^2} + k_y\right)\boldsymbol{Y} &= 0\\ \left(\frac{d^2}{dz^2} + k_z\right)\boldsymbol{Z} &= 0\end{aligned}$$

and the wave number

$$\left(\frac{\omega}{c}\right)^2 = k^2 = k_x^2 + k_y^2 + k_z^2\ . \tag{2.3}$$

The boundary condition of rigid boundaries means that the air particle velocity component normal to the wall has to be zero at the wall. This is expressed as

$$\left(\frac{\delta p}{\delta i}\right)_{i=0} = \left(\frac{\delta p}{\delta i}\right)_{i=L_i} = 0 \qquad , \qquad i = x,y,z \tag{2.4}$$

where L_i are the dimensions of the cavity, and which leads to $\boldsymbol{p}$ expressed as a sum of cosines:

$$\boldsymbol{p}_{n_x n_y n_z} = \Sigma_{n_x n_y n_z} \boldsymbol{A}_{n_x n_y n_z} \cos(k_x x) \cos(k_y y) \cos(k_z z)\, e^{j\omega_{n_x n_y n_z} t} \tag{2.5}$$

where the cosine functions are called *modes* [8, p. 53], $A_{n_x n_y n_z}$ is called the *mode amplitude* and the wave number components are quantized in the following manner:

$$\begin{aligned} k_{i,n_i} &= \frac{n_i \pi}{L_i} \quad , \quad && n_i = 0, 1, 2... \\ & && i = x, y, z \end{aligned} \tag{2.6}$$

where n_i is called the *order* of the mode.

Combining equations (2.3) and (2.6) gives the *eigenfunctions* or *modal frequencies* of the cavity:

$$f_{n_x n_y n_z} = \frac{c}{2}\sqrt{\left(\frac{n_x}{L_x}\right)^2 + \left(\frac{n_y}{L_y}\right)^2 + \left(\frac{n_z}{L_z}\right)^2} \tag{2.7}$$

These frequencies are also called *natural frequencies* or *standing waves*, because their wavelengths corresponds to the dimensions of the cavity in such a way that the sound waves will interfere positively with themselves. Note that energy loss is not included, theoretically causing infinitely high amplitudes for perfectly rigid cavity walls.

2.1.2 Standing waves

Reducing the theory to one dimension for a moment, the sound pressure distribution of the fundamental mode of order 1 ($n_x = 1$) will follow the cosine expression from equation (2.5) for half a period, having $|p| = p_{max}$ at both walls ($x = 0$ & $x = L_x$). The sound pressure will have a *node* (where the sound pressure is zero) half-way between the pressure maxima.

The 2nd order mode (or *1st harmonic*) will follow the same pattern for one period – having half as long wavelength and twice as high frequency. The mode has pressure maxima at both walls and halfway between the walls, with two nodes half-way between pressure maxima. Similarly, the 3rd order mode (or *2nd harmonic*) has a wavelength that is 1/3 the wavelength of the fundamental mode, with four pressure maxima and three nodes.

Plotting the absolute value $|p|$ of the cosine-function sound pressure distribution for the first 10 modes in Figure 2.1, the following can be observed:

- All odd order modes will have a node at $L_i/2$.
- Every other even order mode will have nodes at $L_i/4$ and $3L_i/4$

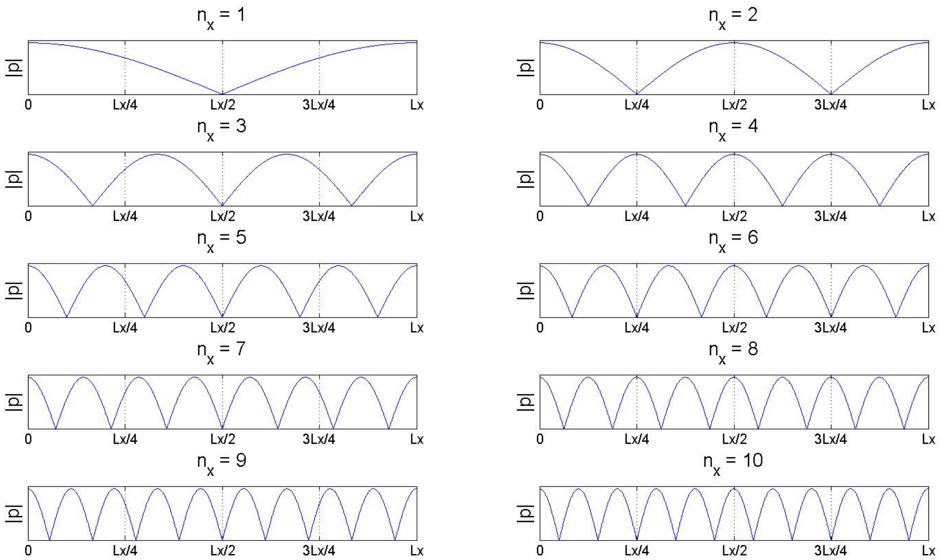

Figure 2.1: Pressure distribution of modes $n_x = 1 - 10$ in 1D

2.1.3 The few modes region & the Schröder region

The number of eigenfunctions ΔN with a resonance frequency within a frequency range Δf is called the *mode density*

$$\frac{\Delta N}{\Delta f} \approx \frac{4\pi f^2}{3c^3}V + \frac{\pi f}{2c^2}S + \frac{L}{8c} \tag{2.8}$$

where S is the total surface area of the room and L is the total length of the edges of the surface segments [19, p. 111]. What equation (2.8) demonstrates is that there are few modes at low frequencies and many modes at high frequencies. If there are few modes in a frequency range, the sound pressure may differ significantly across the room – having clearly defined sound pressure nodes and maxima. On the other hand if the mode density is high enough, the response curves of the standing waves will overlap:

Any sound pressure maxima will be due to interference between more than one mode and the average sound pressure distribution will be the same throughout the room.

For increasingly higher frequencies, the sound field will demonstrate increasing amounts of *diffuse field* characteristics. In a diffuse sound field, the sound pressure is the same across the entire room. A perfectly diffuse field is only theoretically possible, but for *sufficiently high* mode density and modal overlap, it is possible to have a *fairly diffuse* field. Specifically, for increasing frequencies the probability of finding overlapping modes that together will constitute a diffuse field, is higher.

In a sound field with high enough modal overlap, single modes cannot be distinguished from each other and statistical room acoustics (see Section 2.5) is the only practical way to describe the room's acoustics. The criterion of sufficiently high mode density was defined by Schröder in the 1962 as a three-fold modal overlap [13, p. 1]. The frequency range with the minimum three-fold average modal overlap is called the *Schröder region*. Furthermore, he developed a frequency limit, above which the probability of finding this average three-fold modal overlap is high. This frequency limit is called the *Schröder frequency*:

$$f_s = 2000 \cdot \sqrt{\frac{T}{V}} \; . \tag{2.9}$$

Schröder also introduced another characteristic property of the high frequency region, namely the average maximum spacing between frequency maxima as a function of the reverberation time[13, p. 3]:

$$\overline{f}_{max} \approx \frac{4}{T} \; . \tag{2.10}$$

Just as the high frequency region (or the Schröder region) is defined by a minimum three-fold average modal overlap, the low frequency region is defined by modes being separable. Hence, the low frequency region is also called the *few modes region*. However, the Schröder frequency limit is not meant as a sharp boundary and a cross-over region between the few modes region and the Schröder region is observable. Specifically, it is possible to observe sound fields where equation (2.10) are valid for frequencies below $f = f_s$.

In other words, the few modes region where $\overline{f}_{max}$ is not defined and modes are separable, can be followed by a cross-over region where $\overline{f}_{max}$ is valid while $f < f_s$. The cross-over region is then followed by the Schröder region, where $\overline{f}_{max}$ is valid *and* $f > f_s$.

By applying equation (2.10) to equation (2.8), the frequency limit between the few modes region and the cross-over region becomes

$$f_{new} = 900 \cdot \sqrt{\frac{T}{V}} \, , \tag{2.11}$$

as suggested by Magne Skålevik [14, p. 3].

In other words, the modal theory applies up to f_{new}, statistical theory applies from f_s and upwards, but in the frequency range $f_{new} - f_s$ the literature is inconclusive.

2.1.4 Damped modes

Without perfectly rigid cavity walls, the particle velocity at the wall, normal to the wall will not be zero and equations (2.4) are no longer valid. Instead the temporal absorption coefficient β and the spacial absorption coefficients α_i are introduced [8, p. 349]:

$$\begin{aligned} \boldsymbol{k}_i &= k_i + j\alpha_i \qquad , \qquad i = x, y, z \\ \left(\frac{\boldsymbol{\omega}_D}{c}\right)^2 &= \boldsymbol{k}_x^2 + \boldsymbol{k}_y^2 + \boldsymbol{k}_z^2 \\ \boldsymbol{\omega}_D &= \omega_D + j\beta \end{aligned} \tag{2.12}$$

This leads to the expression for damped p^D:

$$\boldsymbol{p}^D_{n_x n_y n_z} = \Sigma_{n_x n_y n_z} \boldsymbol{A}_{n_x n_y n_z} \cos\left(\boldsymbol{k}_x x + \phi_x\right) \cos\left(\boldsymbol{k}_y y + \phi_y\right) \cos\left(\boldsymbol{k}_z z + \phi_z\right) e^{j\boldsymbol{\omega}_D t} \tag{2.13}$$

where k_i, ϕ_i and α_i are determined by the boundary conditions of the cavity. Simplifying the expression in equation (2.13) somewhat, it can be rewritten as

$$\boldsymbol{p}^D_{n_x n_y n_z}\left(x, y, z\right) = \Sigma_{n_x n_y n_z} \boldsymbol{A}_{n_x n_y n_z} \boldsymbol{\Phi}_{n_x n_y n_z}\left(x, y, z\right) e^{j\boldsymbol{\omega}_D t} \tag{2.14}$$

where $\boldsymbol{\Phi}\left(x, y, z\right)$ substitutes the cosines.

Around a resonance frequency, this sum will be dominated by one term in the series:

$$\boldsymbol{p}^D_{n_x = a,\, n_y = b,\, n_z = c}\left(x, y, z\right) \approx \boldsymbol{A}_{abc} \boldsymbol{\Phi}_{abc}\left(x, y, z\right) e^{j\boldsymbol{\omega}_D t} \, . \tag{2.15}$$

2.1.5 Modes with grazing incidence

Mode frequencies with only one non-zero order n_i are termed axial modes because the sound pressure wave propagates parallell to one of the axes. Mode frequencies with two non-zero orders n_i are termed tangential modes because the sound pressure wave propagates parallel to one of the surfaces. Modes frequencies without non-zero orders ($n_{x,y,z} \neq 0$) are termed oblique modes.

Tangential mode sound pressure waves travelling parallel to one of the surfaces of the room, have an incidence angle on the surface of 90°. These modes are said to have *grazing* incidence on the surface.

The amount of sound energy transmitted into the wall and reflected back from the wall will depend both on the material the wall is made from and on the incidence angle of the sound wave. As the incidence angle approaches 90° the amount of energy absorbed is greatly diminished.

2.2 Intensity & impedance

2.2.1 Intensity

The acoustic intensity I of a sound wave is the time-averaged rate of work being done on one fluid element by another [8, p. 125]. This is expressed as the time-averaged product of the particle sound pressure and velocity:

$$I = \frac{1}{\tau_2 - \tau_1} \int_{\tau_1}^{\tau_2} p(t) \cdot u(t) dt \tag{2.16}$$

where $\tau_2 - \tau_1$ is the time period of the averaging. For a plane wave propagating parallel to the x-axis, $p = \pm\rho_0 c u$, which reduces the expression for the intensity in the x-direction to

$$I_x = \overline{p(t) \cdot u_x(t)} = \pm\frac{P^2}{2\rho_0 c} \tag{2.17}$$

where P is the amplitude of p.

2.2.2 Impedance

The sound field impedance is obtained by dividing the acoustic pressure by the particle velocity. This is also called the *specific acoustic impedance*:

$$\boldsymbol{z} = \frac{\boldsymbol{p}}{\boldsymbol{u}} \, . \tag{2.18}$$

For a plane wave the specific acoustic impedance becomes

$$\boldsymbol{Z} = \pm\rho_0 c \tag{2.19}$$

where ρ_0 is the equilibrium density of the medium and c is the speed of sound in the medium. Because this is an important characteristic property of media it is called the *characteristic impedance*.

For plane, propagating waves the specific acoustic impedance will be real, but for standing waves between two walls, the incident and reflected pressures cannot be assumed perfectly in or out of phase. This leads to that the specific acoustic impedance must be assumed complex [8, p. 126], comprising the *specific acoustic resistance* and the *specific acoustic reactance*:

$$\boldsymbol{z} = r + jx \; . \tag{2.20}$$

Looking at the interface between two media, one can assume the boundary conditions continuity of pressure and continuity of the normal component of the particle velocity. This can also be expressed as the continuity of the *normal specific acoustic impedance* [8, p. 160]:

$$\boldsymbol{z}_n = \frac{p}{u\cos(\theta_i)} = r_n + jx_n \tag{2.21}$$

where θ_i is the incidence angle.

2.2.3 Oblique incidence absorption

Looking at reflection and transmission of sound pressure waves from one medium to another, the pressure reflection and transmission coefficients can be defined as

$$\begin{aligned} R &= \frac{p_r}{p_i} \\ T &= \frac{p_t}{p_i} \\ 1 &= T - R \end{aligned}$$

where p_i is the pressure of the incident wave, p_r is the pressure of the reflected wave and p_t is the pressure of the transmitted wave.

An oblique incidence sound pressure wave from one medium onto the surface of another is usually described using specular reflection and transmission: Assuming both media can be approximated to fluids and continuity of pressure and of the normal component of the particle velocity at the interface, R can then be calculated using the incidence angles and the characteristic impedances of the media [19, p. 83]:

$$R = \frac{\dfrac{Z_2}{\cos(\theta_t)} - \dfrac{Z_1}{\cos(\theta_i)}}{\dfrac{Z_2}{\cos(\theta_t)} + \dfrac{Z_1}{\cos(\theta_i)}} = \frac{Z_2\,\cos(\theta_i) - Z_1\,\cos(\theta_t)}{Z_2\,\cos(\theta_i) + Z_1\,\cos(\theta_t)} \tag{2.22}$$

where $Z_{1,2}$ is the characteristic impedance of the media, θ_i is the incidence (and reflection) angle and θ_t is the transmission angle. Letting the incidence angle approach $\theta_i = 90°$ leads to $|R| = 1$ for grazing incidence – meaning no sound wave transmission in medium 2 (the wall), ergo no sound absorption.

2.2.4 Locally reacting material

When medium 2 is solid, the velocity of the refracted wave is decomposed into a tangential and a normal component:

$$\begin{aligned} v_t &= \frac{c}{m_t} \\ v_n &= \frac{c}{m_n} \end{aligned}$$

where v_i is the velocity component in the solid, m_i is the average index of refraction and c is the speed of sound in air. Empirically, m_t is so much larger than unity as to be indistinguishable from infinity [12, p. 58]. This leads to $v_t << v_n$ and is expressed as the assumption that the material is *locally reacting*.

This is particularly common for anisotropic materials. For isotropic materials, the speed of longitudinal wave propagation in the material will be small compared to in the air [8, p. 161]. Combining this with Snell's law [19, p. 82] gives $\theta_t << \theta_i$. Assuming $\cos(\theta_t) = 1$ and using the complex normal specific impedance (2.21), it's possible to obtain the following expression for R:

$$R = \frac{r_n - \dfrac{Z_1}{\cos(\theta_i)} + jx_n}{r_n + \dfrac{Z_1}{\cos(\theta_i)} + jx_n}\,. \tag{2.23}$$

where normally $r_n >> Z_1$, which leads to $|R| = 1$ for $\theta_i = 90°$.

2.3 Sound absorbers

Sound absorbers are usually divided into two categories: porous absorbers and resonator absorbers. Common types of porous absorbers are mineral wool (or 'mineral fibre') and plastic foam. Plastic foam has an open cell structure, while mineral wool is made up of anisotropically oriented fibres with a diameter of a few microns [19, p. 156]. The air inside the material is moveable. When sound waves cause the air in the porous absorber to move, energy will be lost in the friction movement of the structure and converted to heat.

Resonator absorbers are mass-spring systems where sound waves cause the mass to oscillate. The energy will then dissipate through damping in the system. These systems work best around their resonance frequencies. One type of resonance absorber is the Helmholtz resonator, which is an air cavity with a small opening. The air in the opening works as a mass, and the air in the cavity works as a spring.

As this thesis concerns itself with porous absorbers, these will be examined in more detail.

2.3.1 The impedance at the absorber surface

For simplicity, normal incidence is assumed. A plane wave propagating parallel to the x-axis with normal incidence on a perfectly flat and rigid wall will have the specific acoustic impedance

$$\boldsymbol{z}_x = \infty \tag{2.24}$$

at the wall. Substituting the rigid wall for a heavy plate where some of the sound energy is transmitted through the plate, the plane wave will have the specific acoustic impedance

$$\boldsymbol{z}_x = j\omega m + \rho_0 c \tag{2.25}$$

where m is the mass of the plate.

The absorption coefficient can [19, p. 75] be expressed as

$$\alpha = 1 - \left|\boldsymbol{R}\right|^2 \tag{2.26}$$

and $\boldsymbol{R}$ relates to the specific acoustic impedance like this:

$$\boldsymbol{z}_x = \rho_0 c \frac{1+\boldsymbol{R}}{1-\boldsymbol{R}}\ , \tag{2.27}$$

relating the absorption coefficient to the specific acoustic impedance [19, p. 77]:

$$\alpha = \frac{4\,\Re\left\{\frac{\boldsymbol{z}_x}{\boldsymbol{Z}}\right\}}{\left|\frac{\boldsymbol{z}_x}{\boldsymbol{Z}}\right|^2 + 2\,\Re\left\{\frac{\boldsymbol{z}_x}{\boldsymbol{Z}}\right\} + 1}\,. \tag{2.28}$$

2.3.2 The Delany & Bazley model

The most popular model for describing the behaviour of porous absorbers is the empirical model by Delany & Bazley [19, p. 180]. This model describes the absorber by its complex characteristic impedance and complex wave propagation coefficient $\Gamma = j \cdot \boldsymbol{k}$:

$$\begin{aligned} \boldsymbol{Z} &= \rho_0 c\left\{1 + a\left(\frac{f}{\sigma}\right)^b - jc'\left(\frac{f}{\sigma}\right)^d\right\} \\ \boldsymbol{\Gamma} &= \frac{\omega}{c_0}\left\{p\left(\frac{f}{\sigma}\right)^q + j\left[1 + r\left(\frac{f}{\sigma}\right)^s\right]\right\} \end{aligned} \tag{2.29}$$

where σ is the airflow *resistivity*. Furthermore, a, c', p and r are the empirical coefficients of $(\frac{f}{\sigma})$ and b, d, q and s are the empirical degrees of $(\frac{f}{\sigma})$ [10, pp. 121-122]. The empirical coefficients and degrees have been revisited first by Miki and later by Komatsu.

Using the Delany-Bazley model with the Winflag simulation software (see Section 3.3) in the following setup

- air
- porous layer Delany-Bazley model, thickness d
- HARD WALL

gives the following illustration of absorption coefficient efficiency as function of frequency and thickness d of the absorber layer presented in Figure 2.2. Note that this simulation uses $\sigma = 10$ kPa s/m^2. As shown in the figure, absorption efficiency increases for increasing frequency and for increasing absorber thickness.

It's customary to approximate the frequency where the absorber approaches maximum effectiveness to $d \approx \dfrac{\lambda}{4}$ where λ is the wavelength of the sound. For the absorbers presented here, only the three thickest absorbers approach $\alpha \approx 1$ in the relevant frequency range. The three absorbers approach $\alpha \approx 1$ for the following frequencies:

- $d = 50$ mm $\Rightarrow f = \dfrac{c}{4 \cdot d} = 1715$ Hz
- $d = 100$ mm $\Rightarrow f = 857.5$ Hz
- $d = 500$ mm $\Rightarrow f = 171.5$ Hz

The α-plots for these three absorbers with the $d \approx \dfrac{\lambda}{4}$ frequencies marked can be seen in Figure 2.3. From this figure it's apparent that this approximation is better for increasing frequencies. It's also worth noting that the absorber thickness of 500 mm is unusual.

The fluctuations of the curves as they approach $\alpha = 1$ is caused by the absorber being finite in extent. An infinitely large absorber surface would not have the observed fluctuations.

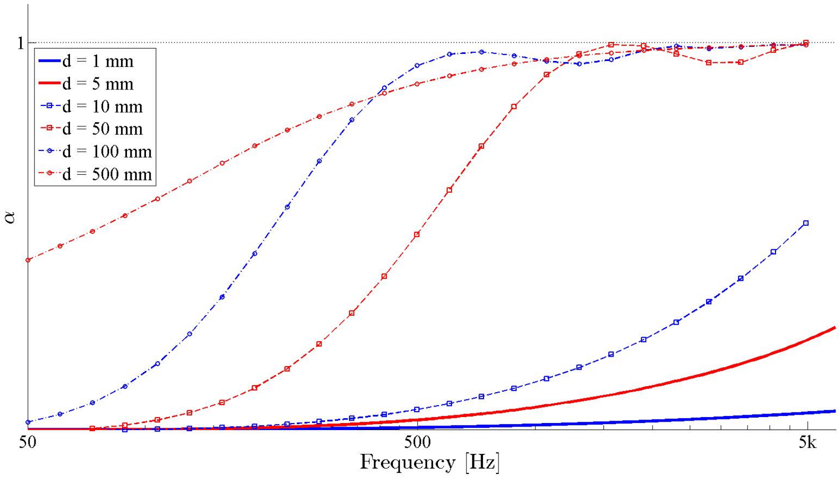

Figure 2.2: Simulated absorption coefficients for different absorber thicknesses using WinFlag & the Delany-Bazley model

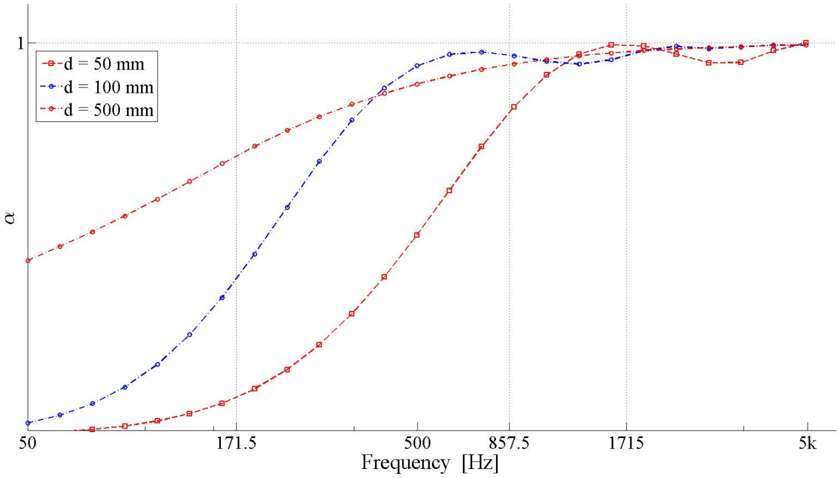

Figure 2.3: Simulated α using WinFlag & the Delany-Bazley model with the frequencies corresponding to $d = \dfrac{\lambda}{4}$ marked as vertical lines

2.4 Grazing incidence absorption

The principle of specular reflection that is commonly used for calculating oblique incidence absorption fails to describe the absorption of a grazing incidence sound wave, i.e. when $\cos(\theta) = 0$ in equations (2.22) and (2.23). These conventional approaches to sound absorption fail to describe the absorption characteristics of THE HARD CASE, as illustrated in Figure 1.1.

Note that for perfect conditions of smooth, flat walls that are infinitely hard, placed perfectly perpendicular to each other, assuming locally reacting surfaces and the room as an infinitely long tube, there would be no grazing incidence absorption.

Kinsler et al. [8, p. 350] has derived an expression for grazing incidence absorption based on equation (2.13) and a series of assumptions:

- Looking at a cuboid room with five perfectly rigid wall and one lossy wall at $x = L_x$, isolating the problem to 1D.
- The absorbing characteristics of the wall are determined by its normal specific acoustic impedance $\boldsymbol{z}_x$ (2.21). This makes the boundary conditions somewhat simpler to formulate.
- Neglecting the reactive part of the complex normal specific acoustic impedance (equation (2.20)) leads to the following expression:

$$\boldsymbol{z}_x = \rho_0 c\, v_x \tag{2.30}$$

where v_x is the dimensionless relationship between the impedance in the interface (parallel to the x-axis) and the characteristic impedance of air: $\boldsymbol{z}_n^{wall}$ / $\boldsymbol{Z}^{air}$.

The rest of the walls are perfectly rigid, giving the coefficients from equation (2.12):

$$\begin{aligned} \alpha_y = \alpha_z &= 0 \\ \phi_{all} &= 0 \\ \beta &= \beta_x \;. \end{aligned} \tag{2.31}$$

Solving the remainder of the $\left(\frac{\omega_D + j\beta}{c}\right)^2 = \mathbf{k}_x^2 + \mathbf{k}_y^2 + \mathbf{k}_z^2$ condition from equation (2.12) gives the real and imaginary parts of the expression as the boundary conditions for the grazing incidence absorption expressions:

$$\begin{aligned} k^2 - \alpha_x^2 &= \frac{\omega_D^2 - \beta_x^2}{c^2} \qquad &(2.32)\\ \beta_x &= k_x \alpha_x \frac{c^2}{\omega_D} \; . \qquad &(2.33)\\ & &(2.34) \end{aligned}$$

The boundary condition $\boldsymbol{z}_x = \dfrac{\boldsymbol{p}}{\boldsymbol{u}_x} = \rho_0 c\, v_x$ at $x = L_x$ gives

$$\tan\left[\left(k_x + j\alpha_x\right) L_x\right] = j \frac{1}{v_x} \frac{\left(\omega_D + j\beta_x\right)/c}{k_x + j\alpha_x} \; . \tag{2.35}$$

For all normal modes, the nearly rigid wall leads to the approximation $k_x L_x \approx n_x \pi$. Applying this and series expansion to the left hand side, equation (2.35) can be rewritten:

$$\begin{aligned} \left(k_x L_x - n_x \pi\right) + j\alpha_x L_x &= j \frac{1}{v_x} \frac{\left(\omega_D + j\beta_x\right)/c}{k_x + j\alpha_x}\\ n_x &= 0, 1, 2... \; . \end{aligned} \tag{2.36}$$

Looking at equation (2.36) for grazing modes ($n_x = 0$), the imaginary part can be written as

$$2 L_x k_x \alpha_x = \frac{\omega_D}{c v_x} \; , \tag{2.37}$$

which when substituted into equation (2.34) gives the expression for $\beta_{grazing}$ as

$$\beta_{grazing} = \frac{1}{2} \frac{c}{v_x l_x} \; . \tag{2.38}$$

Looking at equation (2.36) for non-grazing modes ($n_x \neq 0$), the imaginary part can be written as

$$\alpha_x k_x L_x + \alpha_x \left(k_x L_x - n_x \pi\right) = \frac{\omega_D}{c v_x} \; . \tag{2.39}$$

Assuming $k_x L_x = n_x \pi$ to be a reasonable assumption for lower order modes and substituting the resulting expression into equation (2.34) gives the expression for $\beta_{non-grazing}$ as

$$\beta_{non-grazing} = \frac{c}{v_x l_x} \; , \tag{2.40}$$

which is then assumed valid for lower order modes.

Comparing equations (2.38) and (2.40) reveals the relation

$$\beta_{non-grazing} = 2 \cdot \beta_{grazing} \; . \tag{2.41}$$

For convenience, equations (2.38) and (2.40) are rewritten expressing β as a function of the impedance using equation (2.30):

$$\begin{aligned} \beta_{normal} &= \frac{c}{\frac{\boldsymbol{z}_x}{\rho c} \cdot L_x} \\ \beta_{grazing} &= \frac{1}{2} \frac{c}{\frac{\boldsymbol{z}_x}{\rho c} \cdot L_x} \; . \end{aligned} \tag{2.42}$$

2.4.1 The inverse proportionality of T and β

Equation (2.5) expresses the sound pressure as a sum of cosines multiplied by a temporal factor:

$$\boldsymbol{p}^D_{n_x n_y n_z} \propto e^{j\boldsymbol{\omega}_D t} = e^{j(\omega_D + j\beta)t} \tag{2.43}$$

so that the dependence of $\boldsymbol{p}$ on β can be expressed as:

$$\boldsymbol{p}^D_{n_x n_y n_z} \propto e^{-\beta t} \; . \tag{2.44}$$

As described in Section 2.5, the reverberation time T is the time it takes the sound pressure to decrease by 60 dB. Decibel is defined as $20 \log_{10} (p/p_{reference})$, which gives a decrease in pressure by 60 dB as the decrease to $1/1000$. This can be expressed using equation (2.44) as

$$\Delta \boldsymbol{p} = \frac{1}{1000} = e^{\beta T_{60}} \; , \tag{2.45}$$

or

$$T_{60} = \frac{\ln(1000)}{\beta} \; , \tag{2.46}$$

showing the inverse proportionality of T and β. Revisiting equations (2.38) and (2.40) shows how the reverberation time of grazing modes will be twice that of non-grazing modes:

$$T_{grazing} = 2\, T_{non-grazing} \tag{2.47}$$

2.4.2 Alternative approach

An alternative theoretical approach to absorption as a function of incidence angle was presented by Sven-Ingvar Thomasson in 1982 [17]. His approach provides an expression for the absorption coefficient which does not include the cosine function and consequently does not approach zero for incidence angles $\theta \Rightarrow 90°$.

This expression behaves somewhat like THE HARD CASE, in that the absorption approaches $\overline{\alpha} \Rightarrow 1$ for ca. 400 Hz, just like in Figure 1.1. However, this expression does not predict the steep drop in absorption observed at high frequencies in THE HARD CASE, but rather a gradual decrease to $\overline{\alpha} \approx 0.5$ at ca. 3 kHz.

Consequently, Thomasson's expressions have been omitted, even if they're mentioned here to point out how the expressions in Section 2.4 are not the only ones describing grazing incidence absorption.

2.5 Statistical room acoustics

Above the Schröder frequency (equation (2.9)) the modal overlap makes single modes indistinguishable. In this frequency region the wave theoretical room acoustics (Section 2.1) cannot describe the properties of the room. The statistical approach is much easier to work with and above the Schröder frequency it is highly accurate.

Statistical room acoustics can also be used below the Schröder frequency, but as the mode density decreases, so does the statistical accuracy.

2.5.1 Reverberation time

The reverberation time, T, was developed by Sabine in the the 1890s and is defined as the time it takes for the sound pressure level to decrease by 60 dB after the sound source ceases. Sabine's equation for T is an empirical relation between the reverberation time of the room, the volume of the room and the absorbing characteristics of the room's surfaces [8, p. 338]:

$$T_{Sabine} = \frac{24 \cdot \ln(10)}{c} \frac{V}{A + 4mV} = \frac{0.161V}{S\bar{\alpha_S} + 4mV} \ . \tag{2.48}$$

Here, c is the speed of sound, V is the volume of the room, S is the surface area of the room, $\bar{\alpha_S}$ is the (*Sabine*) mean sound absorption coefficient and m is the energy attenuation coefficient for sound pressure waves travelling through air. The term $4{\cdot}m{\cdot}V$ consequently represents energy absorption in air. Notice how the absorption area A has been replaced by the product of the surface area S and the mean absorption coefficient $\bar{\alpha_S}$ in the final expression.

T_{Sabine} assumes a diffuse sound field. For sufficiently diffuse sound field conditions, $\bar{\alpha_S}$ will range between 0 for perfectly hard, 100 % reflecting surfaces and 1 for perfectly soft, 100 % absorbing surfaces. However, for increasingly non-diffuse sound field conditions, the absorption coefficient α_S can become larger than 1.

Kinsler et al [8, p. 338] gives an approximation of the attenuation coefficient for air absorption as

$$m = 5.5 \cdot 10^{-4} \left(\frac{50}{RH}\right) \left(\frac{f}{1000}\right)^{1.7} \tag{2.49}$$

where RH is the relative humidity of the air given in percent, f is the frequency and the expression (2.49) is *sufficiently accurate* for relative humidities ranging from 20 - 70 % and in the frequency range 1.5 - 10 kHz. As $m \sim \left(\frac{f}{1000}\right)^{1.7}$, air absorption constitutes a negligible error for frequencies below 1.5 kHz. Since the measurements performed in this particular project has an upper frequency limit of 1 kHz, air absorption will be neglected.

The Sabine equation (2.48) assumes a diffuse sound field, where the sound energy density is the same in every point in the room. It will give $T > 0$ even for values of $\bar{\alpha}$ approaching and equal to 1. The most common improvement to the Sabine equation is the Eyring reverberation time, which is based on the mean free path between reflections:

$$T_{Eyring} = \frac{0.161V}{-S\ln(1-\bar{\alpha_E}) + 4mV} \; . \tag{2.50}$$

As long as $\bar{\alpha}_{Sabine}$ calculated from equation (2.48) is allowed to exceed 1, it is possible to directly derive the corresponding $\bar{\alpha}_{Eyring}$ [1, p. 1409].

2.5.2 Measuring the reverberation time

Comparing the signal sent to the loudspeaker with the signal received from the microphone using a Fourier transform gives the transfer function $H(\omega)$ and impulse response $h(t)$ of the room. Integration of the impulse response by the following expression

$$E(t) = \int_{\tau}^{\infty} h^2(t)\, dt \tag{2.51}$$

will give the energy decay $E(t)$ from the time $t = \tau$ [19, p. 107]. The energy decay curve, also called the Schröder curve, shows the decay of the sound pressure energy in the room as a function of time and is used for estimating the reverberation time by using a least squares fit line. A sketched Schröder curve can be seen in Figure 2.4.

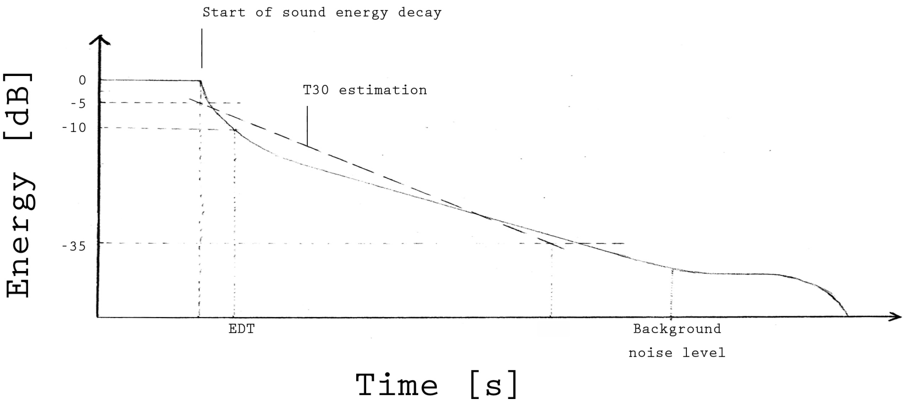

Figure 2.4: Sketch of Schröder curve

As the situation of having a test signal more than 60 dB stronger than the background noise floor is unusual and impractical, the measurement of T will usually involve extrapolating the fitted line based on different parts of the decay slope:

- T_{60} denotes a fitted line based on the dynamic range from 0 to -60 dB.
- T_{30} is the most common substitute for T_{60}. T_{30} uses the dynamic range from -5 dB to -35 dB to extrapolate the line. The T_{30} value will then be twice the time it takes for the sound energy to decay from -5 to -35 dB.
- As an alternative to T_{30}, T_{20} uses the dynamic range from -5 dB to -25 dB.
- Lastly there's *Early Decay Time* (EDT), which uses the dynamic range from 0 to -10 dB.

2.5.3 Decay curve linearity

For a perfectly straight line Schröder curve, $T_{20} = T_{30}$. Measuring $T_{20} \approx T_{30}$ is an indication of a diffuse sound field. In most normal situations, $T_{20} \neq T_{30}$ and T_{20} is then often used as an alternative to T_{30} because T_{20} will favour earlier reflections more than T_{30} will. The early reflections have greater influence on the perceived acoustics of a room, and EDT is sometimes included in addition to T_{20} or T_{30} for this reason.

The curvature parameter C gives the percentage the Schröder curve deviates from a straight line by the following expression:

$$C = 100 \cdot \left(\frac{T_{30}}{T_{20}} - 1 \right) \; [\%] \tag{2.52}$$

where C has typical values between 0 % and 5 %. Higher values than 10 % indicate a far from straight line decay [6, p. 15]. In other words, the curvature parameter reveals whether or not the calculated T is mainly dependent on the chosen dynamic range. In cases of strongly non-diffuse fields (e.g. THE HARD CASE) $T_{30} \neq T_{20}$, $C \neq 0$ and the calculated T is to a high degree dependent on which dynamic range is chosen for the calculation.

In other words, the curvature parameter is a good way to identify a possible HARD CASE room. Examples of non-straight Schröder curves can be seen in Figures 3.6b, 4.6 and in Appendixes A.4 and A.6.

2.6 The Fourier transform & filtering

2.6.1 The Fourier transform

The Fourier transform is defined [11, p. 519] as

$$F\left(\omega\right) = \mathcal{F}\Big\{ f(t) \Big\} = \frac{1}{\sqrt{2\pi}} \int_{-\infty}^{\infty} f(t)\, e^{-j\omega t} dt \; . \tag{2.53}$$

Letting $h(t)$ be the recorded impulse response, the length of $h(t)$ is called the *duration D*, and the width of the spectrum of the transfer function $H(\omega)$ is called the *bandwidth B*. Because the duration and the bandwidth have a reciprocal relationship, the duration-bandwidth product is constant [4, p. 233]:

$$\Delta t \cdot \Delta\omega = C \tag{2.54}$$

where C is a constant. This is called the *uncertainty relation* and implies a wide envelope $\Delta\omega$ for short Δt and vice versa.

2.6.2 The filterwidth

Isolating a mode f_c in the frequency spectrum of $H(\omega)$ using a bandpass filter $\Delta f = f_c \pm B/2$ with a chosen filter bandwidth (or *filterwidth*) B, will lead to the fourier-transformed time signal $h(t)_{\triangle f}$ having an envelope Δt.

The envelope Δt will distort the energy decay curve $E(t)$ (2.51) unless the impulse response of the filter is much shorter than the impulse response of the system under test [7, p. 187]. For $E(t)$ to remain acceptably un-distorted, the bandwidth B of the filter has to fulfill the following requirement:

$$B \cdot T_{60} > 4 \tag{2.55}$$

where T_{60} is the reverberation time of the system under test [7, p. 188].

2.6.3 The transform properties of $p(\chi, t)$

The homogeneous wave equation is derived to the expression for the sound pressure $p(x, y, z, t)$ given in equation (2.14). Including a source term, it can be shown [2, p. 94] that equation (2.14) can be expressed on the following form

$$p(\chi, t) = C \cdot \Sigma_{mnq} \mathbf{\Lambda}_{mnq} \mathbf{\Phi}\left(\chi_s\right) \mathbf{\Phi}\left(\chi\right) \cos\left(\omega_{mnq} t\right) e^{-\delta_{mnq} t} \tag{2.56}$$

where C is a constant, $\mathbf{\Lambda}_{mnq}$ is proportional to $\boldsymbol{A}_{n_x n_y n_z}$ in equation (2.14), $\mathbf{\Phi}\left(\chi_s\right)$ is the cosine expression for the sound source point, $\mathbf{\Phi}\left(\chi\right)$ is the cosine expression for the receiver point, δ_{mnq} is the damping factor, and $n_x n_y n_z$ has been substituted with mnq and (x, y, z) with χ for a more economic expression.

Equation (2.56) has a Fourier transform that can be expressed like this [2, p. 93]:

$$p(\chi, \omega) = C \cdot \Sigma_{mnq} \mathbf{\Lambda}_{mnq} \frac{\mathbf{\Phi}\left(\chi_s\right) \mathbf{\Phi}\left(\chi\right)}{\omega^2 - \omega_{mnq}^2 \pm 2j\delta_{mnq}} e^{j\omega t} \ . \tag{2.57}$$

2.7 Scale model considerations

Using a scale model for measurments entails some considerations when comparing results to full-scale measurements.

Using scale model ratio of 1:X, the wavelength in the scale model becomes

$$\lambda_{scale\ model} = \frac{\lambda_{full\ scale}}{X} \ . \tag{2.58}$$

Using $f = \frac{c}{\lambda}$ gives the frequency relationship

$$f_{scale\ model} = X \cdot f_{full\ scale} \tag{2.59}$$

between the scale model and full scale measurements. Equation (2.48) then gives the following relationship for T:

$$T_{scale\ model} = 0.161 \frac{V_{scale\ model}}{A_{scale\ model}} = 0.161 \frac{\frac{V_{full\ scale}}{X^3}}{\frac{A_{full\ scale}}{X^2}} = \frac{T_{full\ scale}}{X}\ . \tag{2.60}$$

Chapter 3

Measurements

This chapter presents the scale model and sound absorber used. The measurement setup and equipment are described and measurement methods are elaborated.

3.1 Description of the scale model

The scale model is a box made of 18 mm plywood with inner dimensions $L_x \times L_y \times L_z = 1.47 \times 2.37 \times 0.85$ m^3. With a scale factor of 1:4, this scales up to a room of dimensions 5.9×9.5×3.4 m^3. This is a realistic room size, easily comparable to rooms on the NTNU campus. A sketch of the scale model is included in Figure 3.1.

The absorber used with the scale model box is a plastic foam absorber of 50 mm thickness. This absorber was installed in the box with a 50 mm gap between the absorber and the actual box ceiling. Note how the apparent height inside the box is 10 cm less with the absorber installed. This has been taken into account when calculating the volume and dimensions of the box – making $L_z = 0.75$ m with the absorber installed.

3.1.1 Comments on modes

Previous measurements in the box conducted by Bjørn Kolbrek [9] showed all modes in the box corresponding very well with the theoretical calculation of modes in a box of those dimensions – with the exception of the first mode. This indicates that the walls of the box are not perfectly stiff. Still, the approximation of 'hard walls' is a

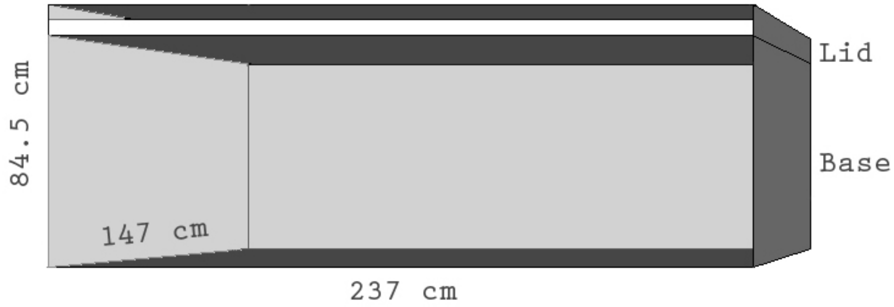

(a) Sketch of scale model box

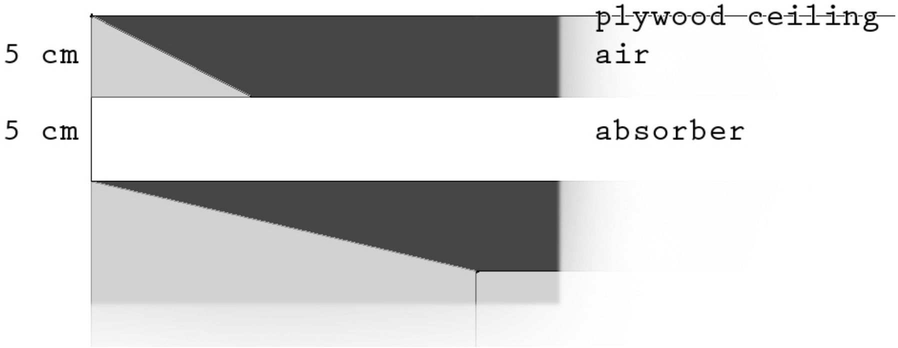

(b) Sketch detail of absorber ceiling

Figure 3.1: Sketch of scale model box with detail

reasonably good one. Using equation (2.7), the theoretical first mode in the box is the $[n_x \, n_y \, n_z] = [1\,0\,0] = 72$ Hz mode and the second is the $[0\,1\,0] = 117$ Hz mode.

Previous measurements in the box conducted by Jakob Vennerød [18, p. 12] identified a peak in T in the 315 Hz 1/3 octave band, which disappeared when the two short-side walls were reinforced by wooden beams connecting them to the surrounding concrete structure. This reinforcement has also been made for the present study.

3.1.2 Measurement frequency range

With previous measurements of the reverberation time in the scale model box by the author [5, p. 20] as basis, T can be approximated across frequencies to roughly 1.5 s. Equation (2.9) and gives the Schröder frequency

$$f_s \approx 2000 \cdot \sqrt{\frac{1.5}{2.37 \cdot 1.47 \cdot 0.85}} = 1423 \text{ Hz} \tag{3.1}$$

and equation (2.11) the upper limit of the few mode region

$$f_{new} \approx 900 \cdot \sqrt{\frac{1.5}{2.37 \cdot 1.47 \cdot 0.85}} = 640 \text{ Hz} . \tag{3.2}$$

As these are statistical boundaries and not 'hard limits', the frequency range of the measurements has been chosen to 100 Hz - 1000 Hz.

3.2 The measurement setup

To be able to calculate the T of a single mode, it's necessary to filter out all the parts of the transfer function $H(\omega)$ that is not the relevant mode. However, equation (2.55) relates a lower limit to how narrow the filter can be without distorting the calculations. It is therefore necessary to obtain a sufficiently high degree of separation between modes, so that the filter does not include more than one mode. This can be done by suppressing some of the modes, while looking at the other ones.

As elaborated in Section 2.1.2, the odd modes will all have a node half-way between the relevant walls. Placing the sound source and the receiver at $i = L_i/2$ will suppress the modes $n_i = 1, 3, 5...$ where $i = x, y, z$. Similarly, every other even mode will have nodes a quarter-distance from the relevant walls. Placing the sound source and the receiver at $i = L_i/4$ or $i = 3 \cdot L_i/4$ will suppress the modes $n_i = 2, 6, 10...$

This leads to the following sound source and receiver placements:

1. Source & receiver at $x = L_x/2$, suppressing the modes $n_x = 1, 3, 5...$

2. Source & receiver at $x = L_x/4$, suppressing the modes $n_x = 2, 6, 10...$
3. Source & receiver at $y = L_y/2$, suppressing the modes $n_y = 1, 3, 5...$
4. Source & receiver at $y = L_y/4$, suppressing the modes $n_y = 2, 6, 10...$

All four positions were used in all measurements (see Section 3.4). The source & receiver placements in the scale model are shown in Figure 3.2.

For the primary measurements, both the source and the receiver were mounted 50 cm above the floor. For the secondary measurements the source was mounted 50 cm above the floor and the receiver was mounted first at 1 cm below the absorber ceiling, second at 10 cm below the ceiling and last at 20 cm below the ceiling.

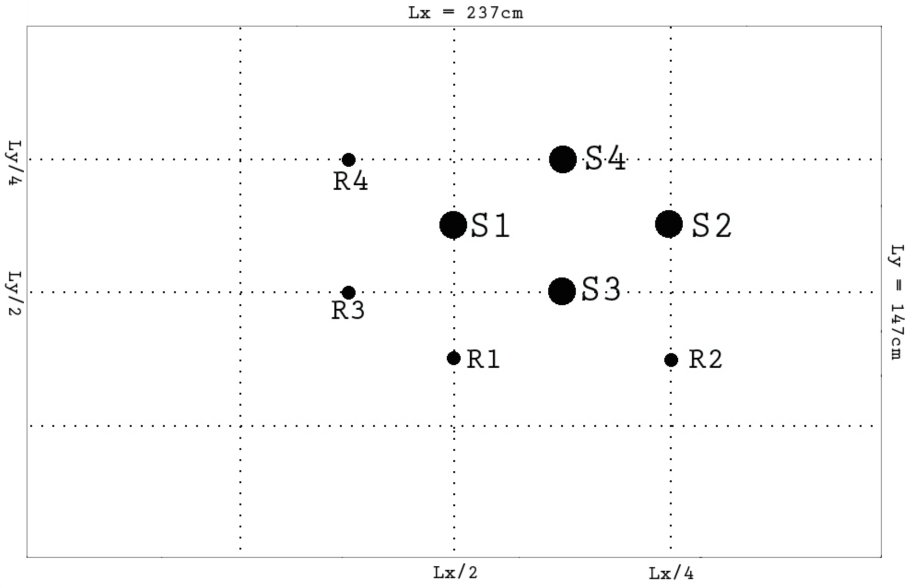

Figure 3.2: Schematic diagram of measurement positions in the scale model. S marks sound source and R marks sound receiver

3.3 Measurement equipment

The sound source used was a 2” AuraSound driver mounted on a sealed aluminium pipe. The loudspeaker rolls off with $\sim$12 dB/oct below 200 Hz in free field, and is omni-directional within $\pm$ 1 dB below 1 kHz [18, p. 57].

The receiver used was a Microflown USP Regular. The reason for using this microphone is that it can record the particle velocity components in 3D – u_x, u_y and u_z, as well as the pressure p.

Because the modes are also decomposable into x, y, z-components this ability in the sound probe was thought to be an advantage in achieving good mode separation in the Primary approach measurements (see Section 3.4.1). For the Additional approaches measurements, the probe was used to record both the impulse responses $p(t)$ and $u_z(t)$ (see Section 3.4.2).

The p channel of the microphone has a corner frequency at 180 Hz, which means it will function like a 2nd order high-pass filter, rolling off with -3 dB at 180 Hz. The u_z channel of the microphone has a corresponding corner frequency at 440 Hz. Note that this will cause transfer functions to appear slightly too low in the lower frequencies, but it will not influence the estimates of T, and is considered insignificant for this study.

Software

WinMLS 2004 was used to measure impulse responses in the room by the sine sweep method. Furthermore, it was also used to calculate T by 1/3 octave band frequencies. The sweep time of the sine sweep was set to the maximum 100 seconds. This is because averaging several shorter sweep measurements underestimate the energy of the reverberation tail and the high frequencies of the signal, as well as providing significantly poorer SNR [3, p. 16]. The sampling frequency was set to 48 kHz and the length of the impulse response was set to 6 seconds.

Post-calculation and plotting was done with MATLAB R2014a. Some simulations were also performed in WinFlag – a Norwegian program for calculation of sound absorption, impedance and sound reduction index of layers of different construction materials by the matrix method [20, p. 4].

Equipment list

The list in Table 3.1 includes all equipment in the measurment chain used in the measurements described in Chapter 3. A thermometer and hygrometer were included to monitor room temperature and relative humidity in the air.

Device	Manufacturer	Model	Serial Number
Loudspeaker	AuraSound	NSW2-326-8A	N/A
Power amplifier	Quad	50E	11852
Microphone	Microflown Technologies	USP Regular	UR-900843
Signal Conditioner	Microflown Technologies	MFSC-4	SC4-900843
USB sound card	AXYS	D-audio	009900086
Software	Morset Sound	WinMLS 2004	N/A
Laptop	DELL	Vostro 3550	DQ18BR1

Table 3.1: Signal chain elements

The sound source and receiver are presented in Figure 3.3.

3.4 Method

3.4.1 Primary approach

Estimating modal T

For the primary approach, the primary setup with both sound source and receiver mounted 50 cm above the floor was used. The impulse response of the scale model box was recorded measuring p, u_x, u_y and u_z for each measurement position. However, the WinMLS software is not able to record four separate channels simultaneously, which lead to the four different impulse responses being recorded sequentially.

The reason for recording all four different impulse responses was to be able to pick the one with the best mode separation and SNR. Checking the SNR was done directly in WinMLS where SNR is presented in 1/3 octave bands. Since the loudspeaker rolls off with 12 dB/oct below 200 Hz, the lowest bands will usually have the worst SNR. Discounting the first mode (see Section 3.1.1) the lowest relevant mode is the [0 1 0] mode at $f = 117$ Hz. This is in the 125 Hz 1/3 octave band, which spans 112-141 Hz. Consequently, the 125 Hz band will usually be the band with the worst SNR (of the bands that are of interest).

The 1/3 octave band SNR values for measurement position 1 is presented in Table 3.2. The SNR tables for the all four positions are included in Appendix A.1.

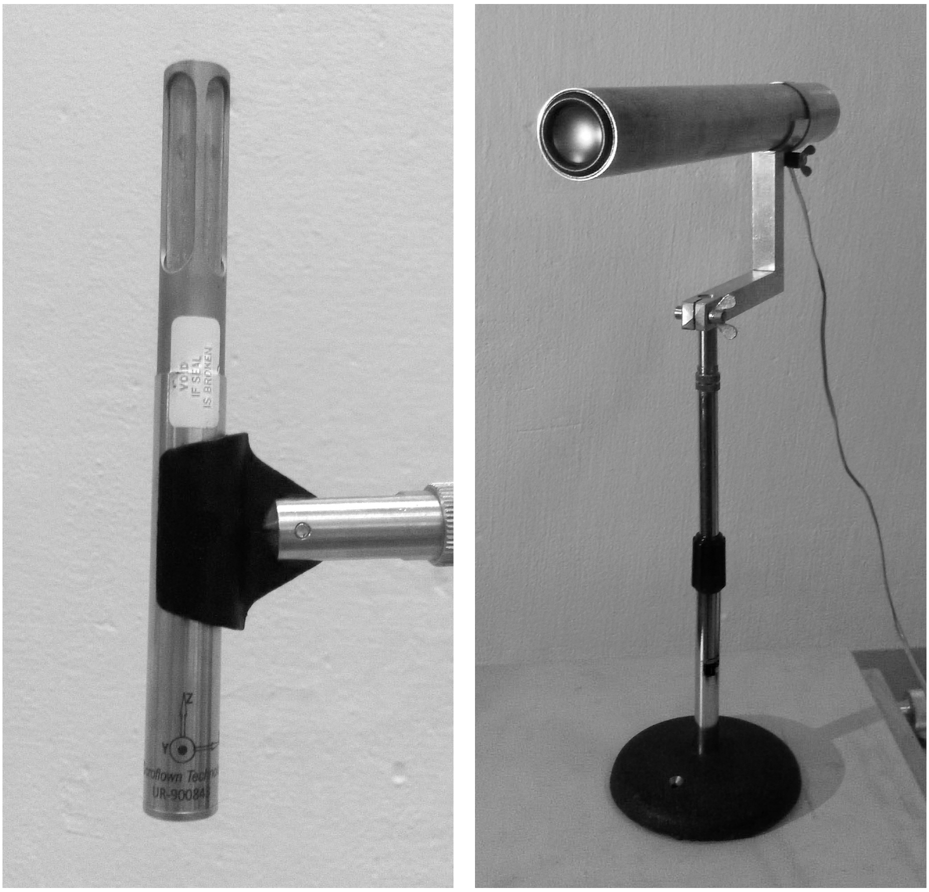

(a) Microflown Probe

(b) Pipe loudspeaker on stand

Figure 3.3: Sound source and receiver

As Table 3.2 shows, $p(t)$ had better SNR than the impulse responses using the particle velocity components had. Consequently, all further measurements and processing were done using $p(t)$. To increase the empirical foundation and to account for inaccurate sound source and receiver placement, $p(t)$ for positions 1-4 was recorded three

f [Hz]	SNR (p)	SNR (u_x)	SNR (u_y)	SNR (u_z)
100	23.3	12.4	26.1	4.8
125	45.4	19.6	30.0	20.7
160	50.6	24.8	34.9	25.8
200	45.5	27.0	37.8	32.0
250	54.5	31.0	40.5	33.2
315	55.4	26.0	35.7	27.2
400	54.7	21.7	36.9	31.2
500	59.1	20.7	37.2	31.1
630	56.7	21.3	35.2	27.8
800	55.7	22.7	34.5	25.1
1k	59.0	25.1	33.1	24.8

Table 3.2: Signal-to-noise ratio for measurement position 1 [dB] in 1/3 octave bands

times. The source and receiver were placed in each position individually for each of the three measurement serieses.

WinMLS was then used to calculate T in 1/3 octave bands and these T-values were used in conjunction with equation (2.55) to determine the frequency dependent filterwidth B.

The impulse responses $p(t)$ were used to calculate the transfer functions $H_p(\omega)$. The prominent mode peaks of the transfer function were identified, selected and filtered. The least number of prominent peaks across all transfer functions (in the relevant frequency range of 100-1000 Hz) were 17, and so for simplicity 17 peaks were selected from each transfer function. Figure 3.4 shows an example of a prominent mode peak in a transfer function. Note how the part of the transfer function included in the filter is marked red.

The filter used was a 2nd order butterworth filter which has a 12 dB/octave roll-off. This was run both backwards and forwards – in practice creating a 4th order filter with 24 db/octave roll-off. Running the filter backwards reduces unwanted influences from the filtering process considerably [7, p. 187]. Running the filter both backwards and forwards eliminates any phase shift errors.

An illustration of the filter can be made using the normalized dirac δ-function, which has the value 1 at a single point and is zero everywhere else. Running the filter on this function is a good illustration both of the filter, and the uncertainty relation from Section 2.6. The dirac δ-function is plotted in Figure 3.5a and the filtered dirac in Figure 3.5b.

The filtered impulse response was cropped to eliminated background noise, the

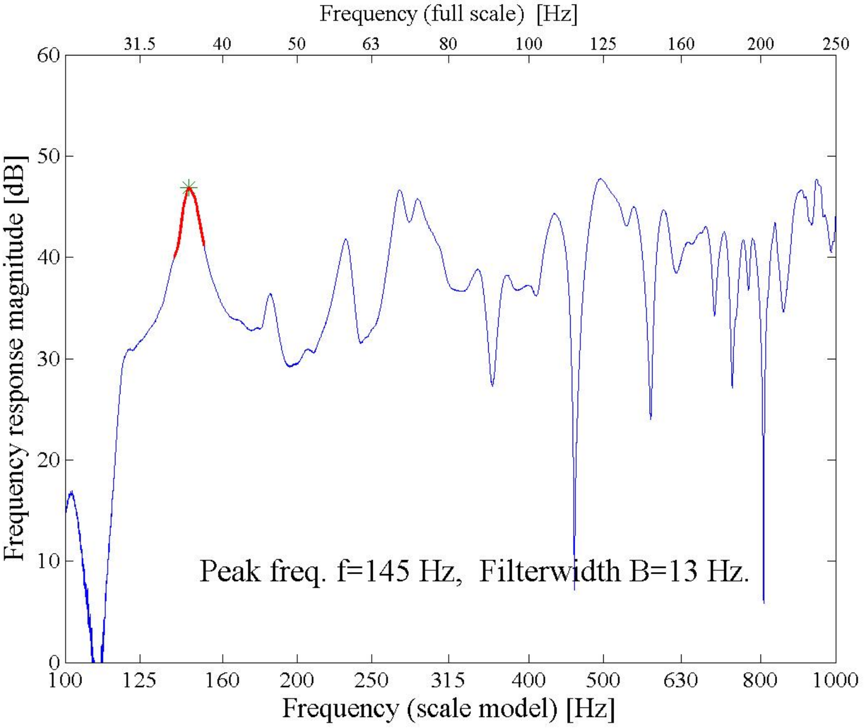

Figure 3.4: Transfer function $H_{p,1}$ with a selected mode peak and its filter

resulting energy decay curve was plotted and optimal linear decay was chosen. This linear decay was then used to determine the T of the mode. An example of the cropped impulse response can be seen in Figure 3.6a and an example of the corresponding energy decay line fit is shown in Figure 3.6b.

Checking the influence of the filterwidth

The filter used on the transfer functions in the primary approach has a lower limit bandwidth given by equation (2.55) that lets $E(t)$ remain acceptably un-distorted. It would be of interest to investigate how T varies as a function of filterwidth, to check if this lower limit is visible in the present measurements.

To check the filterwidth, a mode peak with good SNR and reasonable frequency-spacing to other modes was selected. The filtering and curve fitting described above

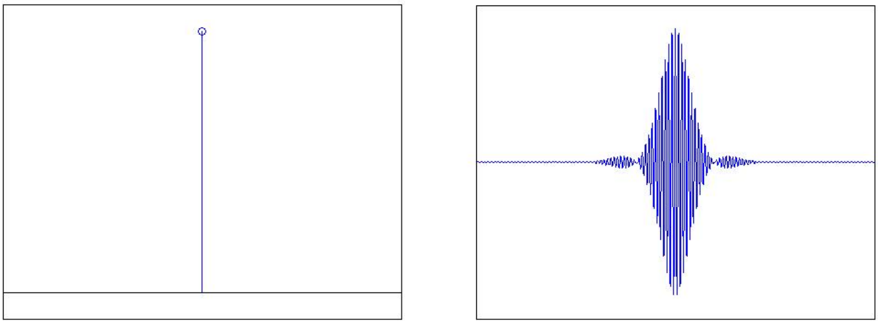

(a) A dirac δ-function **(b)** The filtered dirac δ-function

Figure 3.5: Dirac delta-function in an arbitrary A-space and filtered delta-function in the inverse A^{-1} space

was then applied to the selected mode for 14 different filterwidths ranging from 3 Hz to 38 Hz.

3.4.2 Additional approaches

These approaches are based on the continuity of acoustic pressure $\boldsymbol{p}$ and normal component of the particle velocity $\boldsymbol{u}$ at the interface between two media – the air and the wall. This means (by way of equation (2.18)) that the specific acoustic impedance in the air at the interface between air and wall will be the same as in the wall at the interface.

In other words, the specific acoustic impedance of the ceiling absorber can be found by measuring the impulse responses $\boldsymbol{p}$ and $\boldsymbol{u}_\perp$ in the air right next to it.

Calculating T based on measurements of the absorption coefficient β

The microphone was placed 1 cm below the absorber ceiling, as described in Section 3.2, and the impulse responses $\boldsymbol{p}(t)$ and $\boldsymbol{u}_z(t)$ were used via the transfer functions $H_p(\omega)$ and $H_{u_z}(\omega)$ to find the specific acoustic impedance:

$$\boldsymbol{z}_z = \frac{H_p(\omega)}{H_{u_z}(\omega)} \, . \tag{3.3}$$

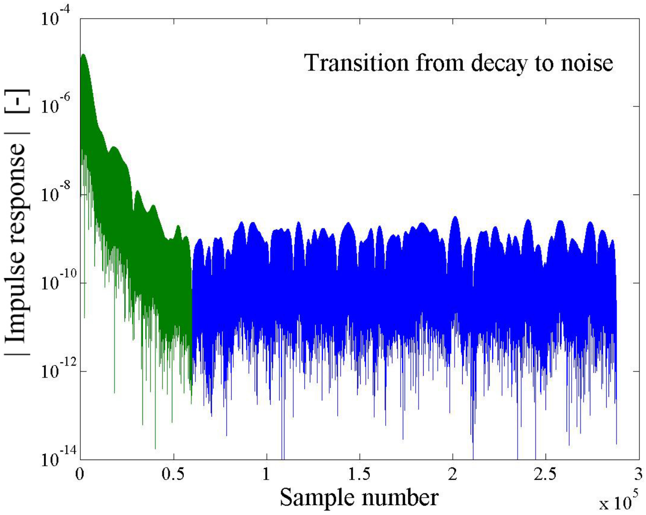

(a) Cropped impulse response noise floor transition

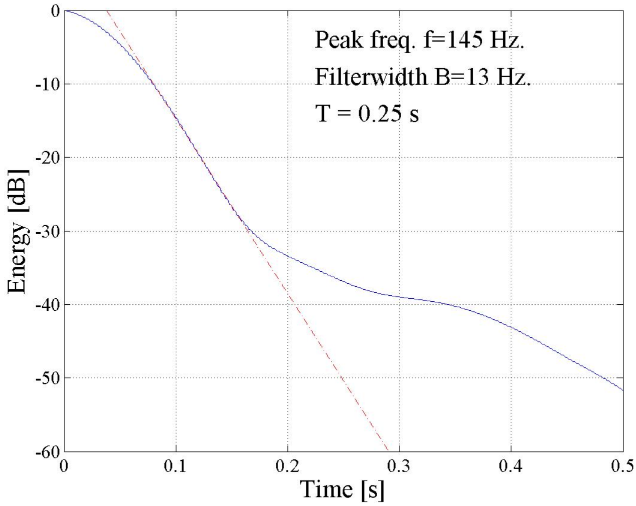

(b) Energy decay curve and fitted line for the chosen mode peak

Figure 3.6: Cropped impulse response & energy decay with linear regression for the selected mode peak

Inserting equation (3.3) into equation (2.42) leads to β expressed by the transfer functions of the measurements:

$$\begin{aligned}\beta_{normal} &= \frac{c}{\dfrac{H_p \cdot H_{ux}^*}{\rho c \left|H_{ux}\right|^2} \cdot L_x} \\ \beta_{grazing} &= \frac{1}{2}\frac{c}{\dfrac{H_p \cdot H_{ux}^*}{\rho c \left|H_{ux}\right|^2} \cdot L_x}\end{aligned}$$

Note how the numerator and denominator of the specific acoustic impedance from equation (3.3) has been multiplied with the complex conjugate of the denominator to achieve a real denominator.

T is found by inserting equation (3.4) into equation (2.46).

Sound intensity and the absorber

For the second part of the Additional approaches, the microphone was placed at distances $d = 1$, 10 and 20 cm below the absorber ceiling, as described in Section 3.2, and the impulse response of the scale model was recorded using p and u_z.

The intensity component $I_z(d)$ was then calculated for all 12 points, as elaborated in Section 2.2.1. Because the sound pressure varies a lot across the space of the room as described in Sections 2.1.2 and 2.1.3, normalization was attempted by the following procedure: The transfer functions $H_{p,1-12}$ from the 12 measurement positions were averaged as shown in the following expression:

$$\overline{H_p} = \frac{\left|H_{p,1} \cdot H_{p,1}^*\right| + ... + \left|H_{p,12} \cdot H_{p,12}^*\right|}{12} \, , \tag{3.4}$$

leading to the normalized z-componen of the intensity:

$$I_{z,i}^{norm} = \frac{I_{z,i}}{\overline{H_p}} \quad , \quad i = 1, 2...12 \, . \tag{3.5}$$

3.4.3 WinFlag simulations

Using the Delany-Bazley model (see Section 2.3.2), The WinFlag simulation software is able to predict the absorbing properties of an absorber for a given sound incidence angle, over a frequency range f, for a given flow resistivity σ. Previous measurements by the author using a standing wave tube [5, p. 33] determined $\sigma = 4.2$ kPa s/m^2 for the porous absorber.

The WinFlag simulations were performed with the following setup:

- air
- porous / Komatsu (50 mm, $\sigma = 4.2$)
- air (50 mm)
- HARD WALL

where 'porous / Komatsu' signifies a 50 mm thick layer of porous absorber with airflow resistiviy 4.2 kPa s/m^2, modeled by the Komatsu version of the Delany-Bazley equations.

These simulations are presented as part of the argument in Section 5.2.1.

Chapter 4

Measurement results

This chapter presents the measurement results. These include the estimations of T for single modes and the test results from the filter that was used to attain the modal T estimations. Furthermore, calculated values of T based on the theoretical expressions for grazing incidence are included as well as measurements of the vertical component of the sound intensity I_z as function of distance to the absorber.

Note how only the main result of the estimated T for all processed single modes have been included in its entirety. This is the Figure 4.3. The rest of the results are presented in representative samples. The measurement results are elaborated in much greater detail in the appendices.

4.1 Primary approach

4.1.1 Estimation of modal T

For the primary approach estimating T for modal peaks, the method described in Section 3.4.1 was used. The recorded transfer function using $p(t)$ for position 1 and measurement series 1 is shown in Figure 4.1 as an example of the recorded transfer functions. All 12 transfer functions can be found in Appendix A.2.

The transfer functions shown in Figure 4.1 and Figure A.1 were used by WinMLS to calculate 1/3 octave band T_{30} values. The filterwidths B used for modal estimation of the mode peaks in Figure 4.1 were calculated from these T_{30} values. The T_{30} values and corresponding filterwidths B for measurement series 1 are shown in Figure 4.2.

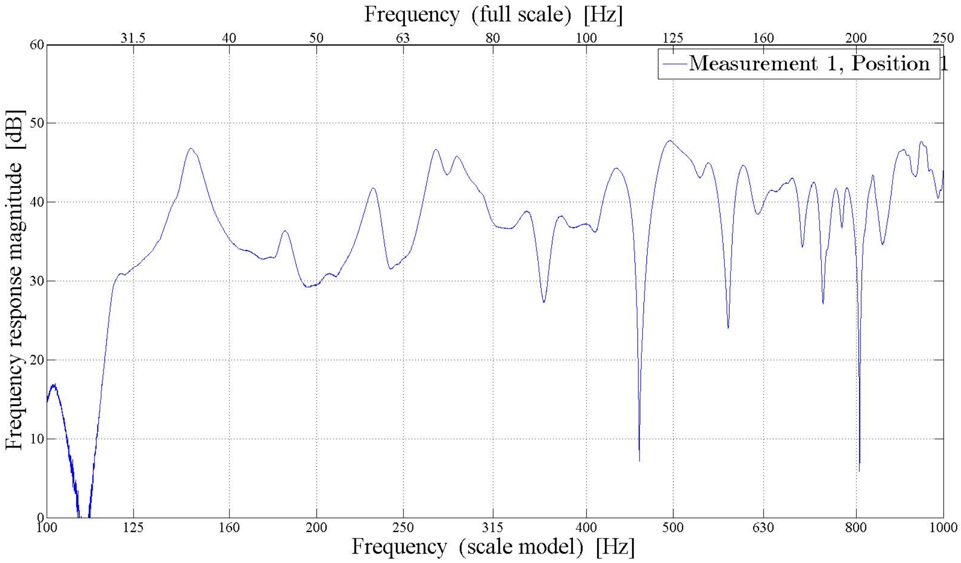

Figure 4.1: Transfer function $H_p(\omega)$, position 1, measurement series 1

The T_{30} and B values for measurement series 2 & 3 are included in Appendix A.3.

For each of the 12 transfer functions, 17 prominent mode peaks were selected and processed as described in Section 3.4.1. Further examples of the impulse response, noise floor transition and energy decay curve with fitted regression line determining T of the mode can be reviewed in Appendix A.4. The resulting 204 T-values are shown in Figure 4.3. Figure 4.3 is repeated in a larger version in Appendix A.5.

The first observation made from Figure 4.3 is that the estimated T values for grazing modes are marked blue and the estimated T values for non-grazing modes are marked red. Section 2.4.1 elaborates how the grazing incidence absorption derivation of Kinsler et al [8, p. 350] implies T of grazing modes to be twice that of T for non-grazing modes. Figure 4.3 shows $T_{grazing}$ to be indistinguishable from $T_{non-grazing}$.

The second observation to be made from Figure 4.3 is that the estimated values for T for the same mode is different in different measurements. The most obvious example is the [2 0 0]-mode at 145 Hz, which is included in 9 of the 12 transfer functions. The estimated reverberation time ranges from 0.26 s to 0.43 s, spanning a $\Delta T = 0.17$ s. However, as the frequency increases, the span in estimated T for a single modes narrows.

Furthermore, as the frequency and the mode density increases, the spacing be-

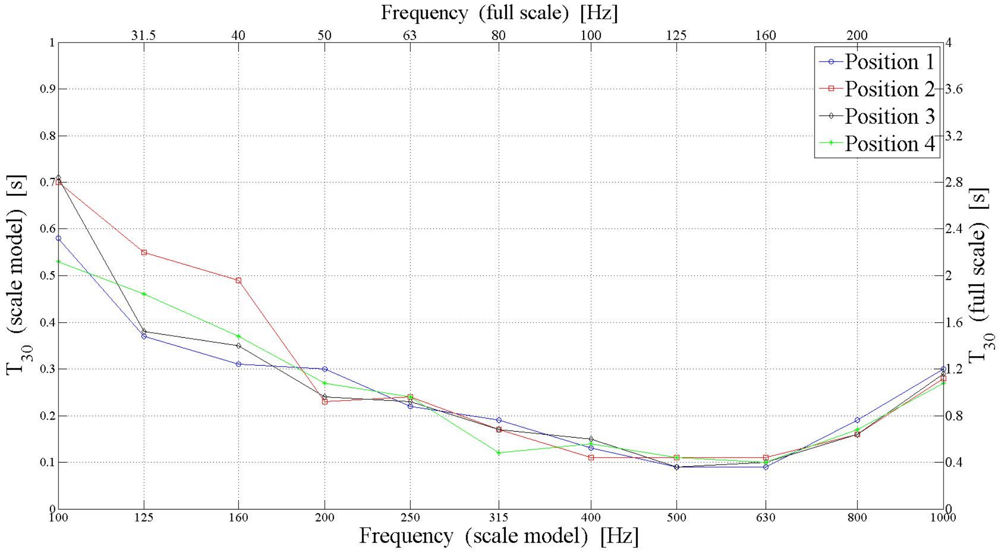

(a) WinMLS-calculated 1/3 octave band T_{30}

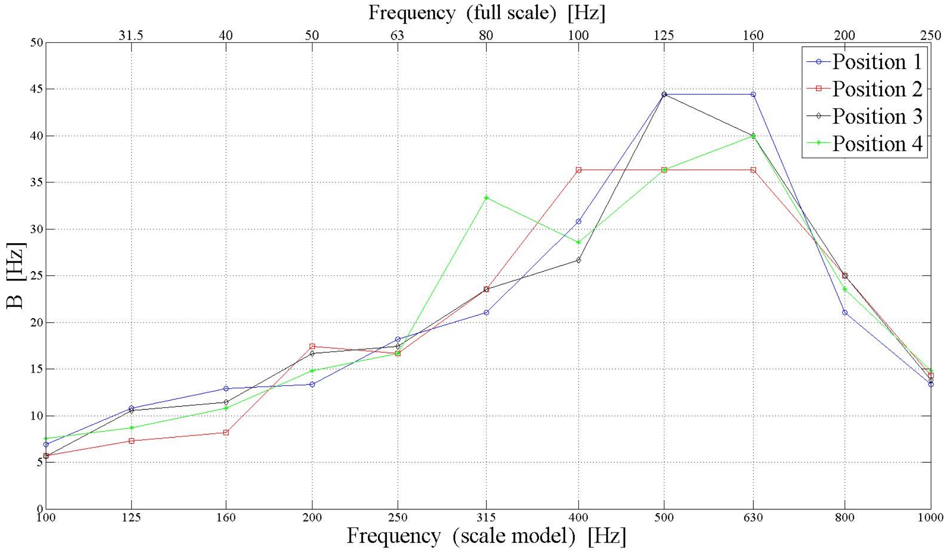

(b) Corresponding filterwidths B to WinMLS-calculated T_{30}

Figure 4.2: 1/3 octave band parameters directing the filterwidth

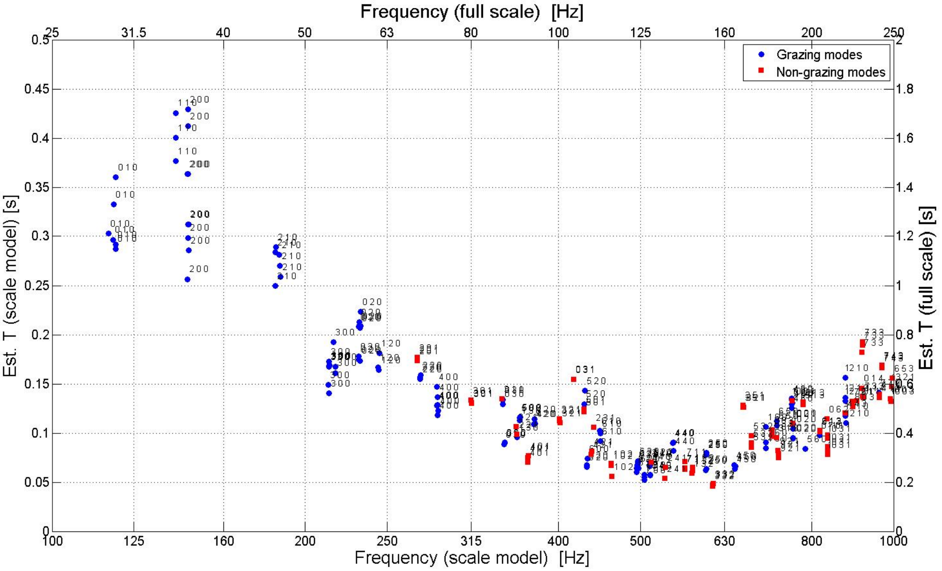

Figure 4.3: Estimated T for 204 mode peaks selected from 12 transfer functions H_p

tween modes decreases. This leads to fewer estimations of T for the same modes, which might also be part of the reason for why the span in estimated T over several measurements is narrowing.

4.1.2 Checking the influence of the filterwidth

The mode that was selected for checking the filterwidth was the [2 0 0]-mode at 145 Hz. This mode has very good mode separation, with the two adjacent modes [1 1 0] at 137 Hz and [2 1 0] at 186 Hz. Because this mode has $n_x =$ even, the measurement position 2 was not included. The transfer functions used was the H_p for measurement series 1, they are shown in Figure 4.4.

The resulting estimations of T for the 145 Hz mode are shown in Figure 4.5 for filterwidths ranging from 3 Hz to 38 Hz. As can be seen, the estimations are fairly constant for most wide filters, decreasing ever so slightly for filterwidths narrower than 20 Hz and down to ca 10 Hz. Filterwidths narrower than 9 Hz gives artificially high estimations of T. This is because the energy decay curve measured is distorted by the envelope Δt of the filter, as elaborated in Section 2.6.2.

The energy decay curves of the filtered transfer function for position 1 are shown together in Figure 4.6 for the filterwidths 3, 6, 9 and 11 Hz. The same four energy decay curves are included for all three positions in Appendix A.6. Figure 4.6 displays the marked change in energy decay slopes for the narrow filters.

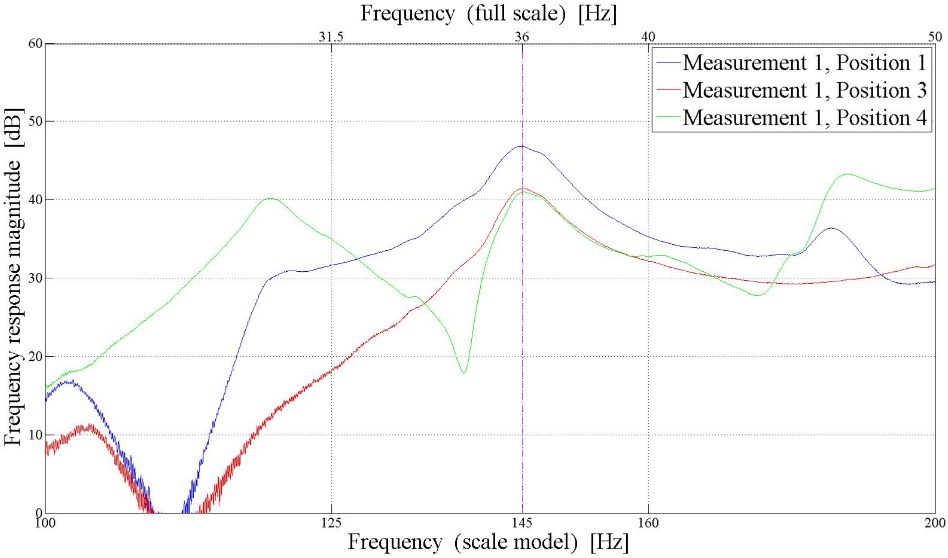

Figure 4.4: 145 Hz peak, measurement series 1, positions 1,3,4

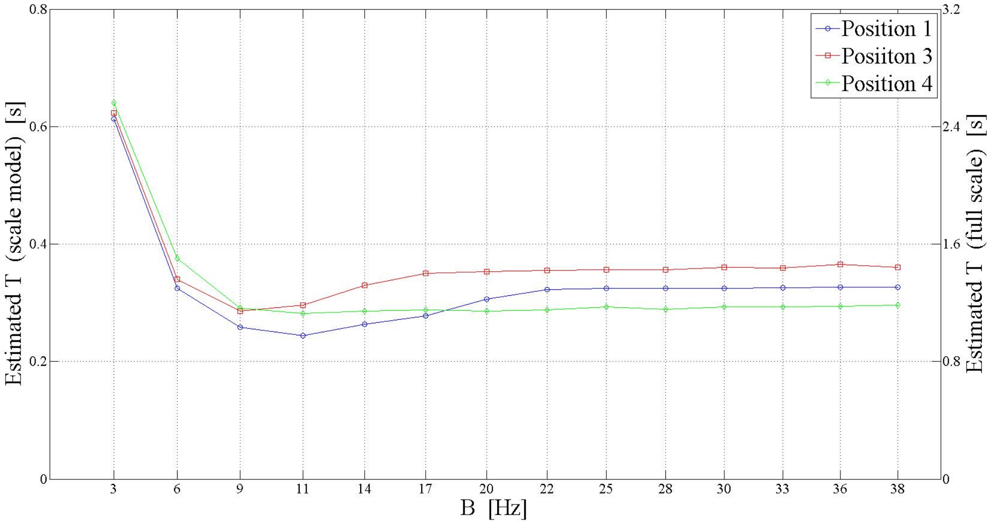

Figure 4.5: Estimated T of the 145 Hz peak, for different filterwidths

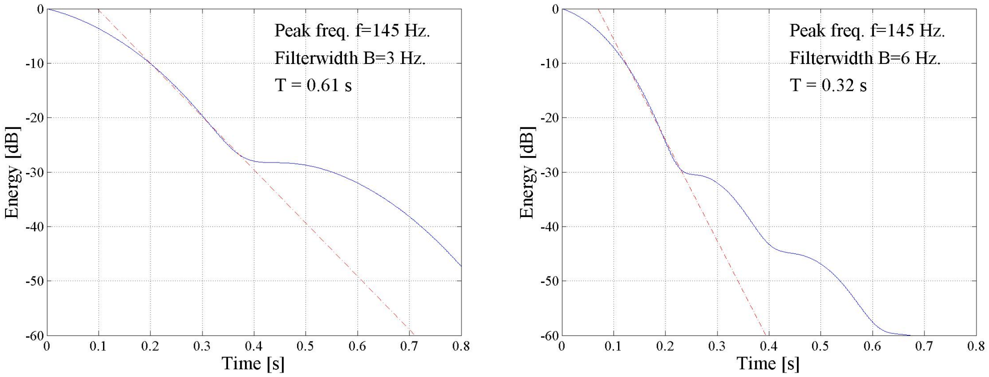

(a) Energy decay, $B = 3$ Hz

(b) Energy decay, $B = 6$ Hz

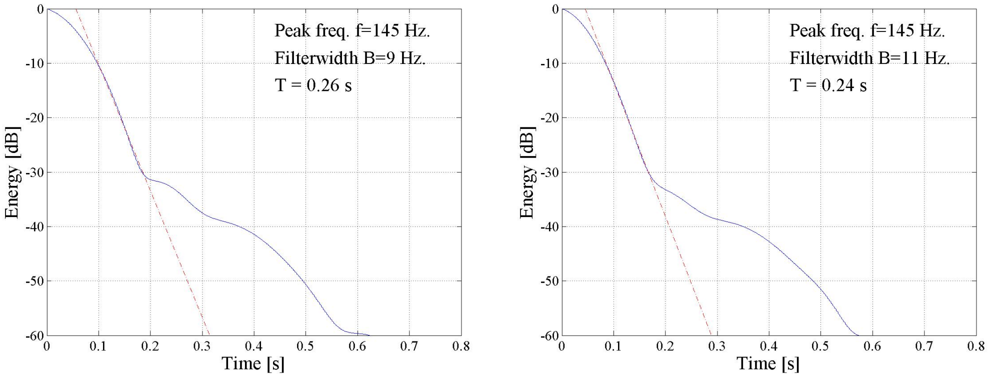

(c) Energy decay, $B = 9$ Hz

(d) Energy decay, $B = 11$ Hz

Figure 4.6: Energy decays for the four narrowest filters, position 1

4.2 Additional approaches

For the additional approaches, the method described in Section 3.4.2 was used.

4.2.1 T based on measurements of β

For calculating β, the transfer functions H_p and H_{u_z} for all four positions at d =1 cm below the ceiling were used with equation (2.42) to calculate the absorption coefficients. These are shown for position 1 in Figure 4.7, with the measured mode peak frequencies from Section 4.1 (for position 1) drawn as vertical lines.

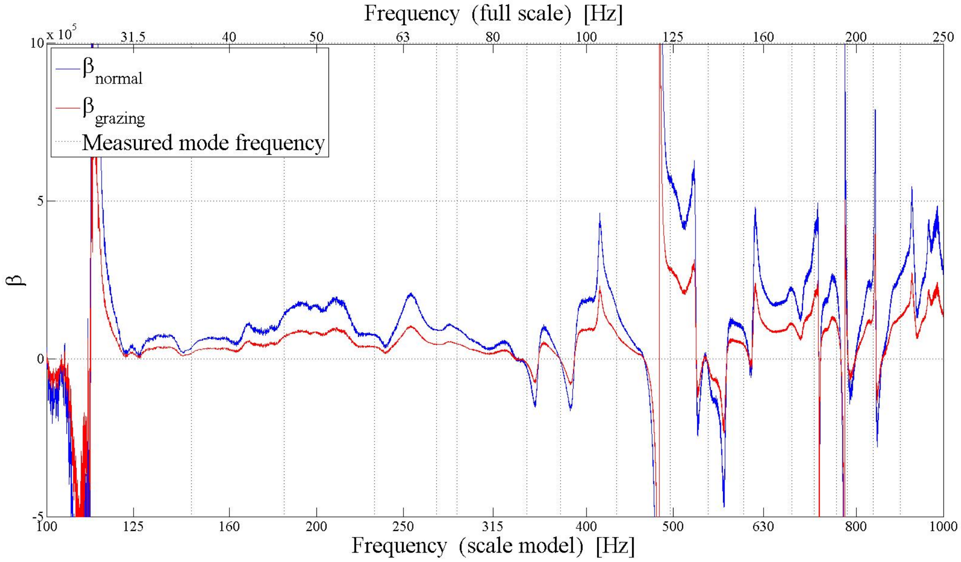

Figure 4.7: Calculated absorption coefficients β, position 1

Because the transfer functions used for calculating β are continuous, the resulting calculated β is too. However, the theory used in the calculations (Section 2.4) applies only to discreet modes. The values of the β curves from Figure 4.7 where they are intersected by the frequencies of the measured modes (the vertical lines) are replicated in Figure 4.8.

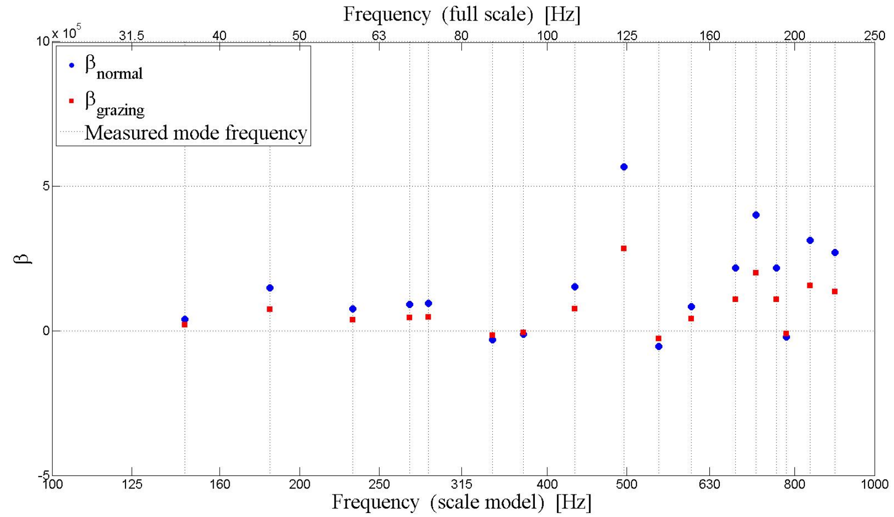

Figure 4.8: Calculated absorption coefficients β for position 1, shown only at measured (mode) frequencies

As described in Section 3.4.2, the absorption coefficient values are inserted into equation (2.46) to get the reverberation time estimates in Figure 4.9.

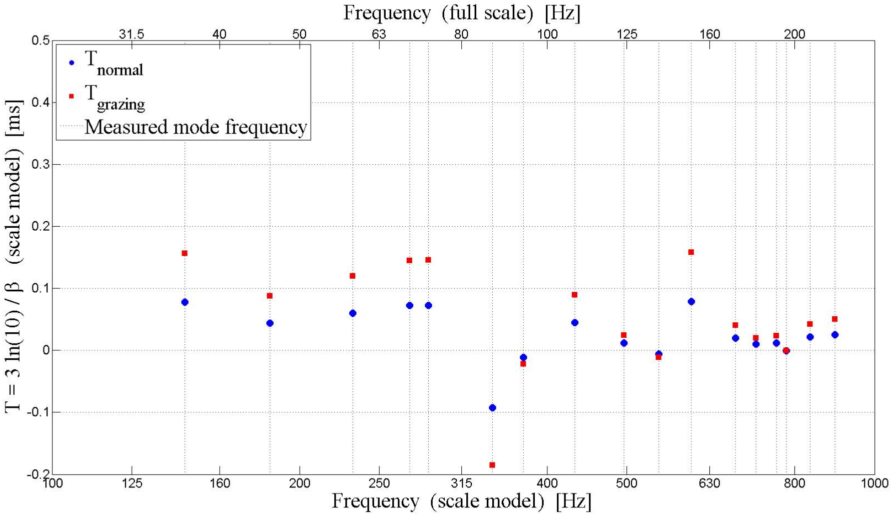

Figure 4.9: Values for T given by the calculated values for β in position 1

The absorption coefficients and corresponding reverberation time estimates for all four positions are included in Appendix B.1.

4.2.2 The intensity profile $I_z(d)$

The normalized z-component of the intensity $I_z(d)$ described in Section 3.4.2 is plotted for position 1 in Figure 4.10. The mode frequencies measured in position 1 are drawn as vertical lines.

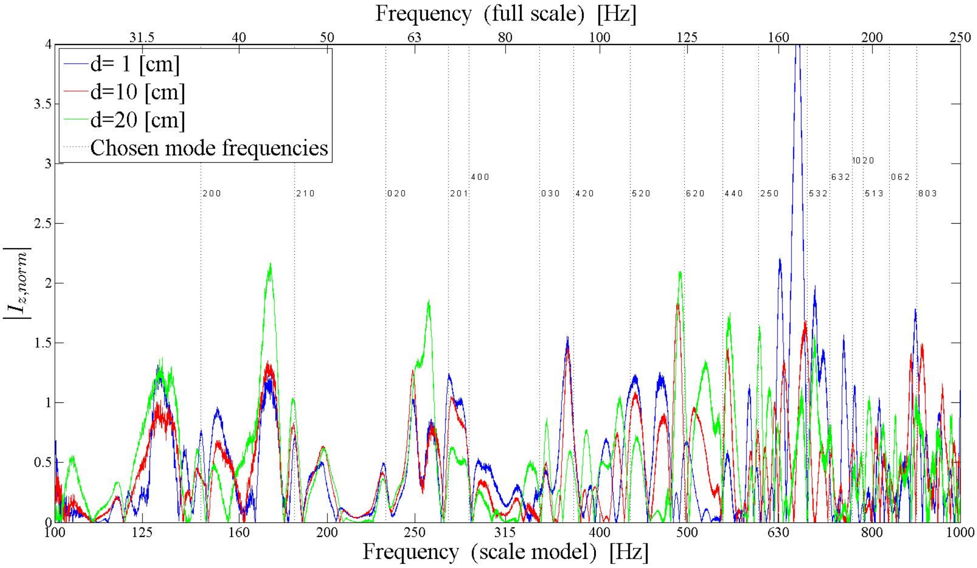

Figure 4.10: $I_z(d)$, position 1

As with the β measurements in the previous Section, the points of interest are the intersection frequencies of the measured modes. The frequency range from 125 - 500 Hz have therefore been sectioned into 6 separate figures zooming in on a minor part of the frequency range to better show the $I_z(d)$ values at the relevant frequencies. This can be seen in Figure 4.11. Figures 4.10 and 4.11 have been reiterated for positions 2,3 and 4 in Appendix B.2.

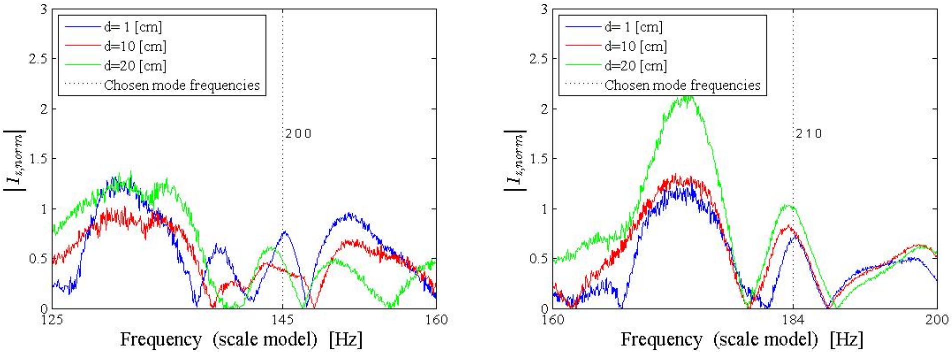

(a) $I_z(d)$, position 1, 1st mode

(b) $I_z(d)$, position 1, 2nd mode

Figure 4.11: $I_z(d)$, position 1, frequency scale zoom

What is obvious in all but the 3rd and 5th mode (Figures 4.11c and 4.11d) is that the z-component of the intensity varies for different distances d between the sound receiver and the absorber.

It's worth noting how 8 of the 9 modes (excepting the 4th mode at 272 Hz) have $n_z = 0$, meaning they are grazing modes. Examining only the grazing modes in Figure 4.11, and doing the same for Figures B.8, B.9 and B.10 in Appendix B.2 shows how roughly half of the grazing modes will have I_z varying significantly for different distances d. The other half of the grazing modes are varying to a lesser degree or very little.

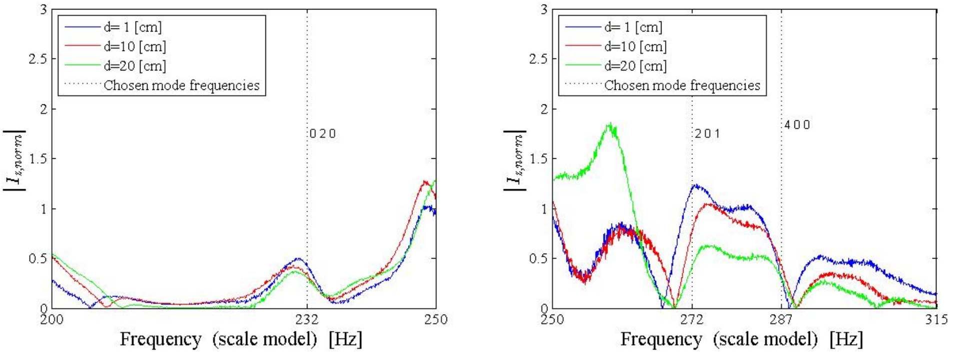

(c) $I_z(d)$, position 1, 3rd mode

(d) $I_z(d)$, position 1, 4th and 5th mode

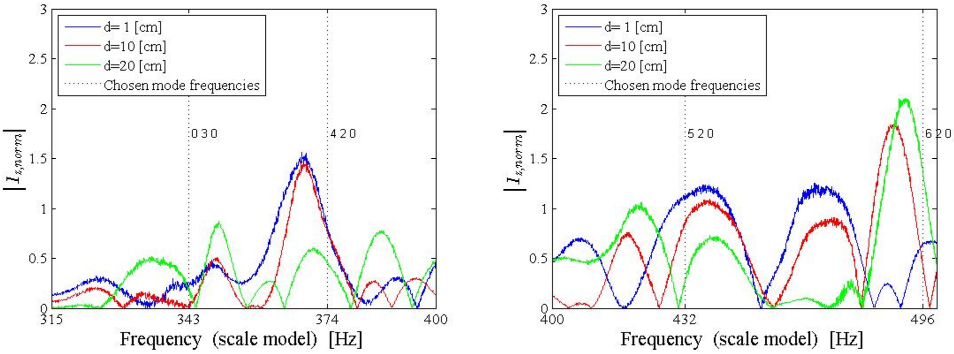

(e) $I_z(d)$, position 1, 6th and 7th mode

(f) $I_z(d)$, position 1, 8th and 9th mode

Figure 4.11: $I_z(d)$, position 1, frequency scale zoom

Chapter 5

Discussion

In this chapter, the measurement results are discussed. Some implications and possible explanations are developed. A number of possible, likely and actual sources of errors in the measurements and results are elaborated. Furthermore, the results and their possible implications are summed up and finally some suggestions for further work are included.

5.1 Primary approach

5.1.1 Estimation of modal T

The estimated modal T results presented in Section 4.1.1 contradicts existing theoretical predictions given by Kinsler et al [8]. As Kinsler et al. uses this grazing mode absorption theory with the Sabine expression for T (see equation (2.48)), the contradictory results will also be discussed using the Sabine expression.

The first point on which the results differ from the theory is the separability of the modes. Section 2.4.1 describes how the reverberation time $T_{grazing}$ of grazing modes should be twice that of non-graing modes $T_{non-grazing}$. The results show how $T_{grazing}$ is statistically indistinguishable from $T_{non-grazing}$.

Calculating the average $T_{grazing}$ and $T_{non-grazing}$ for the 500 Hz 1/3 octave band as a representative example gives the estimated reverberation time as

$$\begin{aligned} T_{500,grazing} &= 0.0742 \pm 0.0064 \text{ s} \\ T_{500,non-grazing} &= 0.0687 \pm 0.0127 \text{ s} \end{aligned}$$

with a 95 % confidence interval given by the student t-distribution [11, p. 1052].

This result relies on the estimation of T being good enough. With good mode separation, suitably narrow filters and good signal-to-noise ratios for most modes (see Appendix A.4) the estimation method appears to be good.

The second point on which the results differ from the theory is the values of the reverberation time. Assuming perfectly hard walls and floors and a 100 % effective absorber ceiling gives the lowest possible T_{Sabine} by equation (2.48) as:

$$\begin{aligned} T_{random} &= \frac{0.161 \cdot L_x L_y L_z}{L_x L_y \cdot 1} = 0.161 \cdot 0.75 = 0.12 \text{ s} \\ T_{grazing} &= 2 \cdot T_{random} = 0.24 \text{ s} . \end{aligned}$$

The results on the other hand, gives T in the 500 Hz and 630 Hz 1/3 octave bands as

$$\begin{aligned} T_{500} &= 0.0730 \pm 0.0054 \text{ s} \\ T_{630} &= 0.0787 \pm 0.0080 \text{ s} \end{aligned}$$

with a 95 % confidence interval given by the student t-distribution. In other words, the measured T is significantly lower than the *minimum* predicted T_{Sabine}.

As noted in Section 2.5, the Sabine expression will give $T > 0$ for $\overline{\alpha} = 1$, but as Kinsler et al. refers to the Sabine expression for T in relation to the grazing incidence absorption it is appropriate to also relate the results to T_{Sabine}.

It's worth noting that the setup used for calculating $T_{Sabine} = 0.12$ s mentioned above will give the following values for T_{Eyring}, using equation (2.50):

$$\begin{aligned} \overline{\alpha}_{Eyring} &= \frac{S_{ceiling}\,\alpha_{ceiling}}{S_{total}} \\ T_{random} &= \frac{0.161V}{-S_{total}\,\ln\left(1 - \overline{\alpha}_{Eyring}\right)} = 0.104s \\ T_{grazing} &= 2 \cdot T_{random} = 0.207 \text{ s} . \end{aligned}$$

5.1.2 The influence of the filterwidth

Figure 4.5 shows how too narrow filters will give false high estimations of T. As the filterwidths narrows to 9 Hz, estimations of T starts to rise. For narrower filterwidths than 9 Hz, the (false) high estimations T increase fast. Keeping in mind that the 145 Hz mode is in the 160 Hz 1/3 octave band and examining the calculated filterwidth B based on the WinMLS-calculated 1/3 octave band T_{30} values (displayed in Figure 4.2b, the minimum filterwidth B for the 160 Hz band is given as approximately 8-13 Hz (depending on measurement position).

This indicates that the filterwidth lower limit presented in equation (2.55) is an effective boundary to achieve as narrow filters as possible without getting false high estimations of T.

5.2 Additional approaches

5.2.1 T based on measurements of β

The β values presented in Figure 4.8 are very high, and consequently they result in very low values for T, as seen in Figure 4.9. Ranging from approximately $0.1 \cdot 10^5 \leqslant \beta \leqslant 5{\cdot}10^5$, the absorption values give reverberation times in the $0.01{\cdot}10^{-3} \leqslant T \leqslant 0.5{\cdot}10^{-3}$ s range.

Reverberation times in the milliseconds is obviously not the case for most any room. Taking a second look at the assumptions made to develop the grazing mode absorption theory in section 2.4, one of the assumptions that make up the basis for the expressions stands out:

> Neglecting the reactive part of the normal specific acoustic impedance leads to the following expression:
>
> $$\boldsymbol{z}_x = \rho_0 c v_x$$
>
> where v_x is the dimensionless relationship $\boldsymbol{z}_x^{wall}/Z^{air}$.

Running a WinFlag simulation as described in Section 3.4.3, it becomes obvious that the reactive (imaginary) part of the impedance is far from zero. This is shown in Figure 5.1. Because $\Im\{\boldsymbol{z}_x\} \neq 0$ it is reasonable to question the validity of this assumption.

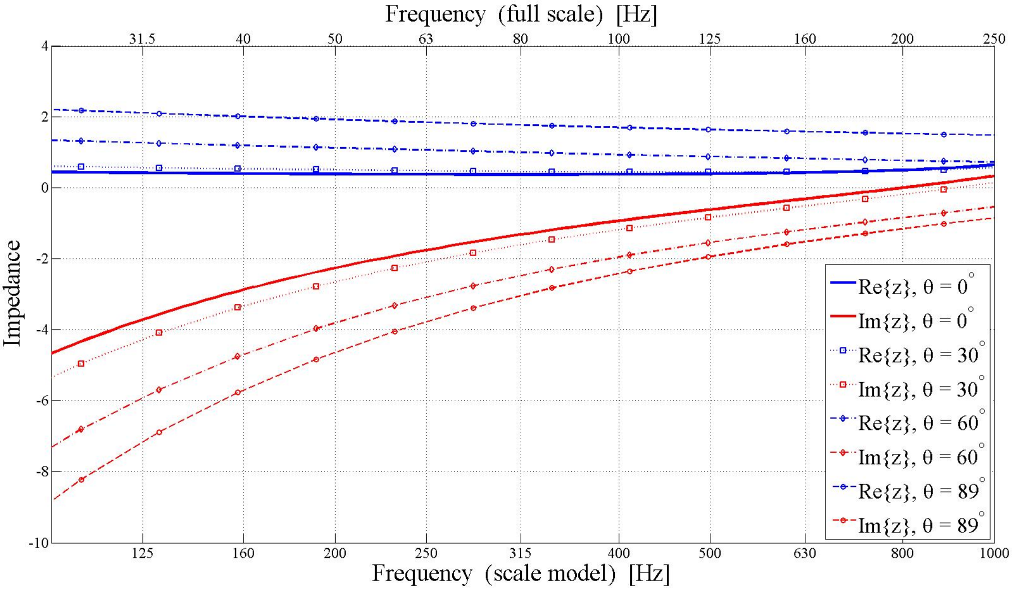

Figure 5.1: Simulated absorber impedance using WinFlag & the Delany-Bazley model (Komatsu version)

To illustrate how the derivation of β could look differently if v_x were complex (and thereby making $\boldsymbol{z}_x$ complex), v_x can be substituted by

$$\boldsymbol{v}_x = R_v + jI_v \ , \tag{5.1}$$

which can be inserted into equation (2.36):

$$\begin{aligned} (k_x L_x - n_x \pi) + j\alpha_x L_x &= j\frac{1}{R_v + jI_v}\frac{(\omega_D + j\beta_x)/c}{k_x + j\alpha_x} \\ n_x &= 0, 1, 2\ldots . \end{aligned} \tag{5.2}$$

Solving equation (5.2) first for $n_x = 0$ gives the imaginary part of the equation as

$$k_x \alpha_x \left[2R_v L_x + I_v L_x \left(\frac{k_x}{\alpha_x} - \frac{\alpha_x}{k_x} \right) \right] = \frac{\omega_D}{c} \ , \tag{5.3}$$

and combined with equation (2.34) this gives

$$\beta_{grazing} = \frac{c}{2R_v L_x + I_v L_x \left(\dfrac{k_x}{\alpha_x} - \dfrac{\alpha_x}{k_x} \right)} \ . \tag{5.4}$$

Solving equation (5.2) next for $n_x \neq 0$ and assuming (like in Section 2.4) $k_x L_x \approx n_x \pi$, the imaginary part of the equation can be expressed as

$$k_x \alpha_x \left(R_v L_x - I_x L_x \frac{\alpha_x}{k_x} \right) = \frac{\omega_D}{c} \ , \tag{5.5}$$

and combined with equation (2.34) this gives

$$\beta_{non-grazing} = \frac{c}{R_v L_x - I_v L_x \dfrac{\alpha_x}{k_x}} \ . \tag{5.6}$$

These expressions for $\beta_{grazing}$ and $\beta_{non-grazing}$ are somewhat more different from each other than than the ones in Section 2.4. Further analysis could be done by letting the WinFlag simulation provide R_v and I_v from the simulation. The ratio of α_x to k_x defines these expressions to some degree, and could also be examined further.

Examining the line of reasoning in Section 2.4 further, the next approximation is that $k_x L_x \approx n_x \pi$ for the expression in equation (2.35). Testing this approximation is a simple matter: Setting up the parameters

$$\begin{aligned} n_x &= 1 \\ L_x &= 1 \\ k_x &= \frac{n_x \pi}{0.99 L_x} \ , \end{aligned}$$

it is now possible to substitute them into the left hand side of equations (2.35) and (2.36). The calculation of these expressions for different values of α_x are shown in Figure 5.2. They show this approximation to be adequate for values of α_x up to ca 0.4.

5.2.2 The intensity profile $I_z(d)$

As described in Chapter 2, modes with grazing incidence on a surface in the x, y-plane will not have any sound waves propagating along the z-axis. Theoretically, these modes will have $u_z = 0$ and consequently the vertical intensity component $I_z = 0$. However,

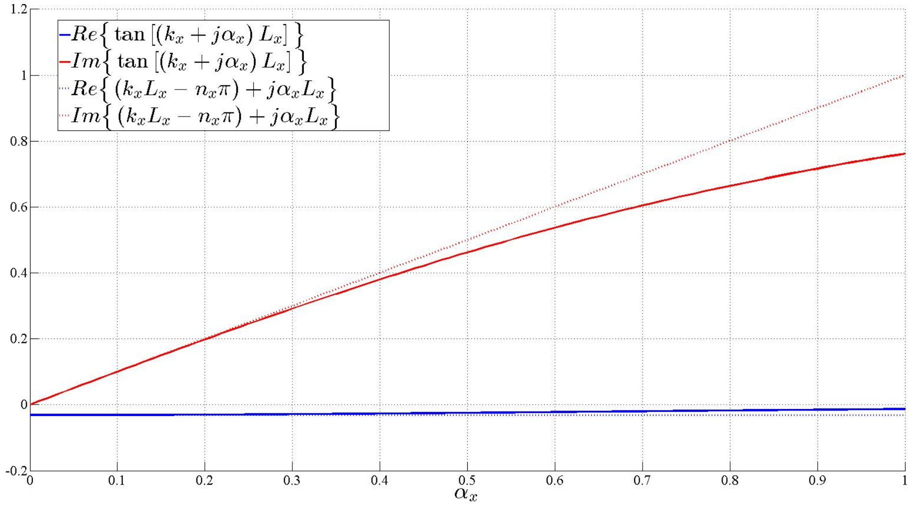

Figure 5.2: Calculated disparity between equations (2.35) and (2.36) for different values of α_x

when the boundary condition in the z-dimension is an impedance $\boldsymbol{z} \neq \infty$, the mode *must* have an intensity component $I_z \neq 0$. Experimentally, I_z should then not be significantly different from background noise. As described in Section 4.2.2, it's not possible to distinguish grazing modes from non-grazing modes in the measurements based on this criteria.

As the observed 'grazing' modes are indeed damped more than can be attributed to the walls, the sound energy is presumably dissipating through the absorber, as specified by the boundary condition. This means vertical energy transference is occurring and consequently that the mode has a vertical intensity component. This is particularly well illustrated in Figure B.8c, where the 'grazing' mode [3 0 0] obviously has a vertical intensity component that is not zero.

This suggests that there might not be any *true* grazing modes present in the measurements. One possible explanation is that there are no true grazing modes present in enclosed spaces, at least not parallel to any sound absorbing surface.

It should be noted in this context that the theoretical expressions for grazing incidence absorption presented by Kinsler et al. (Section 2.4) is not based on this line of reasoning. Observe how the hard wall differs from the absorber surface:

1. The surface is a hard wall. $u_z = 0$ at the wall $\Rightarrow \boldsymbol{z}_z = \infty$ and $I_z = 0$.

2. The surface is an absorber. $u_z \neq 0$ at the wall $\Rightarrow$ $\boldsymbol{z}_z \neq \infty$ and $I_z \neq 0$.

Operating with the term *damped modes* assumes that the specific acoustic impedance in the air next to the absorber surface

$$\boldsymbol{z}_{air} = \frac{p_{air}}{u_{air}} \approx \boldsymbol{z}_{absorber} \neq \infty \tag{5.7}$$

at the absorber surface.

Still, the expressions presented in Section 2.4 are nonetheless contradicted by the experimental results.

Taking a closer look at a plane wave propagating parallel to a surface, the hard wall scenario in Figure 5.3a gives a true plane wave and true grazing incidence. The absorber scenario in Figure 5.3b gives a quasi-plane wave that is interacting with the surface. But it still retains most plane wave characteristics.

Comparing Figures 5.3a and 5.3b, it can be noted how

$$\begin{aligned} p = p(x,t) \quad &\Rightarrow \quad u_z = \frac{\partial p}{\partial z} = 0 \\ p = p(x,z,t) \quad &\Rightarrow \quad u_z = \frac{\partial p}{\partial z} \neq 0 \; . \end{aligned}$$

The expressions for $p(z)$ are not trivial and beyond the scope of this thesis.

The relevance of the absorber surface in Figure 5.3b is made by the geometry. When the plane wave is propagating parallel to a soft surface, its behaviour can be described as if there was a boundary layer along the surface:

If there are no restrictions in the z-dimension ($L_z \rightarrow \infty$), the thickness of the boundary layer is negligible ($L_{BL} << L_z$) and the wave is not attenuated by the surface. However if there is a limitation in the z-dimension ($L_z \nrightarrow \infty$), then L_{BL} is not negligible compared to L_z and the wave will interact with the boundary layer. In the boundary layer, the wave will have a z-component: $p(x,t)_{BL} = p(x,z,t)$.

This might serve to explain how the grazing modes cease being 'true' grazing modes when propagating parallel to a surface that is not infinitely hard, and this may be somewhat easier to observe in the HARD CASE geometry than for other types of rooms.

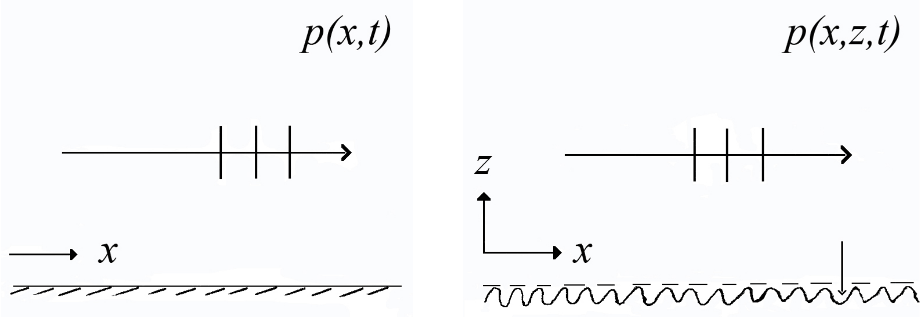

(a) Plane wave propagating parallel to a hard wall

(b) Quasi-plane wave propagating parallel to a soft wall

Figure 5.3: Plane wave propagating parallel to a hard & a soft surface

5.3 Sources of error

Concerning weaknesses in the results, the most obvious one is that the same mode will have different estimations of T from different measurements. However, this is most pronounced for the lowest frequency modes and as the frequency increases, the span in estimated T values for a single modes narrows. This is in accordance with the theory from Section 2.1.3, stating that higher frequencies have higher mode density, more even sound pressure distribution throughout the room and less uncertainty in the estimation of T.

Earlier measurements in the scale model box by the author [5, p. 20] confirm widening confidence interval for decreasing frequencies, and a figure of these measurements is included here for illustrative purposes: Figure 5.4 also includes a 95 % confidence interval using the student t-distribution.

Another problem with the results is that as the mode separation spacing decreases (for increasing frequencies), the identification of mode peaks becomes increasingly uncertain. This is because even though the theoretical modes given by equation (2.7) are fairly accurate, they are not perfectly spot-on. As shown in Figure 5.5, the modes of the measured transfer function are not perfectly aligned with the relevant theoretical mode frequencies.

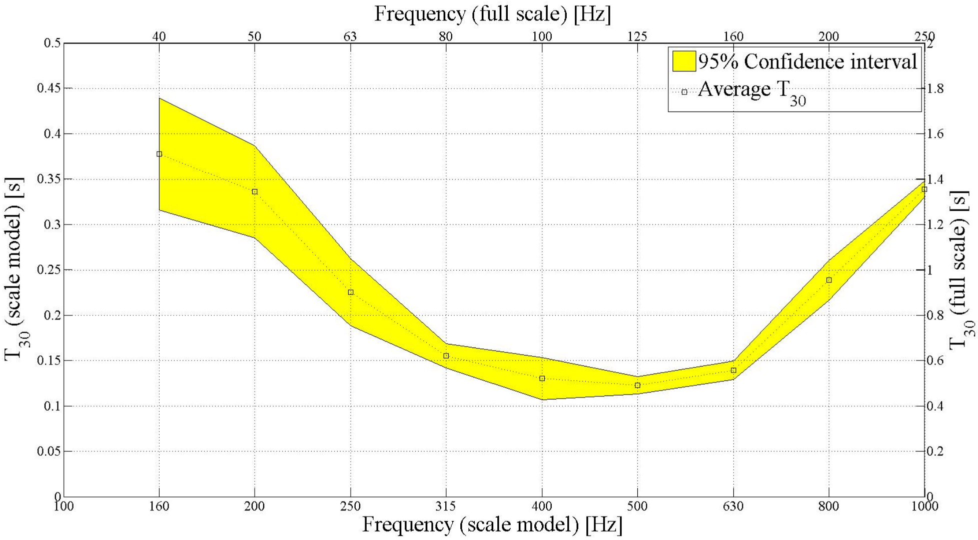

Figure 5.4: Previous T_{30} measurements of the scale model box in 1/3 octave bands

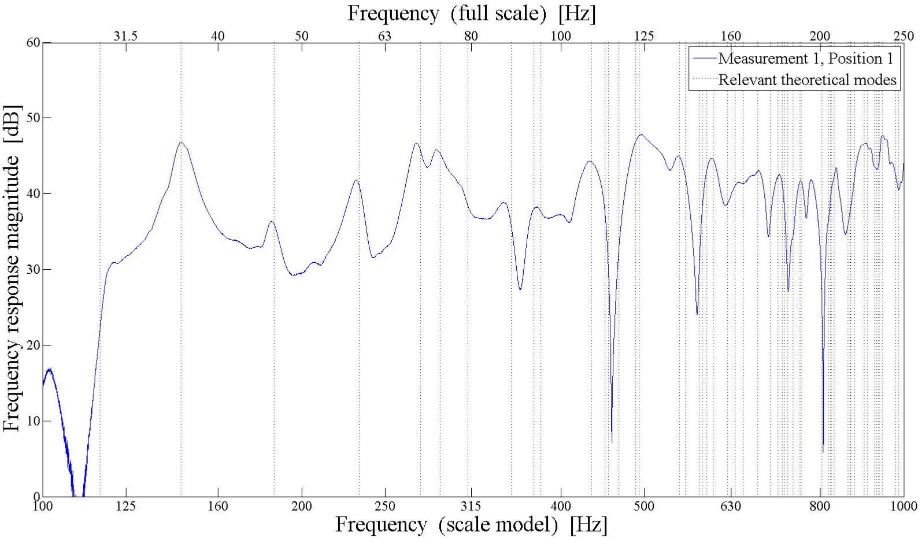

Figure 5.5: Transfer function $H_{p,1}(\omega)$ (position 1, measurement series 1) with relevant theoretical mode frequencies as vertical lines

Note how the relevant theoretical mode frequencies plotted as vertical lines are the mode frequencies that are not suppressed by the sound source and receiver placement. Figure 5.5 shows a transfer function for position 1, in which the modes with $n_x = 1, 3, 5...$ will be suppressed. Accordingly, these mode frequencies are not plotted. The 3 remaining transfer functions for positions 2,3,4 from measurement series 1 are presented with relevant theoretical modes in Appendix C.

The mode separation might have been improved by using the $u(t)$ impulse responses instead of the $p(t)$ impulse response. However, as elaborated in Section 3.4.1, this would have been at the expense of significantly poorer signal-to-noise ratios.

The attempt at normalizing the vertical component of sound intensity I_z described in Section 3.4.2 has an obvious weakness in that the mean transfer function used as basis for the normalization is not statistically representative for the room – using only the 4 measurement positions that were used for the measurements. Improvement of the normalized I_z could be achieved by measuring more transfer functions at different points in the room.

The measurement equipment will probably affect the measurements. One example is the loudspeaker, as its size makes it into a sound diffuser. The diffusing element is probably not negligible on account of the size of the loudspeaker not being negligible, compared to the size of the room. Scattering effects of sound waves on objects will be present for $ka > 1$ where k is the wave number and a is the dimension of the object. Using the loudspeaker length of 40 cm gives scattering effects above approximately 140 Hz.

Another systematic error source is the scale model. Shortcomings in the model construction can lead to inaccuracies – as with the walls that are not stiff enough, leading to incorrect frequency placement for the measured [1 0 0] mode (compared to the theoretical mode frequency), as well as probably giving some margin of error for the reverberation times at low frequencies.

When measuring impulse responses, a sufficiently high signal-to-noise ratio is needed. Most measurements have been checked for sufficient SNR in low frequency 1/3 octave bands, as the low frequency bands usually have the worst SNR due to the roll-off of the sound source and receiver.

It is possible that some measurements might have been recorded while disturbed by outside noises from the the rest of the building. WinMLS have shown itself to be somewhat unstable, giving completely wrong results from time to time. Erroneous results from these erratic sources have been removed whenever they have been discovered.

Room temperature was recorded to vary between 18.4°C and 20.2°C. Relative humidity in the air were recorded to vary from 25 - 33 %. These fluctuations are not accounted for in the measurements, as their impact on the results are deemed negligible.

5.4 Concluding remarks

This thesis appertain to small shoebox-shaped rooms with hard, flat walls and an absorbing ceiling, dubbed THE HARD CASE. This room shape leads to some frequency dependent absorption characteristics that are in opposition to predictions by existing theory.

The hypothesis used as a starting point is that the existing expressions for grazing mode absorption and non-grazing mode absorption can be tested and rejected. Specifically, the expression under scrutiny states that grazing modes will be absorbed by a factor 1/2 the absorption on non-grazing modes, and consequently that grazing modes will have twice the reverberation time of non-grazing modes.

The aim of this thesis was to provide measurements that would try to validate or possibly reject this relation.

The primary approach to this was an attempt at estimating the reverberation time of single modes *and* identifying the modes as either grazing or non-grazing modes. The reverberation time of grazing modes and non-grazing modes could then be compared. This was achieved, even if the identification of modes might be drawn into doubt – particularly for increasing frequencies and mode density.

However, the 204 mode peaks analysed were not statistically separable into two distinct clouds of data-points. In other words, it was not possible to separate one group of modes from another based on reverberation time estimates. This is a very good indication that the hypothesis is good.

There were two additional approaches complementing the primary approach. The first was to calculate the absorption coefficients β from measurements of $\boldsymbol{p}$ and $\boldsymbol{u}_z$, and then the reverberation times T from β. These values for T proved to be several orders of magnitude smaller than what was observed – Giving reverberation times in milliseconds. This is also a good indication that the hypothesis is good.

The second part of the complementary approaches was to measure the vertical component of the sound intensity I_z as a function of distance d from the absorber ceiling. The motivation for doing this was not directly linked to the main aim of the thesis – testing the absorption of grazing modes. Rather, this part of experiment was an effort into understanding the workings of the absorber.

These measurements showed that it was not possible to separate the grazing modes from the non-grazing modes based on any assumption that the grazing modes should behave differently than the non-grazing modes with respect to the vertical intensity component.

This might indicate that any 2D sound field propagating more or less parallel to the ceiling might not have all the characteristics attributed to 'true' (theoretical) grazing modes. However, it might also just as well be explained by the fact that the space is damped by the absorber ceiling.

Furthermore, the values of the estimated T for the modes between approximately 450 Hz and 700 Hz were significantly lower than the minimum possible T predicted by conventional theory. That is, both the Sabine and Eyring expressions for minimum T overshot the estimated modal T from the measurements. This is another very good indicator that existing theory can be rejected.

Examining the derivation of β and the assumptions made, one weakness stands out: Kinsler et al. [8] assumes the specific acoustic impedance of the absorber surface approximately equal to the resistive part of the impedance – neglecting the reactive part. Closer examination of the impedance reveals this to be a rather poor approximation.

5.5 Suggestions for further work

To achieve better understanding of what is actually happening in and to develop a solid theoretical foundation for accurately predicting the acoustics of THE HARD CASE, some topics for further work are suggested:

As this thesis finds no fault in the mathematical derivations of the expressions for grazing incidence absorption, further analysis of the assumptions that make up the basis for the derivations are in order.

One assumption that has not been discussed is that the material is locally reacting. All theoretical models and expressions used in this thesis assumes the absorber material to be locally reacting. That is to say: the sound wave incident on an absorber surface can be decomposed into two waves inside the material – one parallel to the absorber surface and one perpendicular to it. The common assumption in most room acoustics is that the attenuation of the wave propagating parallel to the surface is so much larger than for the wave propagating perpendicular to the surface, that the parallel wave is neglected. A common exception is sound propagation in ducts – where the porous absorber can be assumed globally reacting, but whether duct theory is applicable to THE HARD CASE has not been determined. Local reaction absorption is relevant mainly in relation to the discussion about true grazing modes in enclosed spaces and plane waves propagating parallel to soft walls (see Section 5.2.2).

Another assumption made in the derivation is that $k_x L_x = n_x \pi$, which enables equation (2.39) to be simplified in order to provide the expression (2.40). For $n_x = 1$ this gives $k_x L_x = \pi$, which is what would be expected in a hard wall scenario.

However, with an efficient absorber the validity of the hard wall assumption is not obvious. Further investigations into which modes n_x the assumption is adequate for, and the magnitude of any margin of error such an assumption might entail, is warranted.

The assumption that the specific acoustic impedance of the absorber surface is approximately equal to the resistive part of the impedance has been explored in Section 5.2.1 and a (somewhat quick-fix) alternative (including a complex ratio of impedances $\boldsymbol{z}_x^{wall}/\boldsymbol{Z}^{air} = \boldsymbol{v}_x = R_v + jI_v$) has been sketched. The resulting expressions (5.4) and (5.6) should be tested.

The difference in absorption characteristics of THE HARD CASE between low and high frequencies (which cannot be explained by existing theory) elicits a closer look at the cross-over region. For the scale model, this is the frequency range of approximately 600-1000 Hz (see Figure 1.1). Why is the ratio between theoretical diffuse field absorption and HARD CASE (scale model) absorption almost ~ 2 at low frequencies while down to $\sim 1/9$ for high frequencies? The impedance simulations in Figure 5.1 show $\left|\Im\{\boldsymbol{z}\}\right|$ is only dramatically increasing for frequencies below ~ 250 Hz, which means there are no obvious explanations for the change in absorption characteristics at the cross-over region.

A basic property of THE HARD CASE is that vertical components of the reverberant sound field is attenuated faster than the horizontal components. Theory and experiments indicate this behaviour in the high-frequency region, but it is not observed in the low-frequency region. Contrary to what is expected, experiments show examples of grazing modes (at least grazing according to theory) with equally strong vertical components as the non-grazing modes. It could be speculated how a good porous absorber affects the low-frequency grazing modes to such an extent that they cease being grazing modes. With no true horizontal modes, the 'basic property of THE HARD CASE' (with vertical components of the reverberant field quickly damped and horizontal components damped much slower) is not present in the low-frequency region.

If this is the case, one important practical implication would be that a sound absorbing ceiling can be more than twice as efficient as the same amount of sound absorbers evenly divided between surfaces in all three dimensions x, y, z. This will require further investigations.

Chapter 6

Conclusions

Kinsler et al.'s [8] theory on damped modes does not seem to be applicable to the shoebox-shaped room with five hard walls and one absorber wall (denoted THE HARD CASE in this thesis):

- No factor 2 reverberation time has been observed between one group of modes and another.
- The assumption Kinsler et al. makes on wall impedance – which is the basis for the damped mode analysis – does not fit with porous absorbers on rigid walls.

Furthermore:

- The characteristics of 'true' grazing waves could not be applied to any sound waves in these measurements. The existence of 'true' grazing waves in the HARD CASE scenario are drawn into doubt, and by extension is drawn into doubt for all non-perfectly hard surfaces.
- For measurements in the HARD CASE scenario, it has been possible to analyse the reverberation times of up to 17 modes in each measurement position, indirectly.
- The use of a Microflown USP Regular sound probe could have given sparser mode peaks in the impulse responses (by using the particle velocity component sensors), and thereby facilitate the analysis of more modes. However, using the pressure sensor gives a superior SNR.

Bibliography

[1] L. L. Beranek. Analysis of Sabine and Eyring equations and their application to concert hall audience and chair absorption. *The Journal of the Acoustical Society of America*, 120(3):1399–1410, 2006.

[2] M. M. Boone, G. Janssen, and M. van Overbeek. Modal superposition in the time domain: Theory and experimental results. *The Journal of the Acoustical Society of America*, 97(1):92–97, 1995.

[3] A. Farina. Advancements in impulse response measurements by sine sweeps. In *Audio Engineering Society Convention 122*. Audio Engineering Society, 2007.

[4] B. Girod, R. Rabenstein, and A. Stenger. *Signals and* S*ystems*. John Wiley & Sons Inc, 2001.

[5] H. Granseth. Scale model measurements for ceiling absorbers. *Unpublished Project*, NTNU, 2015.

[6] E. ISO. 3382-2: 2008. *Acoustics.* M*easurements of room acoustics parameters.* P*art*, 2:3382–2.

[7] F. Jacobsen and J. Rindel. Time reversed decay measurements. *Journal of Sound and vibration*, 117(1):187–190, 1987.

[8] L. E. Kinsler, A. R. Frey, A. B. Coppens, and J. V. Sanders. *Fundamentals of* A*coustics*. John Wiley & Sons, 1999. 4th Edition.

[9] B. Kolbrek. Interviews, 2014. NTNU.

[10] T. Komatsu. Improvement of the Delany-Bazley and Miki models for fibrous sound-absorbing materials. *Acoustical science and technology*, 29(2):121–129, 2008.

[11] E. Kreyszig. *Advanced* E*ngineering* M*athematics*. John Wiley & Sons, 1988. 9th Edition.

[12] P. M. Morse. Some Aspects of the Theory of Room Acoustics. *The Journal of the Acoustical Society of America*, 11(1):56–66, 1939.

[13] M. R. Schroeder and K. Kuttruff. On Frequency Response Curves in Rooms. Comparison of Experimental, Theoretical, and Monte Carlo Results for the Average Frequency Spacing between Maxima. *The Journal of the Acoustical Society of America*, 34(1):76–80, 1962.

[14] M. Skålevik. Schroeder Frequency Revisited. In *Forum Acusticum*, volume 2, page 2, 2011.

[15] M. Skålevik. Small room acoustics – the hard case. In *Proceedings of Forum Acusticum*, 2011.

[16] StandardNorge. NS 8175:2012 – Lydforhold i bygninger, Lydklassifisering for ulike bygningstyper (Acoustic conditions in buildings, Sound classification of various types of buildings), 2012.

[17] S.-I. Thomasson. *Theory and experiments on the sound absorption as function of the area*. Department of Acoustics, Royal Institute of Technology, 1982.

[18] J. Vennerød. The Hard Case – Improving Room Acoustic in Cuboid Rooms by using Diffusors. *Unpublished Project*, NTNU, 2013.

[19] T. E. Vigran. *Building* A*coustics*. Taylor & Francis, 2008.

[20] T. E. Vigran. MANUAL FOR WINFLAG, VERSION 3.0. 2014.

[21] H. D. Young, R. A. Freedman, and L. Ford. SEARS AND ZEMANSKY'S UNIVERSITY PHYSICS. Pearson Education, Inc., 2008. 12th Edition.

Appendices

Appendix A

Primary Approach

Appendix A contains the intermediate measurement results and post-processing results from the *Primary approach* section of the results presented in Chapter 4.

A.1 Signal-to-noise ratios

Section A.1 presents the SNR values for all four channels of the Microflown probe from all four measurement positions.

f [Hz]	SNR (p)	SNR (u_x)	SNR (u_y)	SNR (u_z)
100	23.3	12.4	26.1	4.8
125	45.4	19.6	30.0	20.7
160	50.6	24.8	34.9	25.8
200	45.5	27.0	37.8	32.0
250	54.5	31.0	40.5	33.2
315	55.4	26.0	35.7	27.2
400	54.7	21.7	36.9	31.2
500	59.1	20.7	37.2	31.1
630	56.7	21.3	35.2	27.8
800	55.7	22.7	34.5	25.1
1k	59.0	25.1	33.1	24.8

Table A.1: Signal-to-noise ratio for measurement position 1 [dB]

f [Hz]	SNR (p)	SNR (u_x)	SNR (u_y)	SNR (u_z)
100	33.3	6.2	24.4	8.4
125	39.2	14.6	31.9	21.7
160	41.9	18.0	30.0	26.6
200	54.9	36.1	38.6	39.3
250	54.9	32.6	39.6	34.5
315	55.8	29.8	37.9	27.6
400	54.0	32.8	36.0	33.1
500	57.0	30.9	37.3	30.2
630	55.6	27.0	34.8	28.9
800	57.0	30.6	34.4	24.5
1k	57.8	28.1	33.1	23.7

Table A.2: Signal-to-noise ratio for measurement position 2 [dB]

f [Hz]	SNR (p)	SNR (u_x)	SNR (u_y)	SNR (u_z)
100	13.9	20.6	6.0	15.7
125	36.4	33.5	17.1	18.0
160	44.6	35.5	22.8	21.6
200	50.3	38.1	20.8	33.3
250	53.2	38.8	29.1	33.7
315	55.6	34.1	25.7	30.3
400	50.0	34.6	25.0	29.4
500	58.7	34.6	22.0	31.5
630	57.4	33.1	20.1	27.7
800	56.0	32.5	20.3	25.8
1k	57.2	31.1	21.7	24.0

Table A.3: Signal-to-noise ratio for measurement position 3 [dB]

f [Hz]	SNR (p)	SNR (u_x)	SNR (u_y)	SNR (u_z)
100	36.6	24.2	22.1	12.5
125	49.2	36.7	33.8	23.2
160	51.3	39.4	28.8	23.3
200	59.9	40.1	33.2	32.3
250	55.9	34.7	32.4	33.0
315	47.6	32.8	28.7	28.5
400	52.8	32.6	34.9	29.6
500	57.4	33.1	29.6	28.4
630	55.1	31.8	31.0	22.5
800	58.2	33.4	28.0	21.3
1k	55.9	34.3	25.1	20.0

Table A.4: Signal-to-noise ratio for measurement position 4 [dB]

A.2 Transfer functions

Section A.2 includes the transfer functions $H_p(\omega)$ for all four measurement positions and all three measurement serieses.

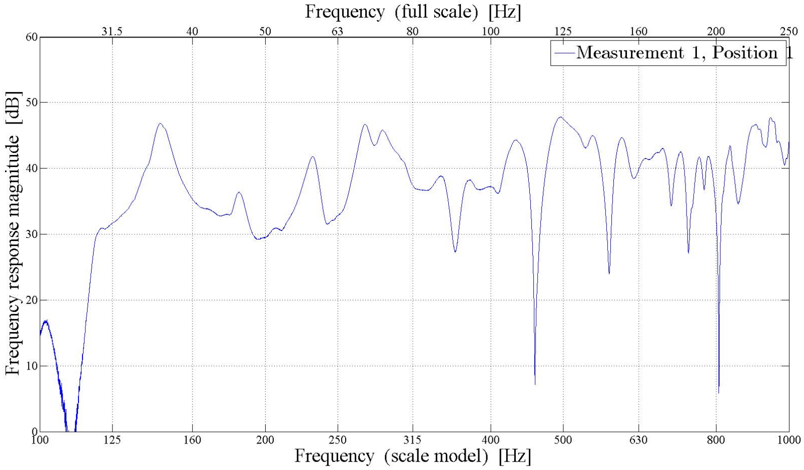

(a) $H_{p,1}$, position 1

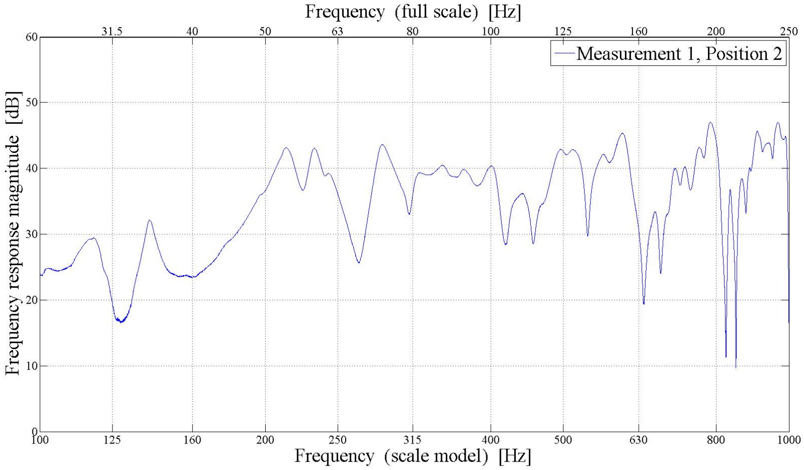

(b) $H_{p,1}$, position 2

Figure A.1: Transfer functions $H_{p,1}$ from measurement series 1

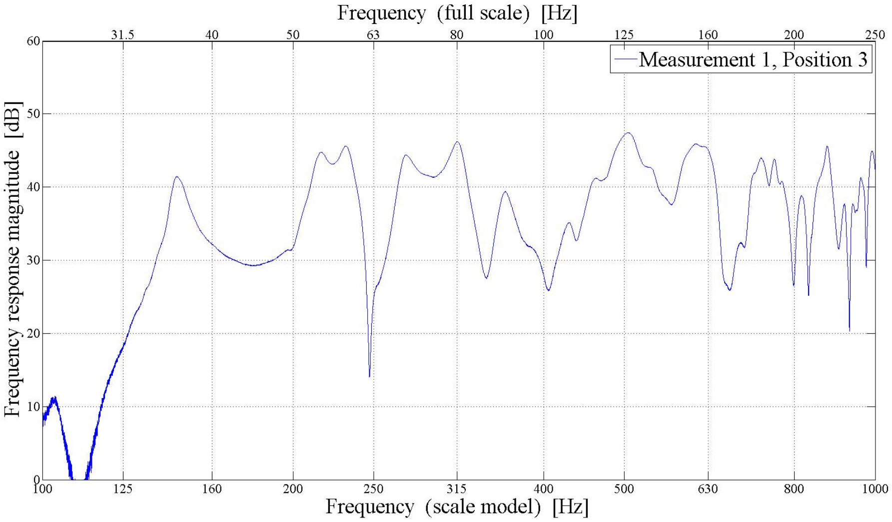

(c) $H_{p,1}$, position 3

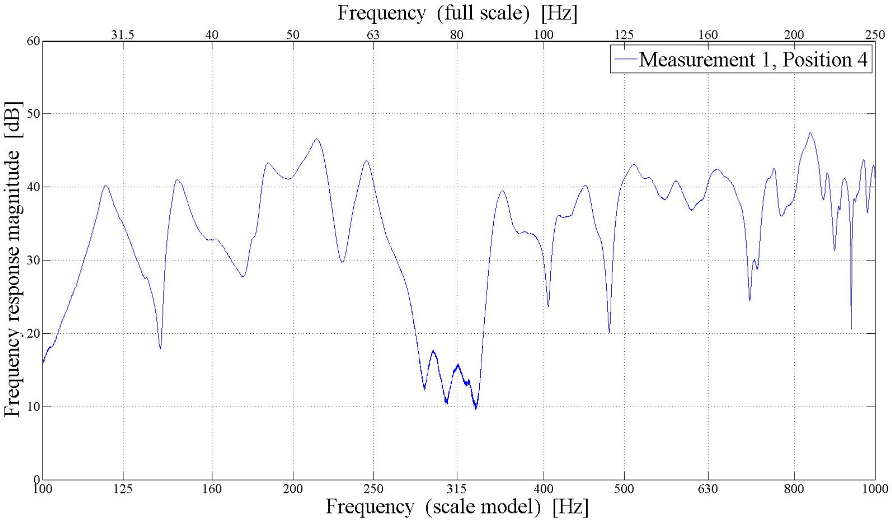

(d) $H_{p,1}$, position 4

Figure A.1: Transfer functions $H_{p,1}$ from measurement series 1

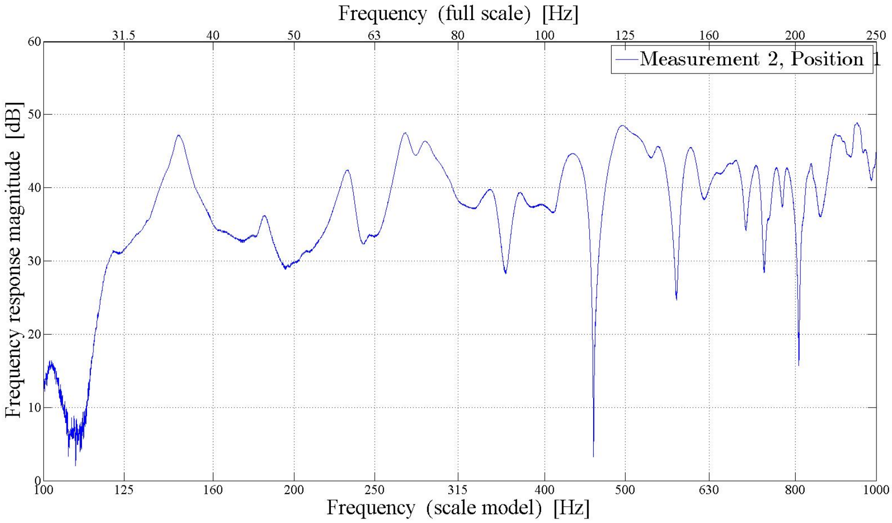

(a) $H_{p,2}$, position 1

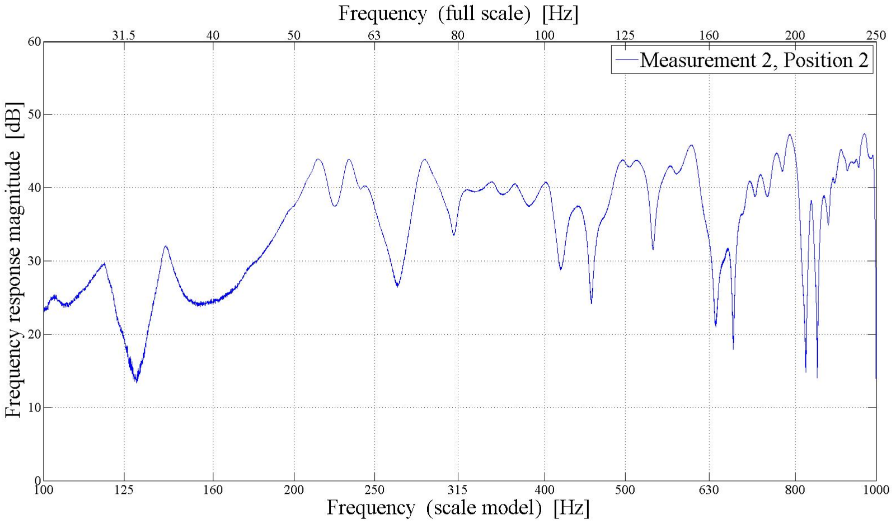

(b) $H_{p,2}$, position 2

Figure A.2: Transfer functions $H_{p,2}$ from measurement series 2

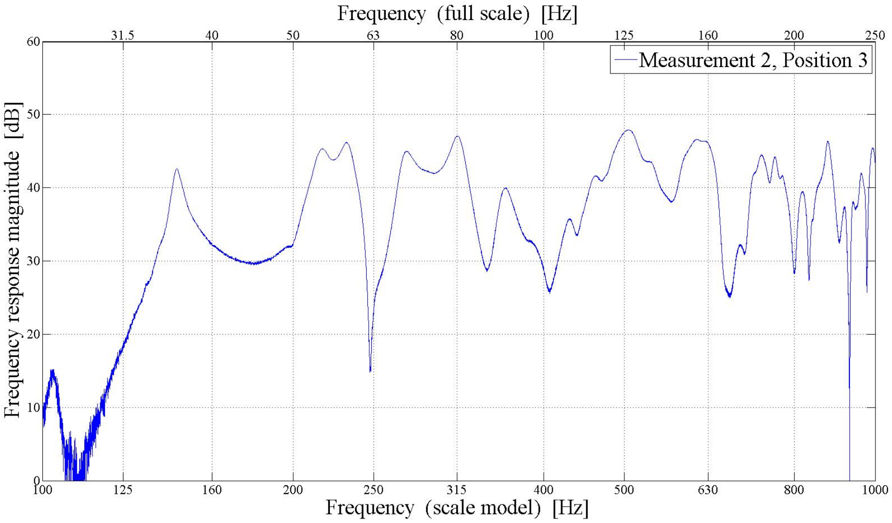

(c) $H_{p,2}$, position 3

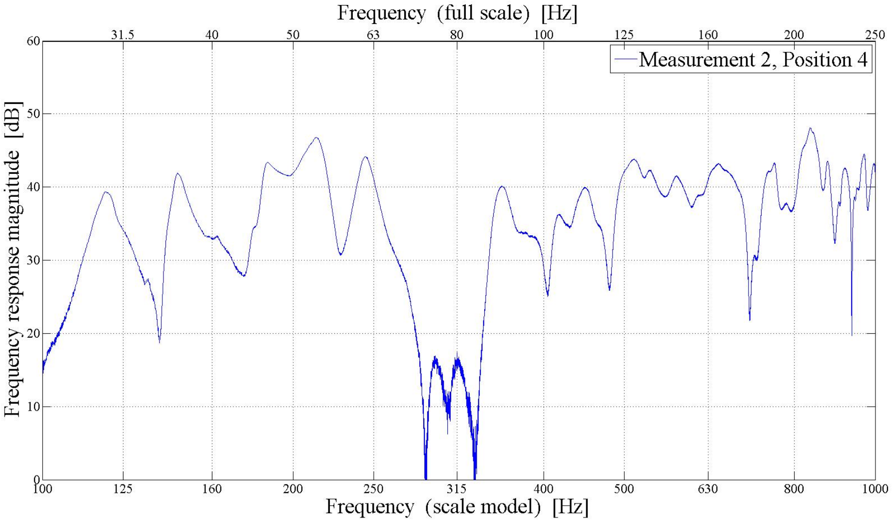

(d) $H_{p,2}$, position 4

Figure A.2: Transfer functions $H_{p,2}$ from measurement series 2

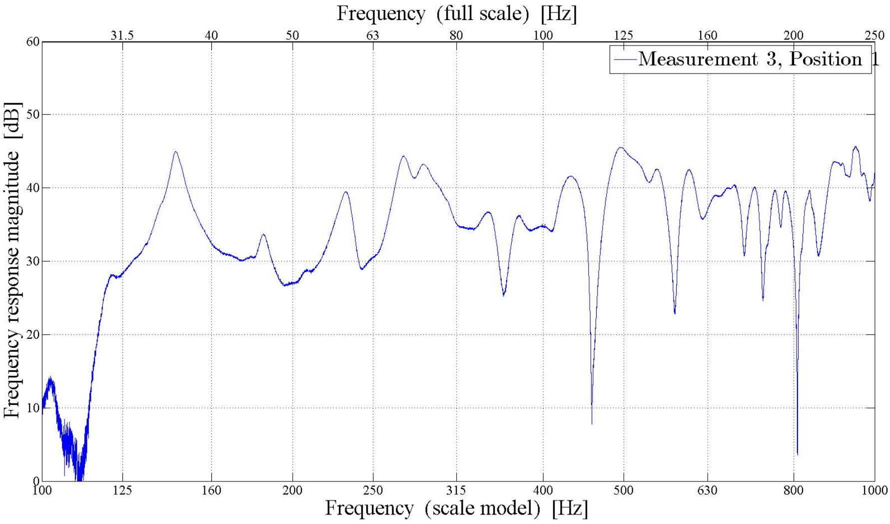

(a) $H_{p,3}$, position 1

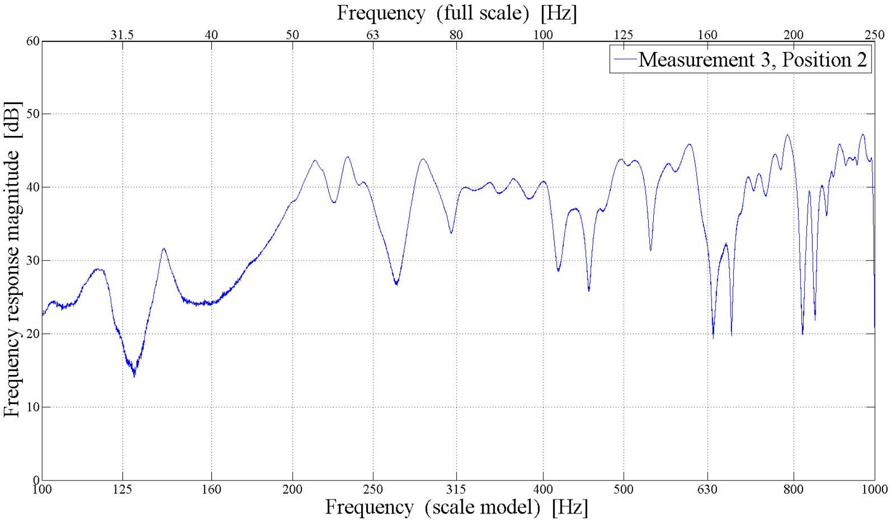

(b) $H_{p,3}$, position 2

Figure A.3: Transfer functions $H_{p,3}$ from measurement series 3

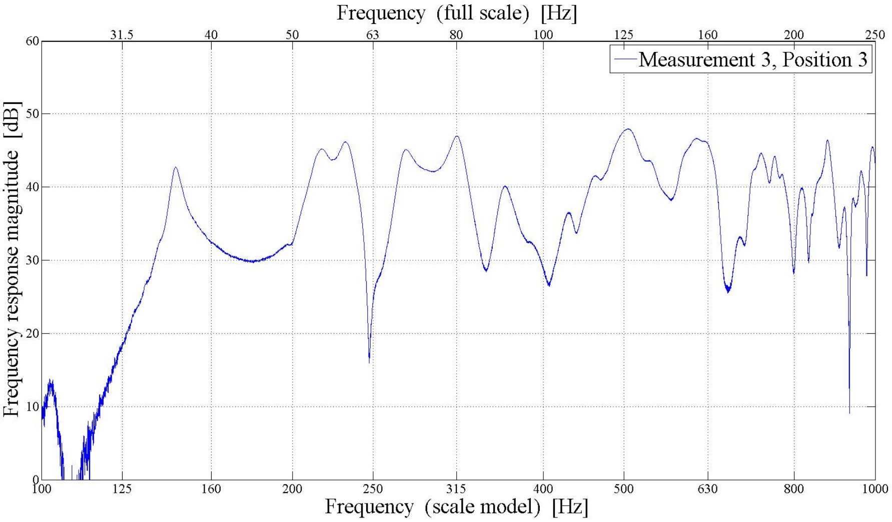

(c) $H_{p,3}$, position 3

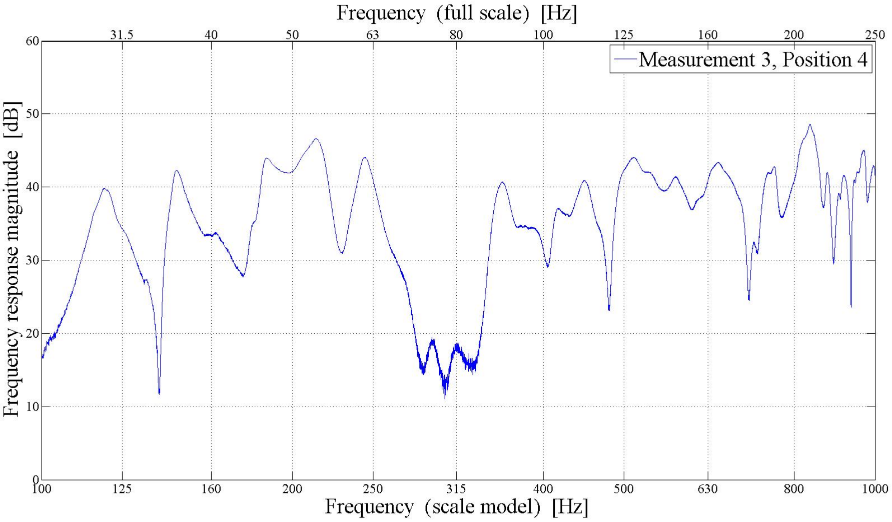

(d) $H_{p,3}$, position 4

Figure A.3: Transfer functions $H_{p,3}$ from measurement series 3

A.3 Filter parameters

Section A.3 contains the WinMLS-calculated 1/3 octave band T_{30} values and corresponding filterwidths B for all 3 measurement serieses.

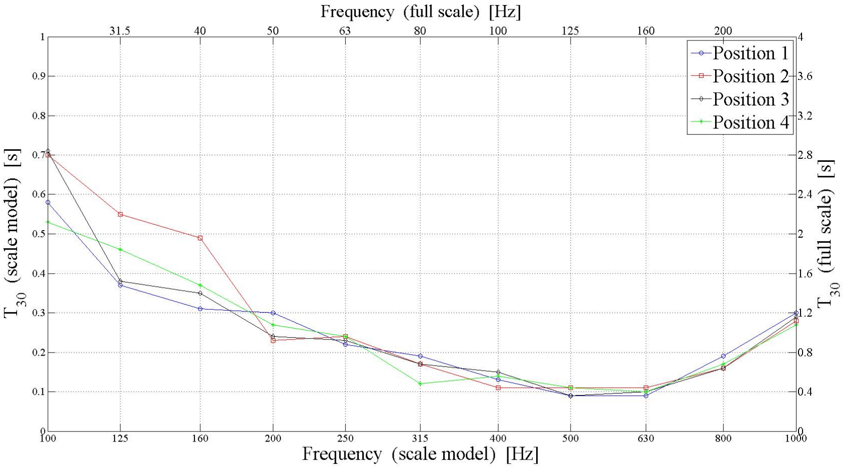

(a) 1/3 octave band T_{30}

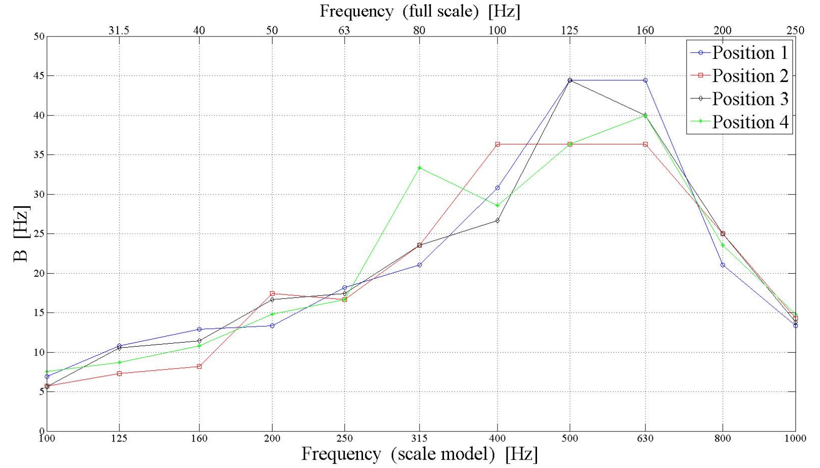

(b) 1/3 octave band B

Figure A.4: WinMLS-calculated T_{30} & B from measurement series 1

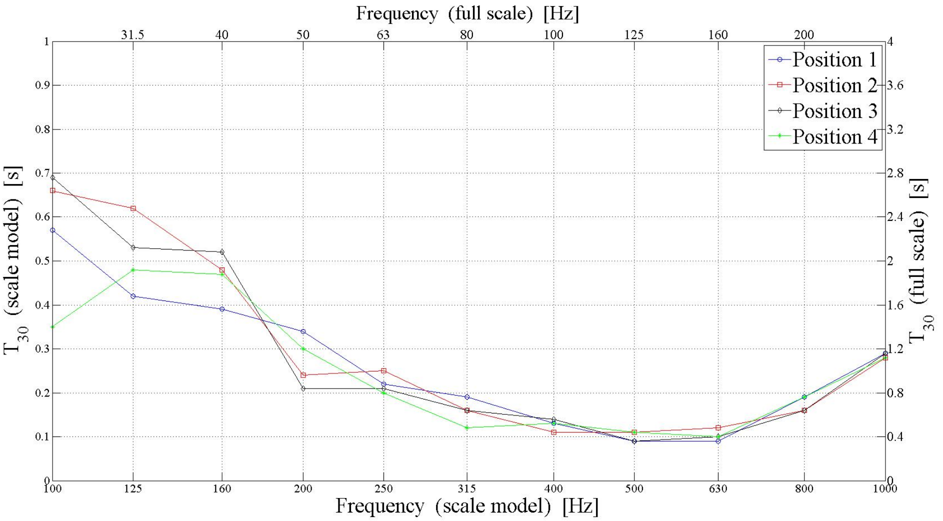

(a) 1/3 octave band T_{30}

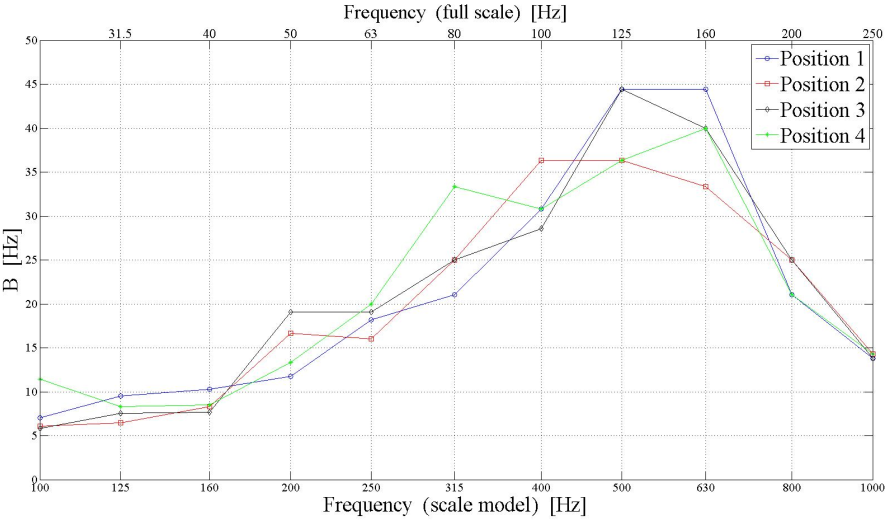

(b) 1/3 octave band B

Figure A.5: WinMLS-calculated T_{30} & B from measurement series 2

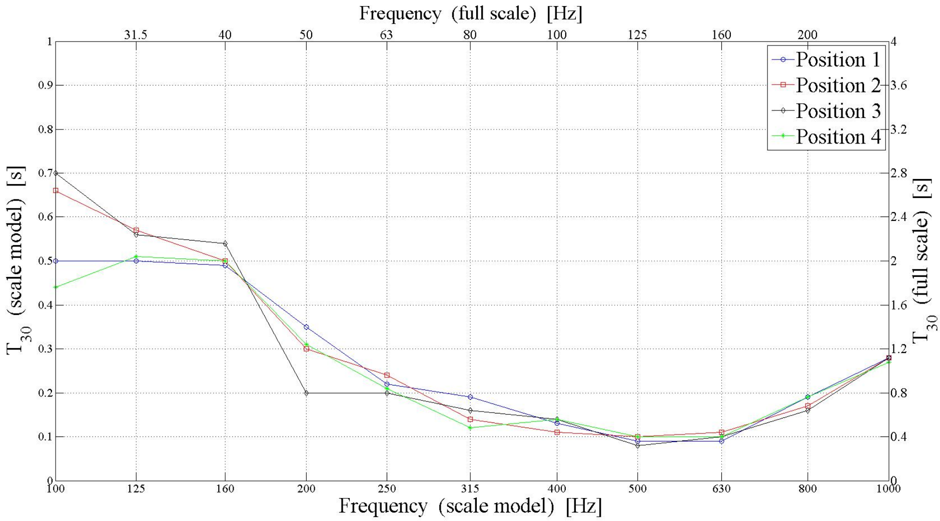

(a) 1/3 octave band T_{30}

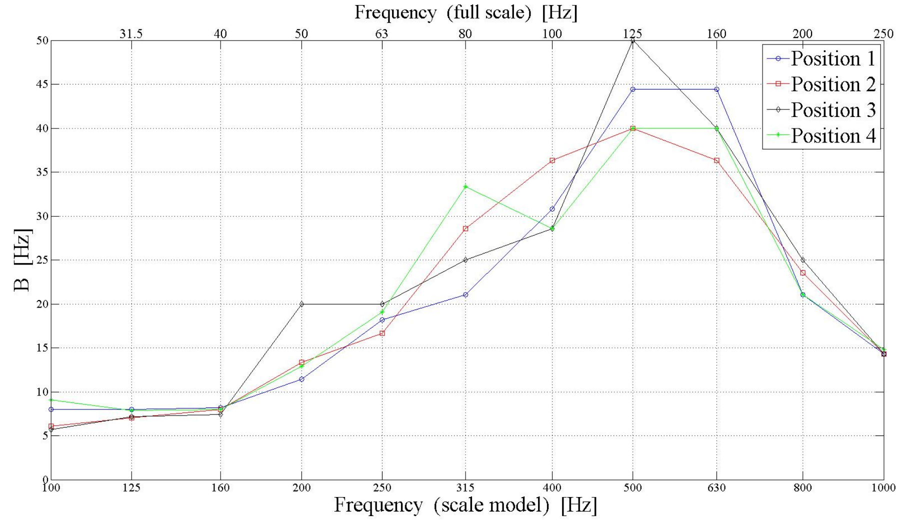

(b) 1/3 octave band B

Figure A.6: WinMLS-calculated T_{30} & B from measurement series 3

A.4 Mode processing

Section A.4 includes the transfer functions, the filtered impulse responses, and the energy decay curves of each of the 17 modes selected for analysis from the measurement position 1 and measurement series 1 impulse response. The energy decay curve also includes the fitted linear regression line used for determining T.

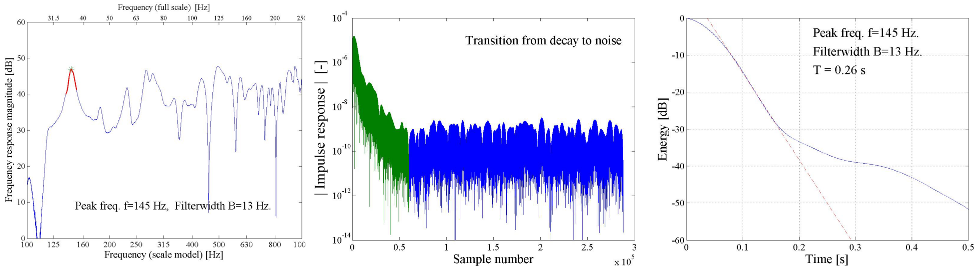

(a) Mode 1, transfer function

(b) Mode 1, filtered impulse response

(c) Mode 1, fitted line energy decay

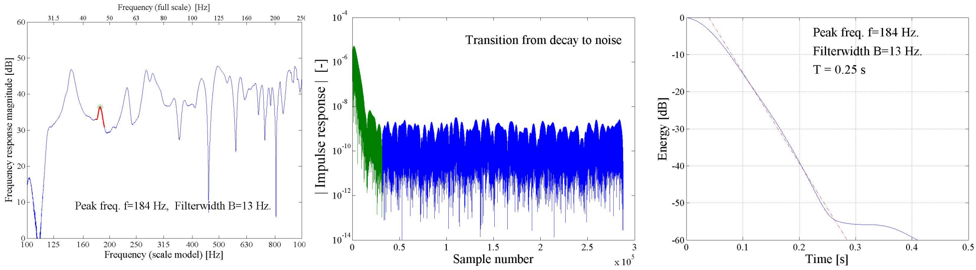

(d) Mode 2, transfer function

(e) Mode 2, filtered impulse response

(f) Mode 2, fitted line energy decay

Figure A.7: Measurement 1, position 1, Modes 1-2

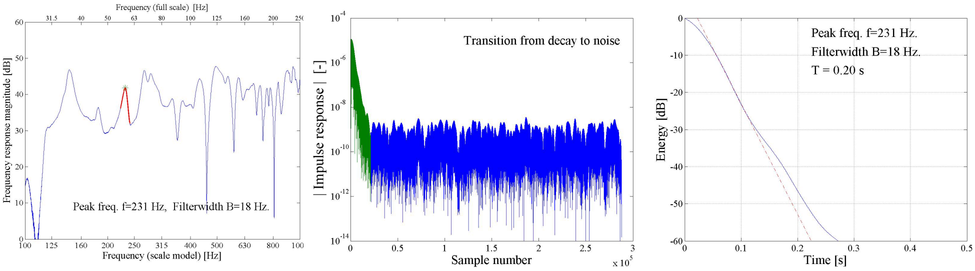

(a) Mode 3, transfer function

(b) Mode 3, filtered impulse response

(c) Mode 3, fitted line energy decay

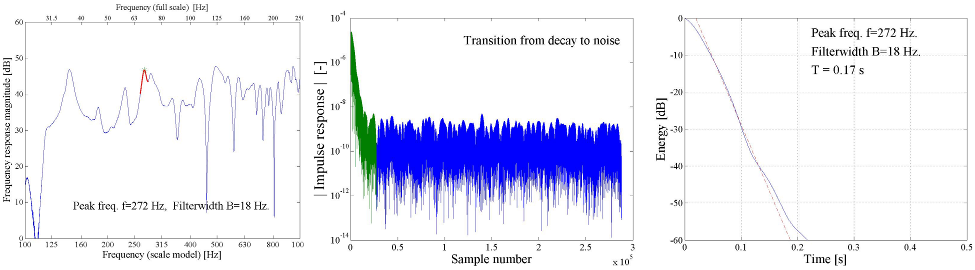

(d) Mode 4, transfer function

(e) Mode 4, filtered impulse response

(f) Mode 4, fitted line energy decay

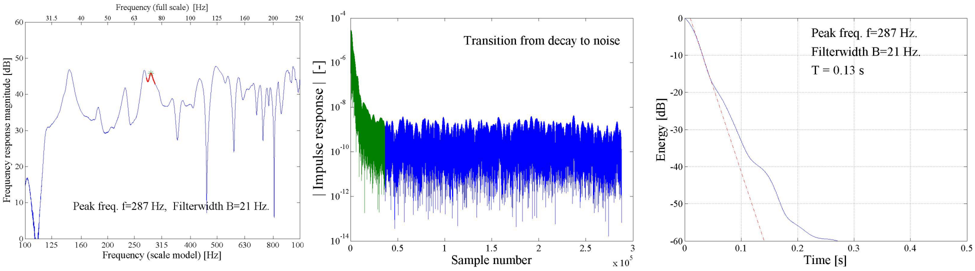

(g) Mode 5, transfer function

(h) Mode 5, filtered impulse response

(i) Mode 5, fitted line energy decay

Figure A.8: Measurement 1, position 1, Modes 3-5

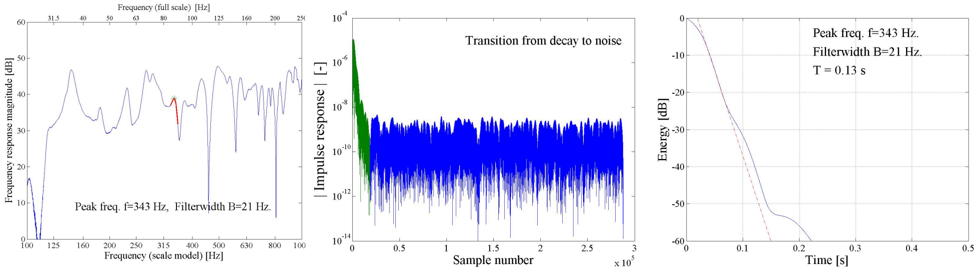

(a) Mode 6, transfer function

(b) Mode 6, filtered impulse response

(c) Mode 6, fitted line energy decay

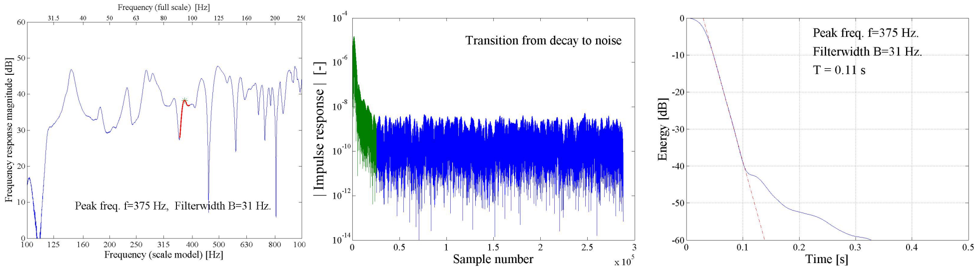

(d) Mode 7, transfer function

(e) Mode 7, filtered impulse response

(f) Mode 7, fitted line energy decay

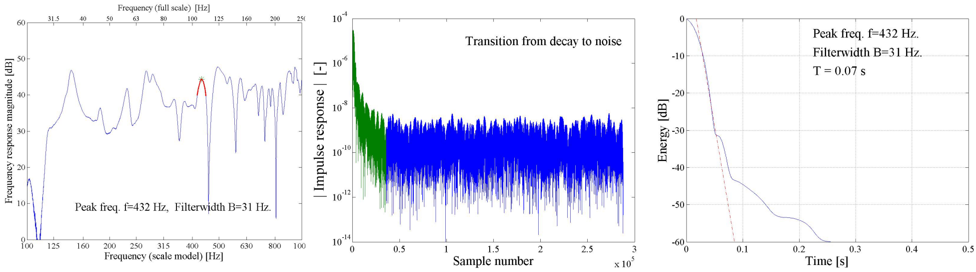

(g) Mode 8, transfer function

(h) Mode 8, filtered impulse response

(i) Mode 8, fitted line energy decay

Figure A.9: Measurement 1, position 1, Modes 6-8

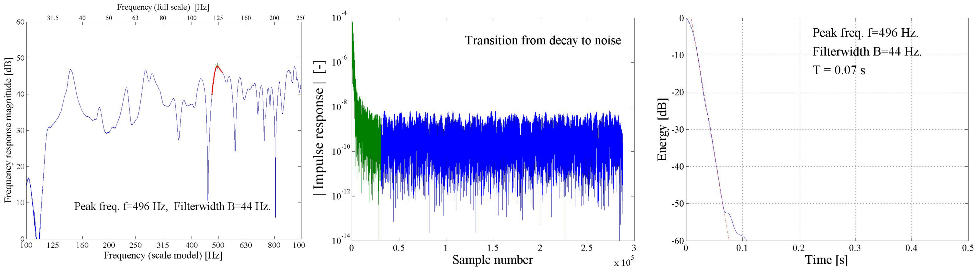

(a) Mode 9, transfer function

(b) Mode 9, filtered impulse response

(c) Mode 9, fitted line energy decay

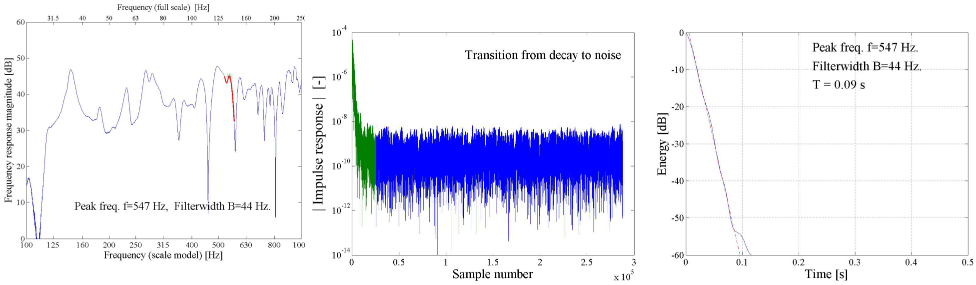

(d) Mode 10, transfer function

(e) Mode 10, filtered impulse response

(f) Mode 10, fitted line energy decay

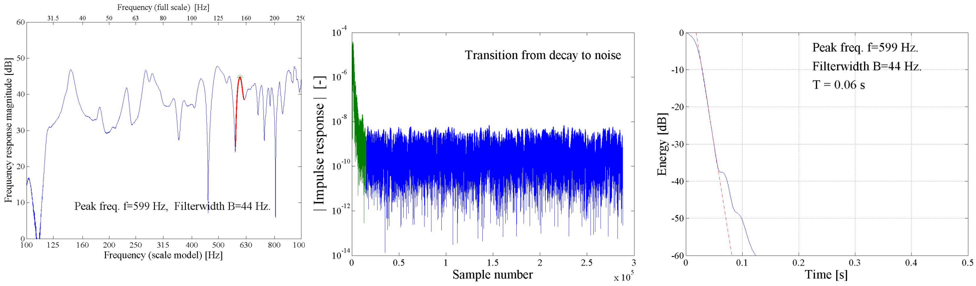

(g) Mode 11, transfer function

(h) Mode 11, filtered impulse response

(i) Mode 11, fitted line energy decay

Figure A.10: Measurement 1, position 1, Modes 9-11

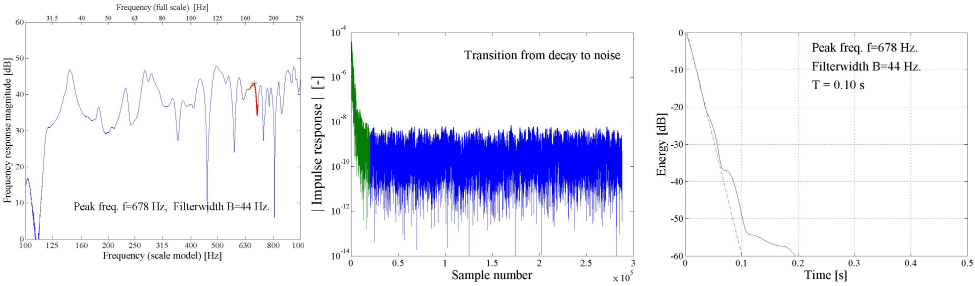

(a) Mode 12, transfer function

(b) Mode 12, filtered impulse response

(c) Mode 12, fitted line energy decay

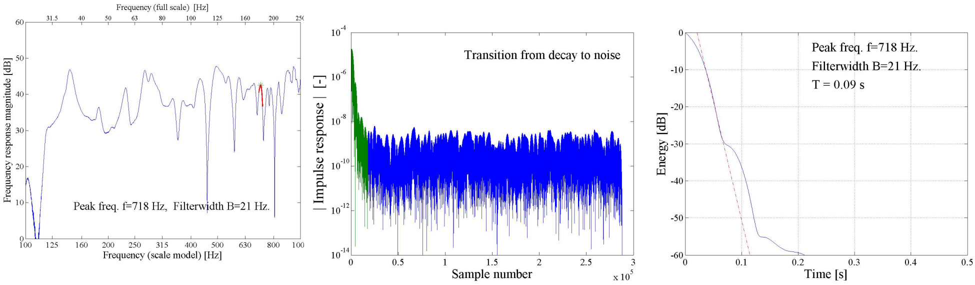

(d) Mode 13, transfer function

(e) Mode 13, filtered impulse response

(f) Mode 13, fitted line energy decay

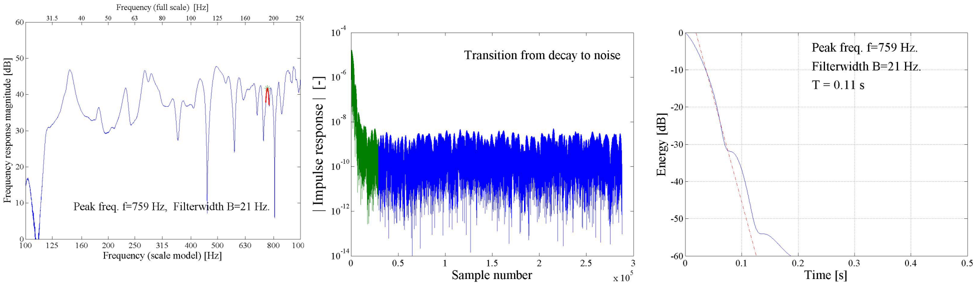

(g) Mode 14, transfer function

(h) Mode 14, filtered impulse response

(i) Mode 14, fitted line energy decay

Figure A.11: Measurement 1, position 1, Modes 12-14

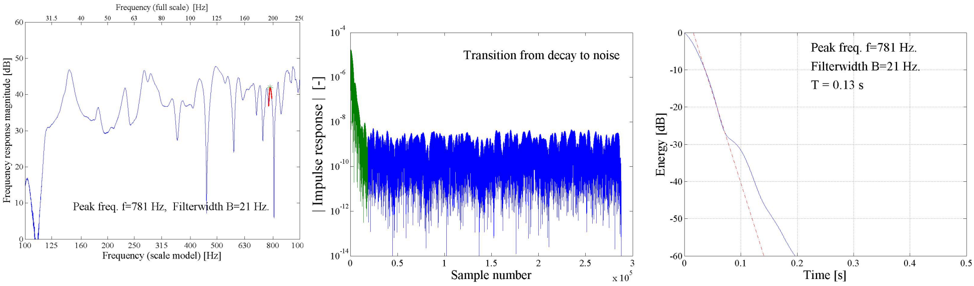

(a) Mode 15, transfer function

(b) Mode 15, filtered impulse response

(c) Mode 15, fitted line energy decay

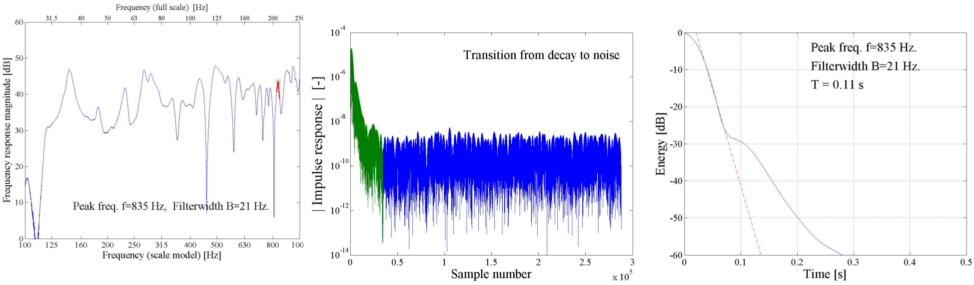

(d) Mode 16, transfer function

(e) Mode 16, filtered impulse response

(f) Mode 16, fitted line energy decay

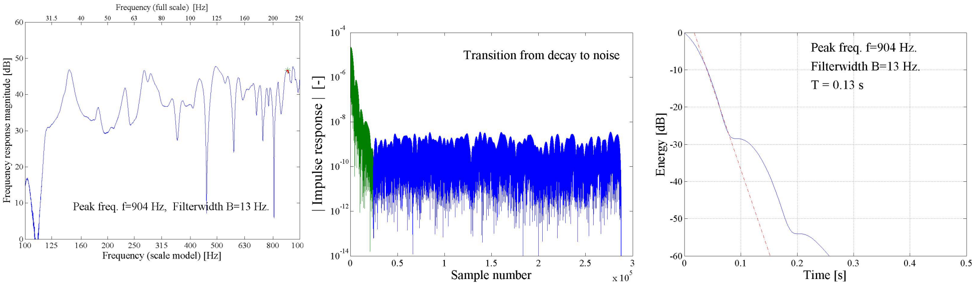

(g) Mode 17, transfer function

(h) Mode 17, filtered impulse response

(i) Mode 17, fitted line energy decay

Figure A.12: Measurement 1, position 1, Modes 15-17

A.5 Estimation of modal T

Section A.5 repeats the estimated T for all 204 mode peaks result presented in Chapter 4 in a larger figure.

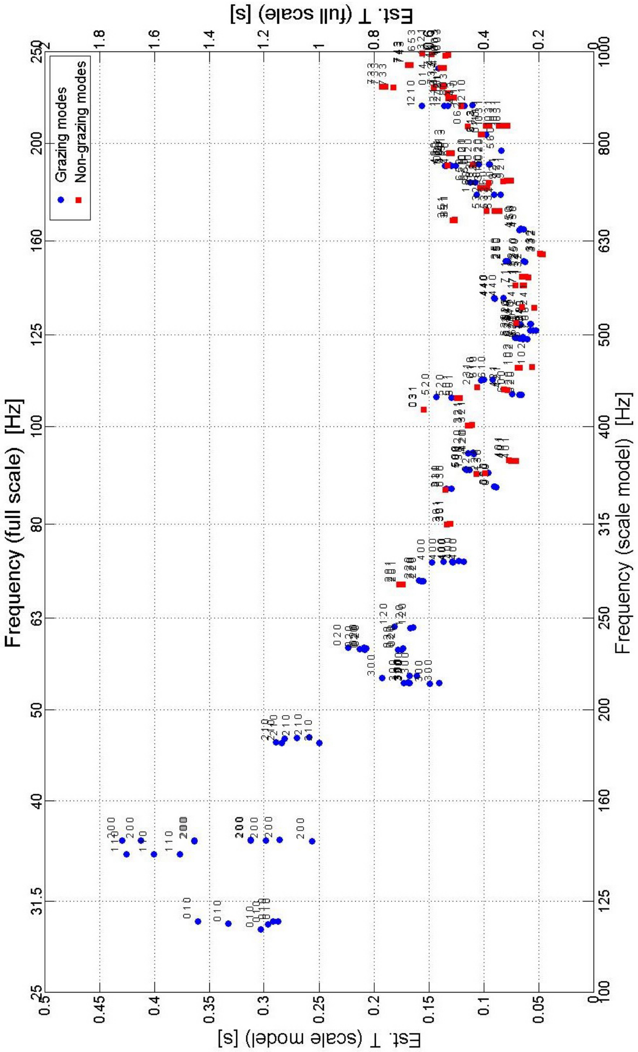

Figure A.13: Estimated T for 204 mode peaks selected from 12 transfer functions H_p

A.6 The influence of the filterwidth

The energy decay for the 145 Hz peak with fitted linear regression line is included for measurement positions 1,3 and 4, and filterwidths 3,6,9 and 11 Hz.

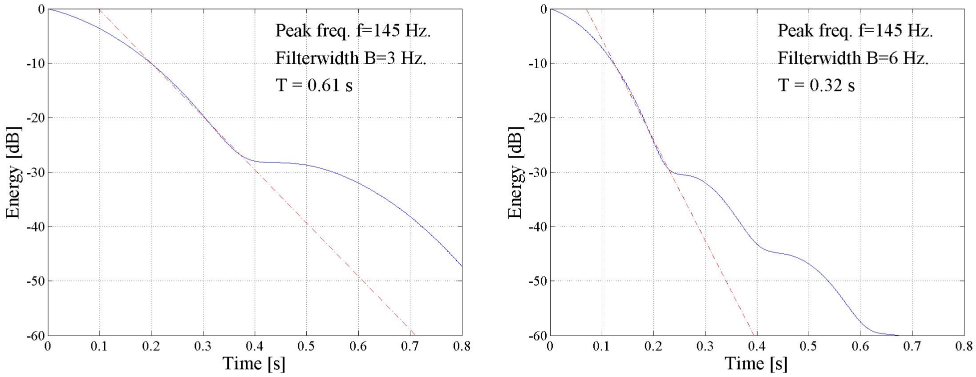

(a) Position 1, filterwidth 3 Hz

(b) Position 1, filterwidth 6 Hz

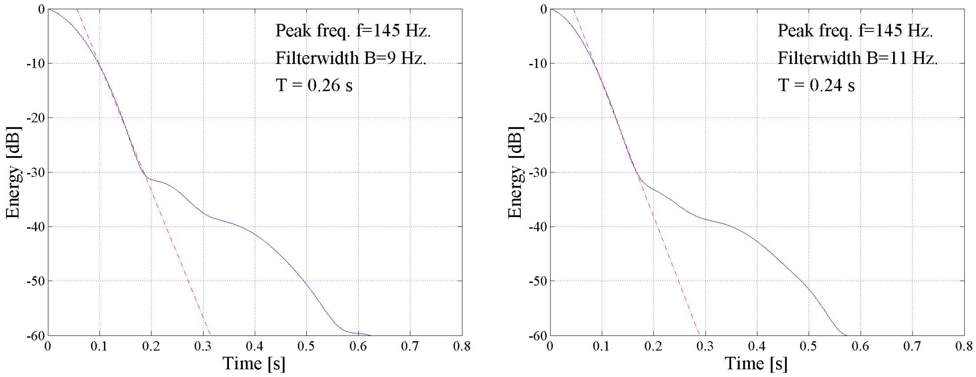

(c) Position 1, filterwidth 9 Hz

(d) Position 1, filterwidth 11 Hz

Figure A.14: Position 1, filtered energy decay

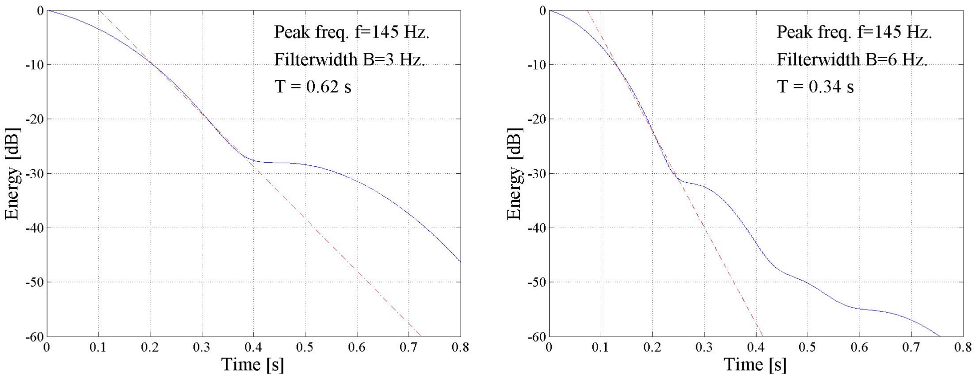

(a) Position 3, filterwidth 3 Hz

(b) Position 3, filterwidth 6 Hz

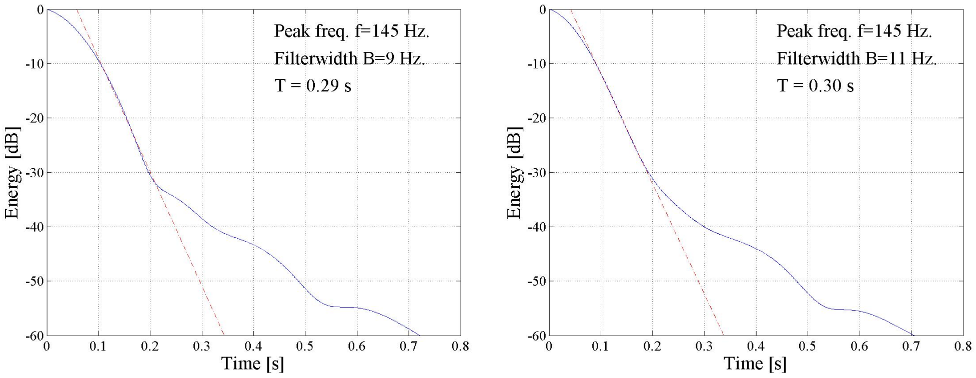

(c) Position 3, filterwidth 9 Hz

(d) Position 3, filterwidth 11 Hz

Figure A.15: Position 3, filtered energy decay

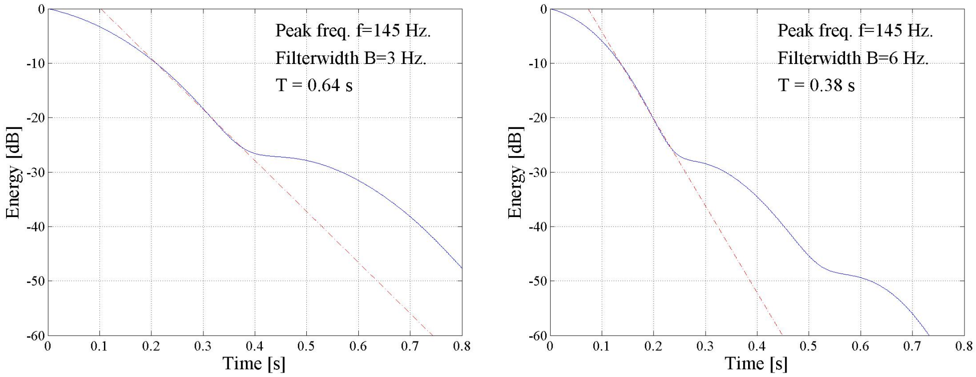

(a) Position 4, filterwidth 3 Hz

(b) Position 4, filterwidth 6 Hz

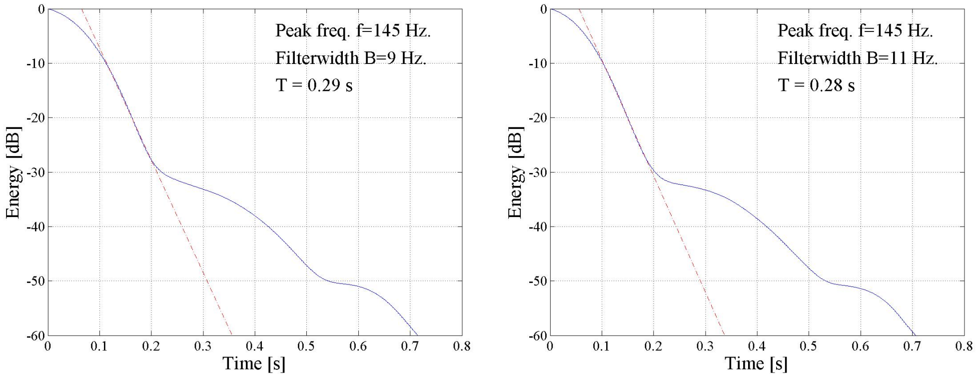

(c) Position 4, filterwidth 9 Hz

(d) Position 4, filterwidth 11 Hz

Figure A.16: Position 4, filtered energy decay

Appendix B

Additional approaches

Appendix B contains the intermediate measurement results and post-processing results from the *additional approaches* sections of the results presented in Chapter 4.

B.1 Calculated β and $T(\beta)$

Section B.1 contains the calculated β-values and their corresponding T-values for all 4 measurement positions.

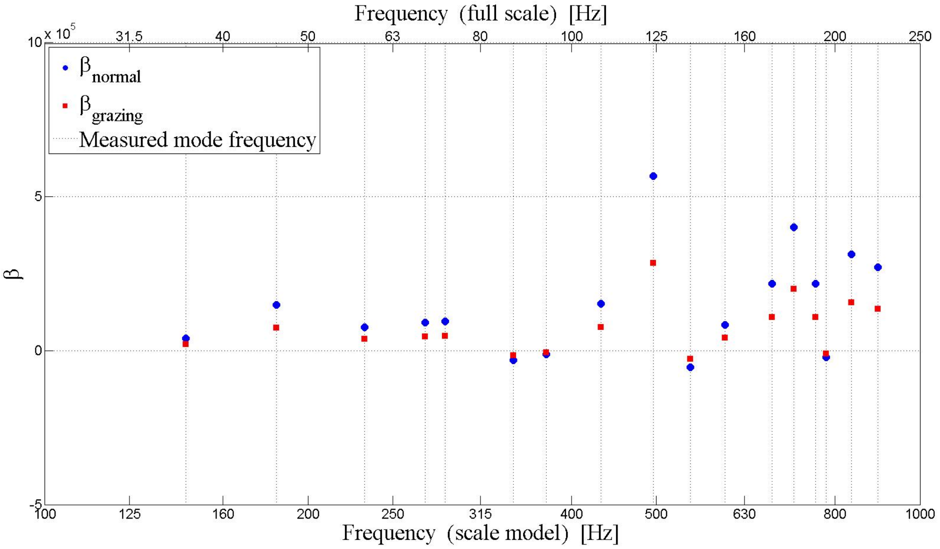

(a) β, position 1

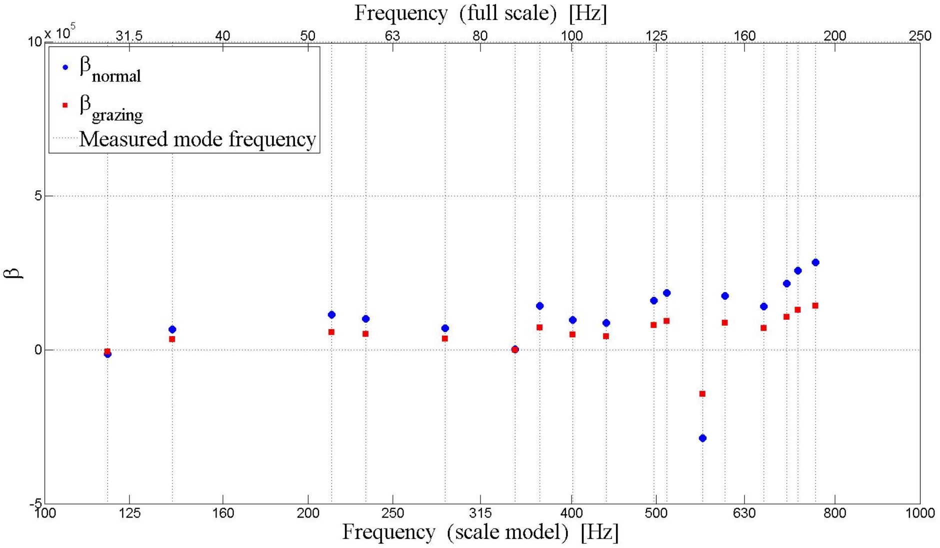

(b) β, position 2

Figure B.1: Calculated absorption coefficients β

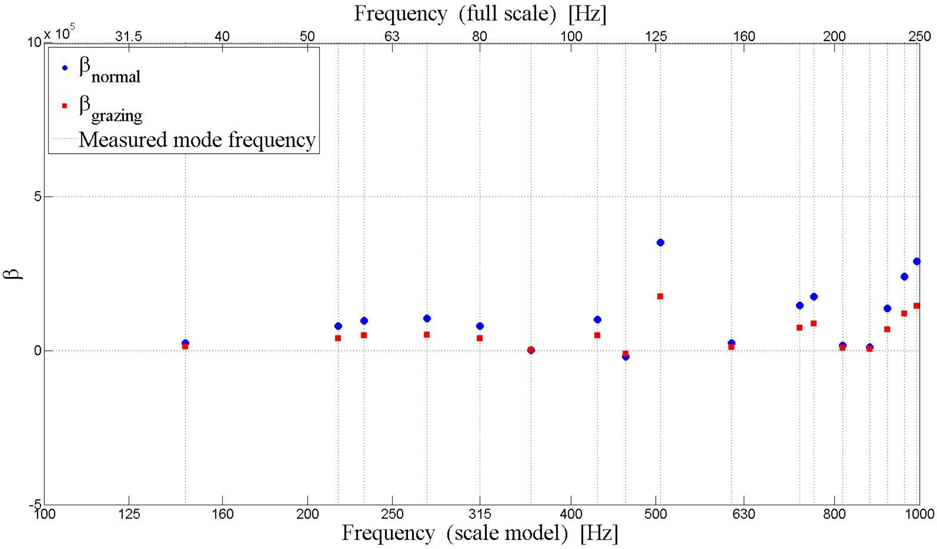

(c) β, position 3

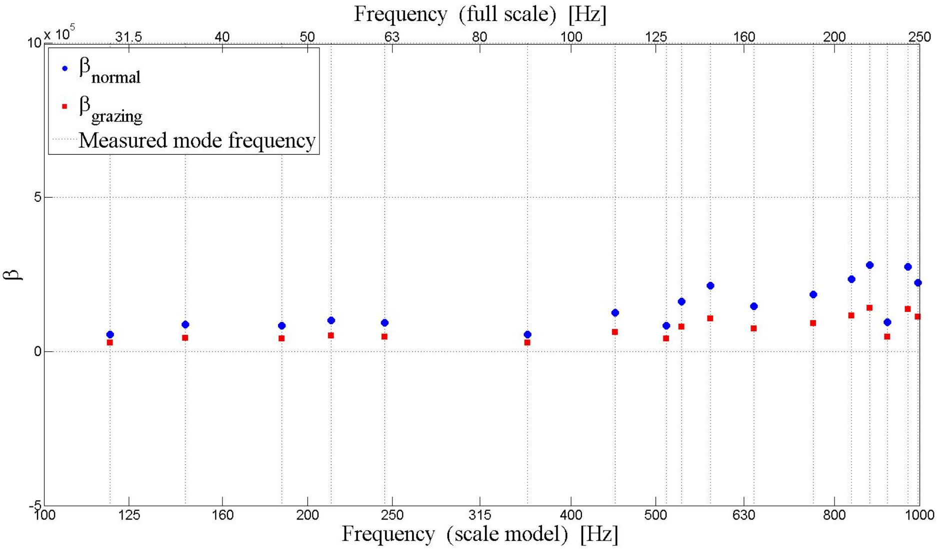

(d) β, position 4

Figure B.1: Calculated absorption coefficients β

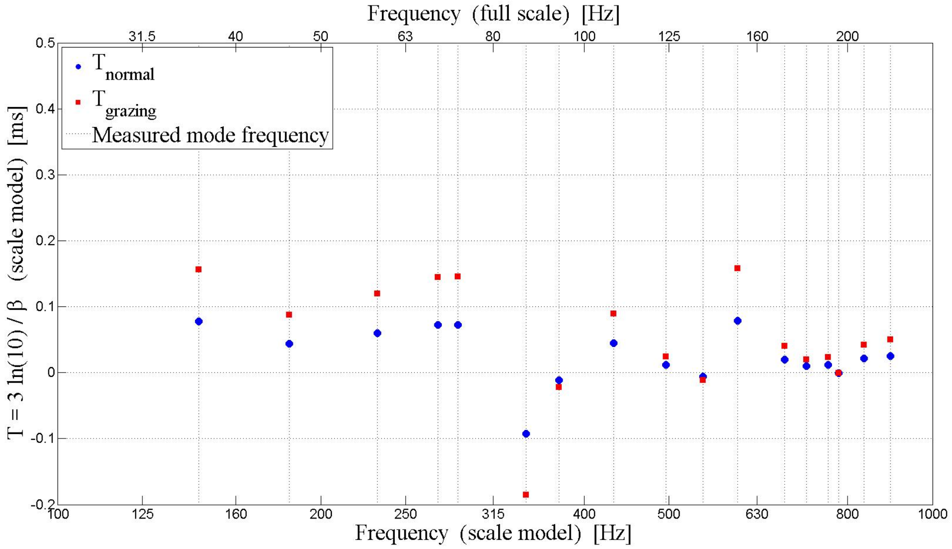

(a) $T(\beta)$, position 1

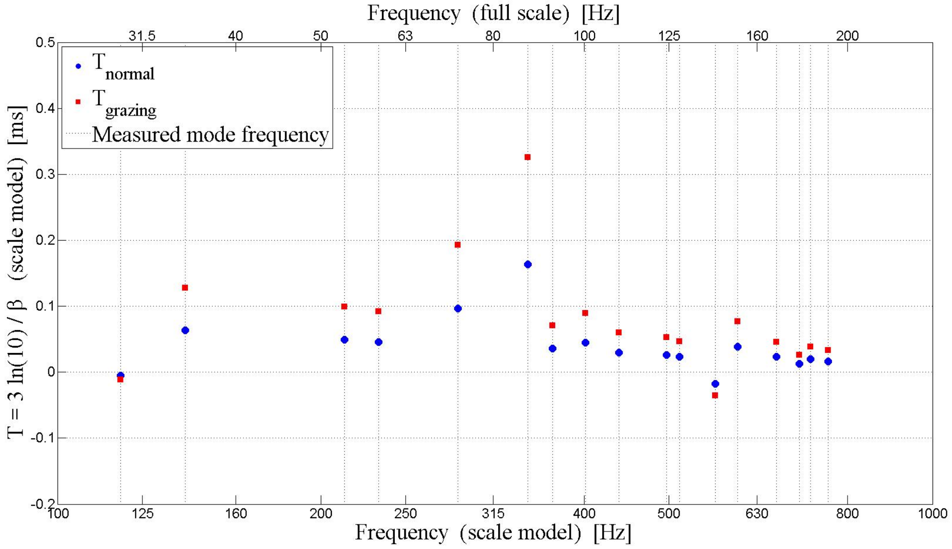

(b) $T(\beta)$, position 2

Figure B.2: Calculated $T(\beta)$

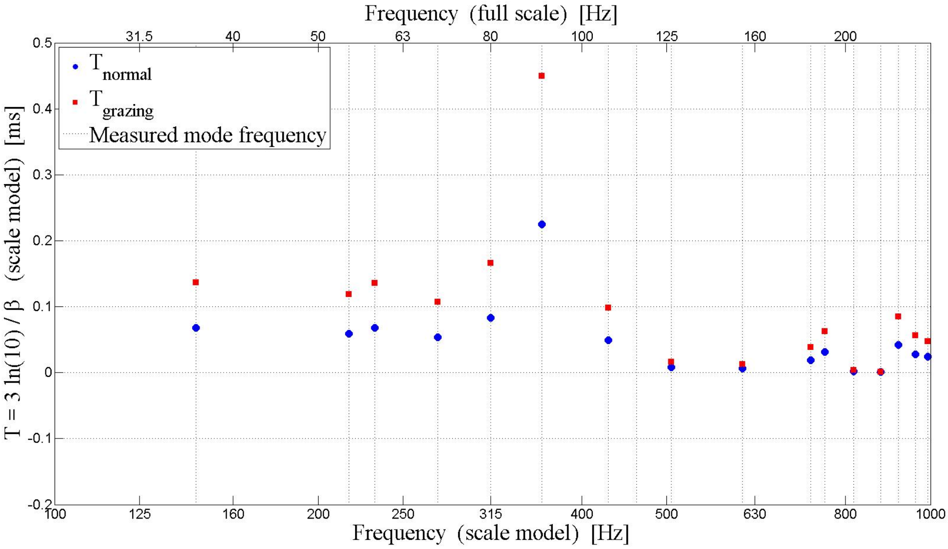

(c) $T(\beta)$, position 3

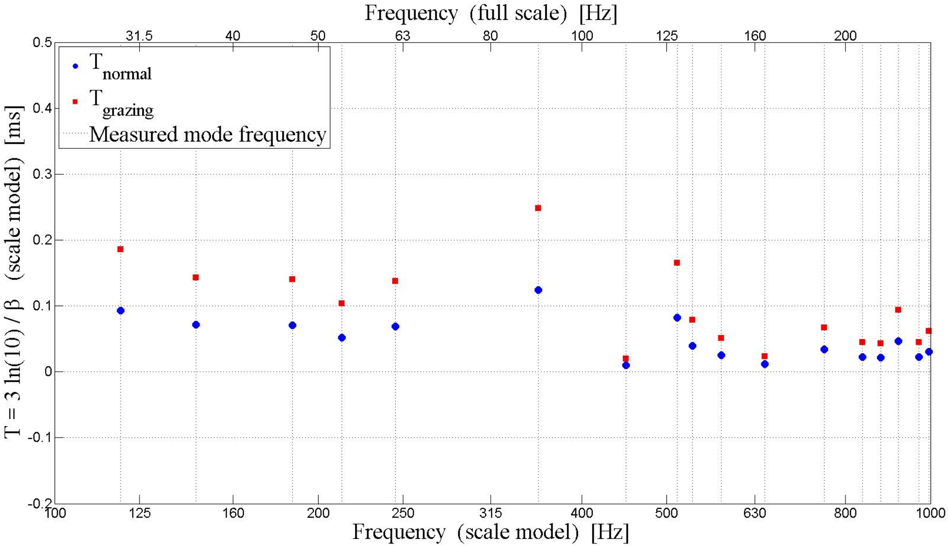

(d) $T(\beta)$, position 4

Figure B.2: Calculated $T(\beta)$

B.2 The intensity profile $I_z(d)$

Section B.2 includes all 12 measurements of I_z divided into figures for the 4 measurement positions. In addition, the intersection points of the first (lowest) mode frequencies are examined in closer detail for each of the 4 measurement positions. These close-ups are presented in Figures B.7, B.8, B.9 and B.10.

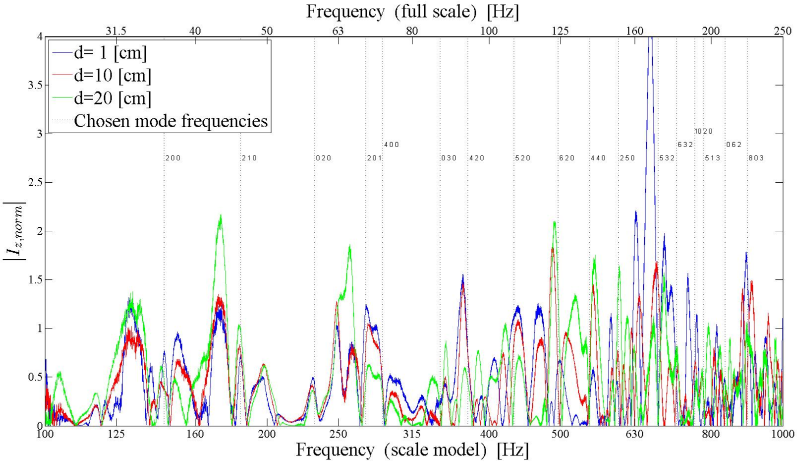

Figure B.3: $I_z(d)$, position 1

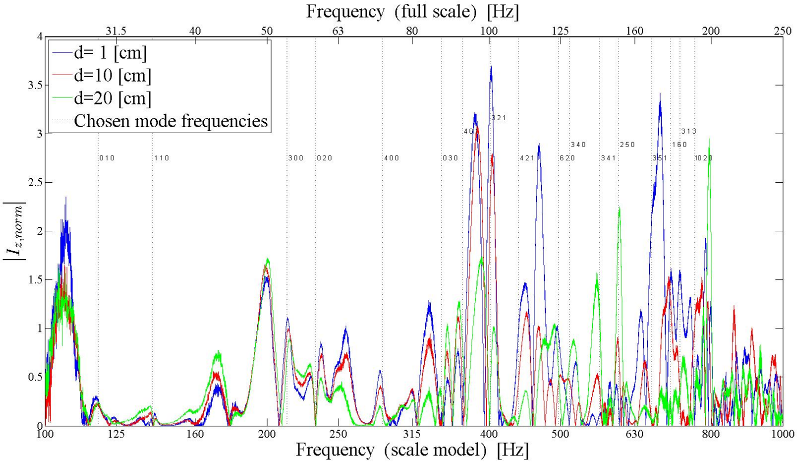

Figure B.4: $I_z(d)$, position 2

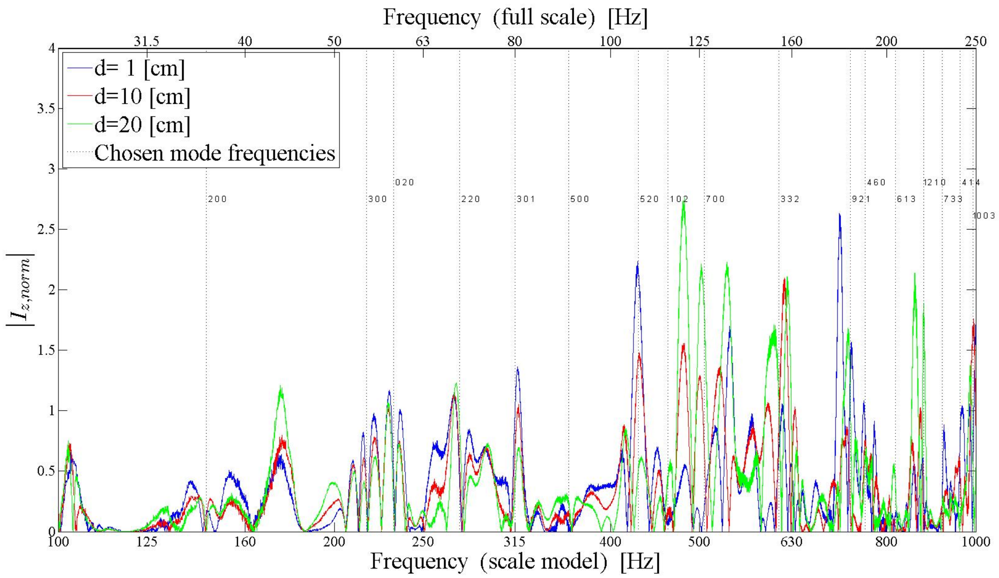

Figure B.5: $I_z(d)$, position 3

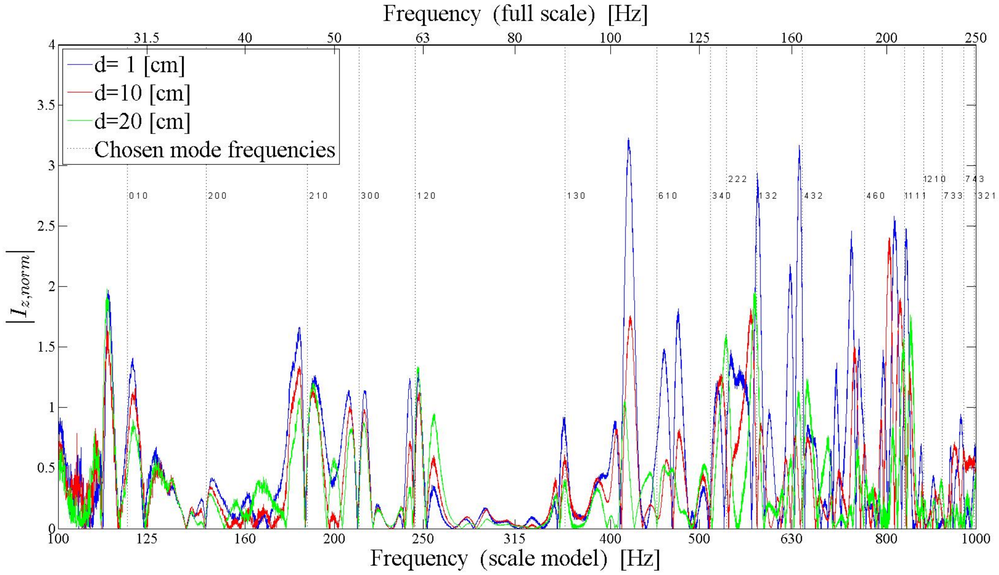

Figure B.6: $I_z(d)$, position 4

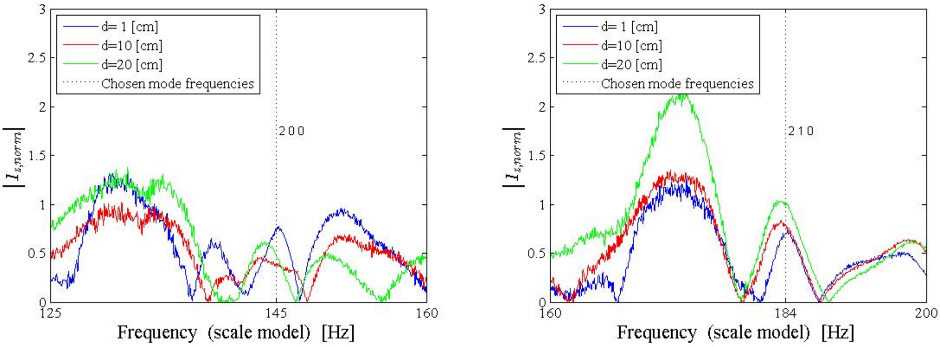

(a) $I_z(d)$, position 1 – 1st mode

(b) $I_z(d)$, position 1 – 2nd mode

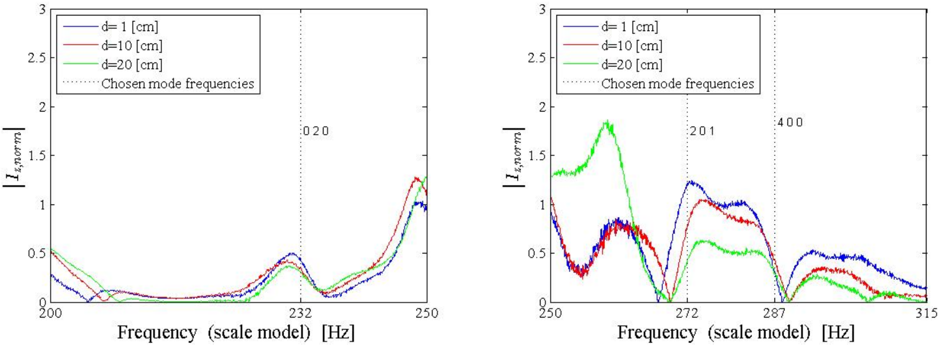

(c) $I_z(d)$, position 1 – 3rd mode

(d) $I_z(d)$, position 1 – 4th and 5th mode

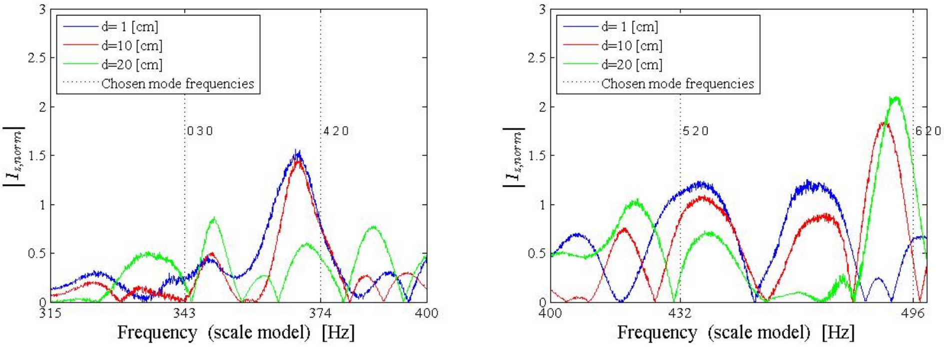

(e) $I_z(d)$, position 1 – 6th and 7th mode

(f) $I_z(d)$, position 1 – 8th and 9th mode

Figure B.7: $I_z(d)$, position 1, frequency scale zoom

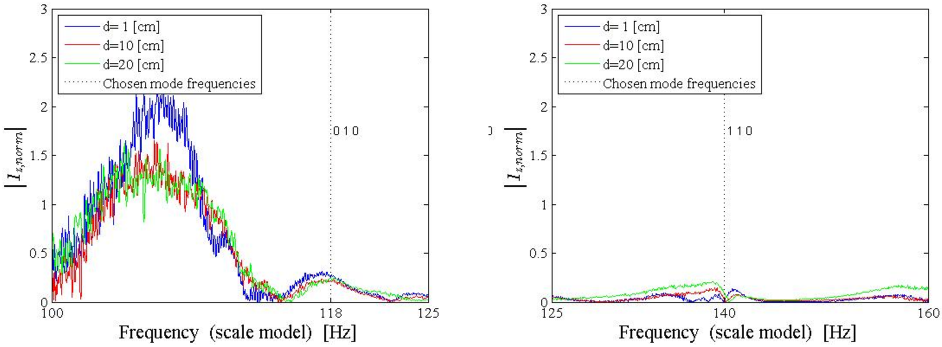

(a) $I_z(d)$, position 2 – 1st mode **(b)** $I_z(d)$, position 2 – 2nd mode

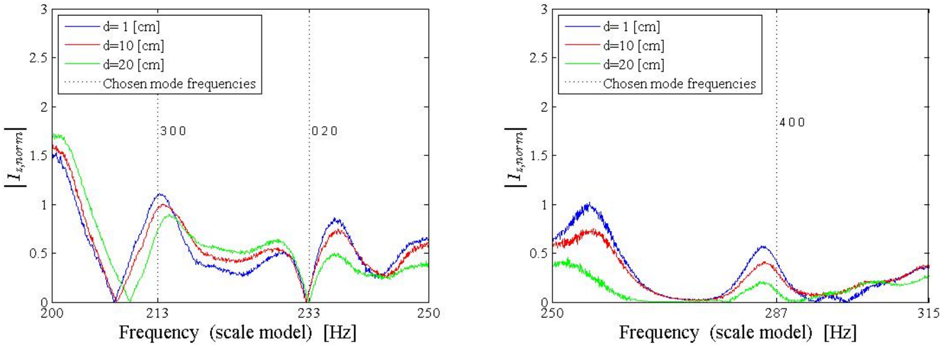

(c) $I_z(d)$, position 2 – 3rd and 4th mode **(d)** $I_z(d)$, position 2 – 5th mode

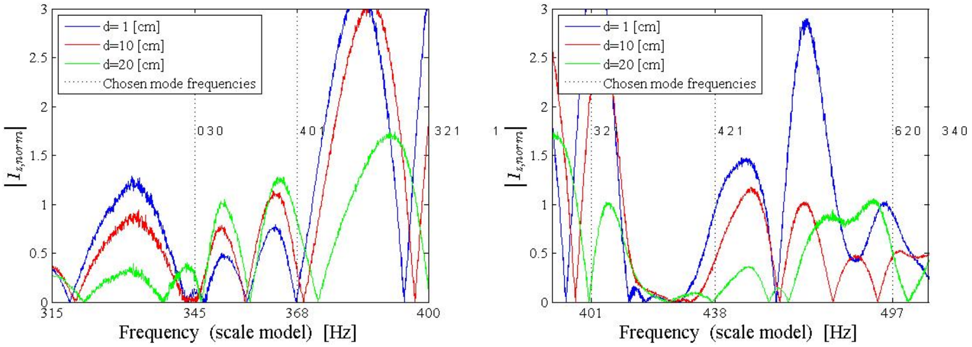

(e) $I_z(d)$, position 2 – 6th and 7th mode **(f)** $I_z(d)$, position 2 – 8th, 9th and 10th mode

Figure B.8: $I_z(d)$, position 2, frequency scale zoom

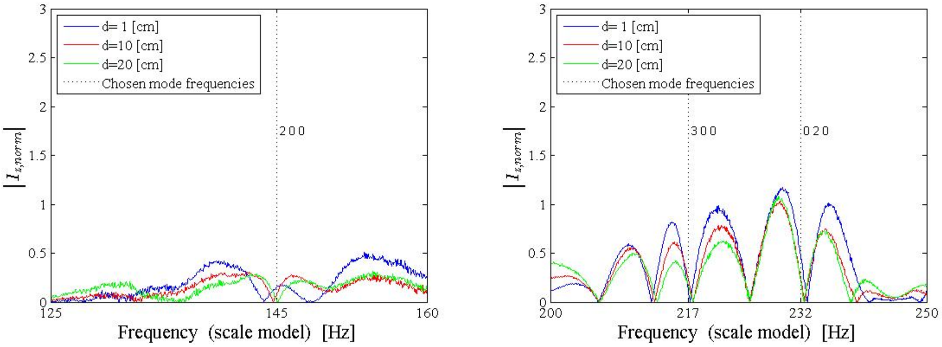

(a) $I_z(d)$, position 3 – 1st mode

(b) $I_z(d)$, position 3 – 2nd and 3rd mode

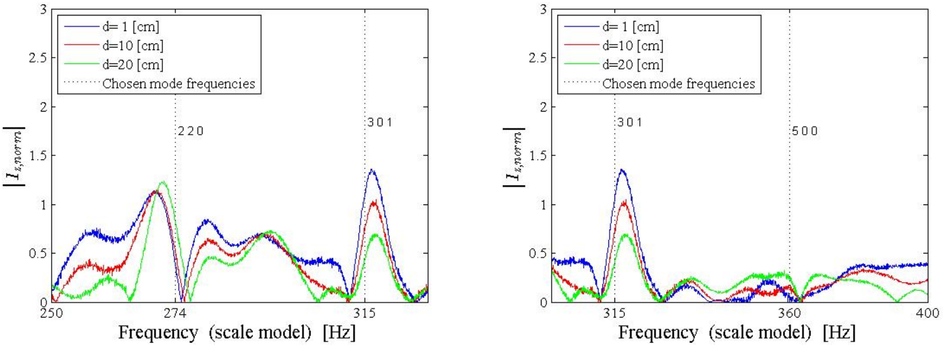

(c) $I_z(d)$, position 3 – 4th and 5th mode

(d) $I_z(d)$, position 3 – 6th and 7th mode

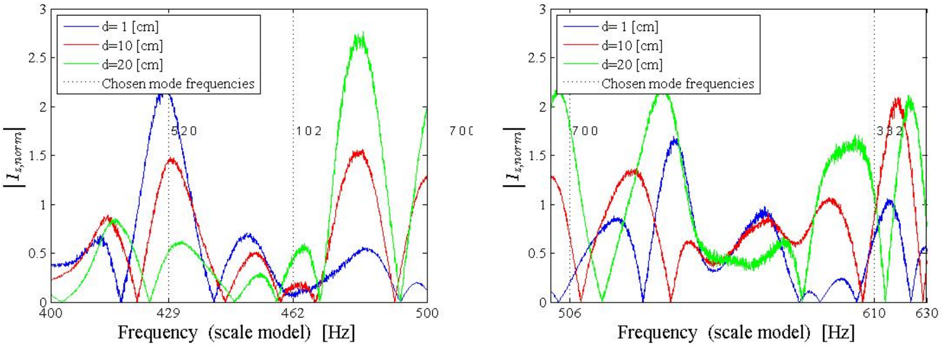

(e) $I_z(d)$, position 3 – 8th and 9th mode

(f) $I_z(d)$, position 3 – 10th and 11th mode

Figure B.9: $I_z(d)$, position 3, frequency scale zoom

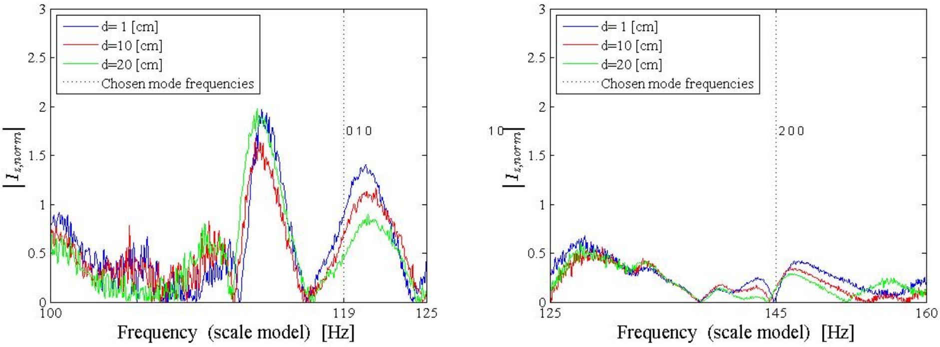

(a) $I_z(d)$, position 4 – 1st mode

(b) $I_z(d)$, position 4 – 2nd mode

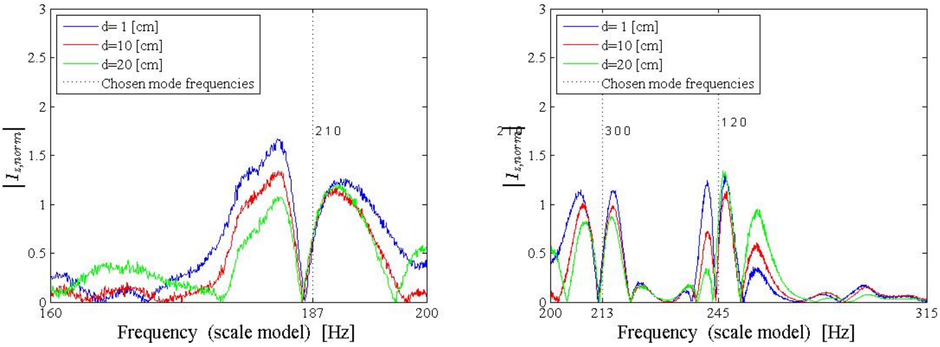

(c) $I_z(d)$, position 4 – 3rd mode

(d) $I_z(d)$, position 4 – 4th and 5th mode

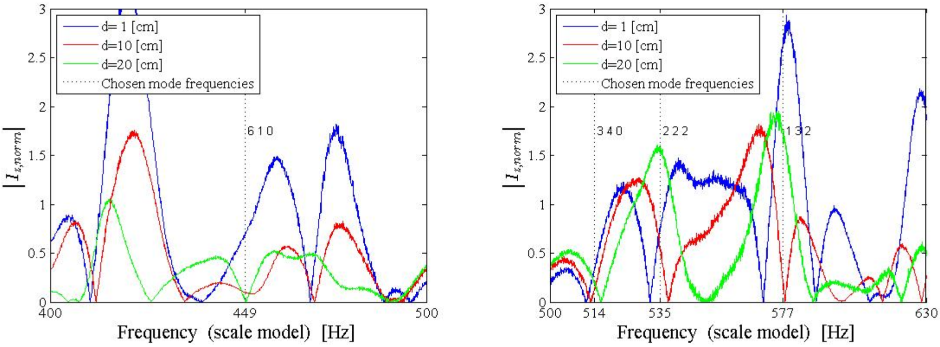

(e) $I_z(d)$, position 4 – 6th mode

(f) $I_z(d)$, position 4 – 7th, 8th and 9th mode

Figure B.10: $I_z(d)$, position 4, frequency scale zoom

Appendix C

Discussion

Appendix C contains some complimentary figures to to the ones presented in Chapter 5. Figures C.1 show the transfer functions from measurement series 1 with the theoretical mode frequencies relevant to the measurement position drawn as vertical lines. Note that the figure showing measurement position 1 has already been presented in Chapter 5, so only the figures showing measurement positions 2,3 and 4 are included here.

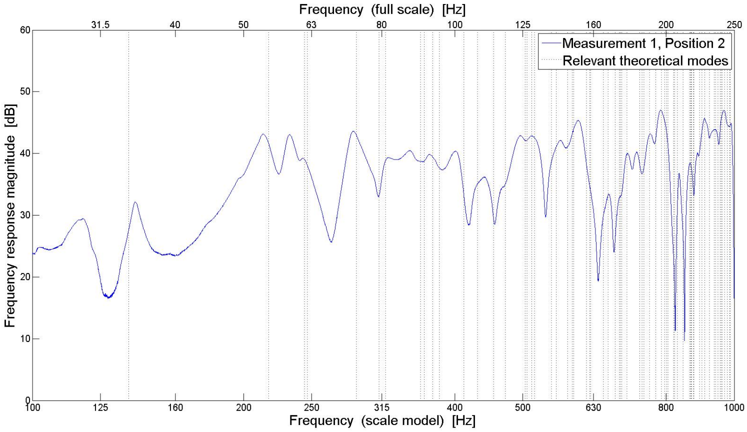

(a) $H_{p,1}$, position 1

Figure C.1: Transfer functions $H_{p,1}$ (from measurement series 1) with theoretical modes

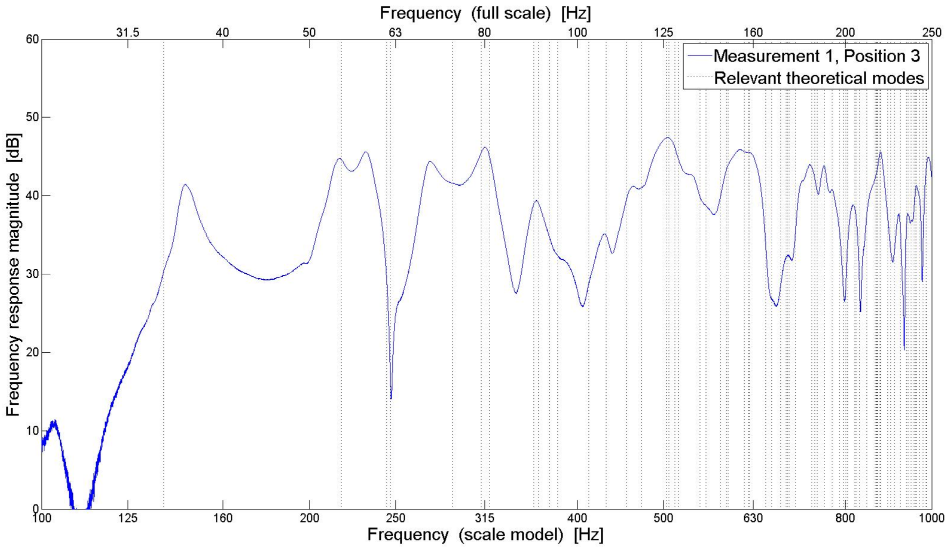

(b) $H_{p,1}$, position 3

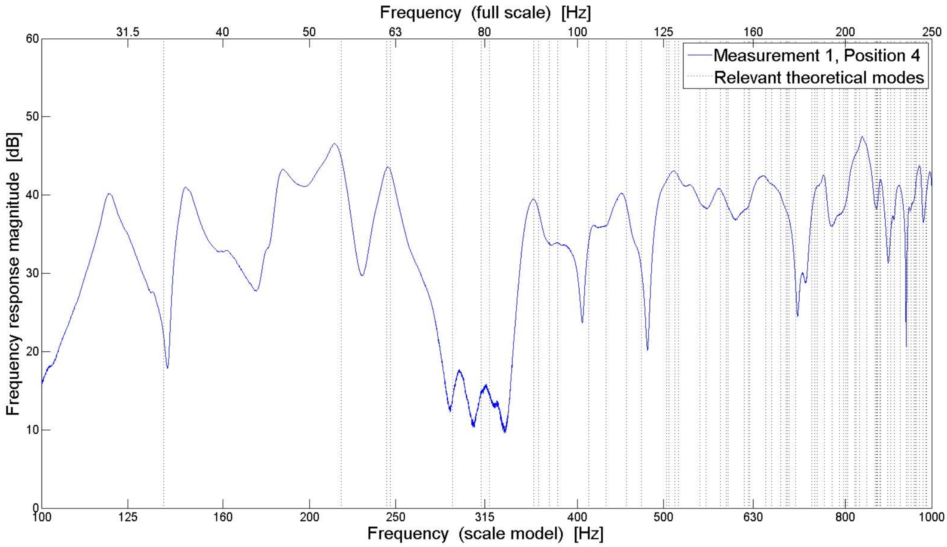

(c) $H_{p,1}$, position 4

Figure C.1: Transfer functions $H_{p,1}$ (from measurement series 1) with theoretical modes